Relativistic self-consistent models for atomic nuclei derived from the empirical densities

Accorto, Giacomo

Doctoral thesis / Disertacija

2022

University of Zagreb

Faculty of Science and Mathematics

Department of Physics

Giacomo Accorto

RELATIVISTIC SELF-CONSISTENT

MODELS FOR ATOMIC NUCLEI DERIVED

FROM THE EMPIRICAL DENSITIES

DOCTORAL DISSERTATION

Zagreb, 2022

University of Zagreb

Faculty of Science and Mathematics

Department of Physics

Giacomo Accorto

RELATIVISTIC SELF-CONSISTENT

MODELS FOR ATOMIC NUCLEI DERIVED

FROM THE EMPIRICAL DENSITIES

DOCTORAL DISSERTATION

Supervisor: Tamara Nikšić

Zagreb, 2022

Sveučilište u Zagrebu

Prirodoslovno-matematički fakultet

Fizički odsjek

Giacomo Accorto

RELATIVISTIČKI SAMOSUGLASNI

MODELI ATOMSKIH JEZGARA IZVEDENI

IZ EMPIRIJSKIH GUSTOĆA

DOKTORSKI RAD

Mentor: Tamara Nikšić

Zagreb, 2022.

Information on the supervisor

Supervisor:	Prof. Tamara Nikšić
Position:	Full Professor
Fields of interest:	*Theoretical nuclear physics:* nuclear energy density functionals, collective models of nuclear structure, clustering in light nuclei. *Computational nuclear physics*
Awards:	Annual Croatian State Award for Science in 2012
Tel:	+385 1 4605574
Location:	Department of Physics, Faculty of Science, University of Zagreb
Website:	http://www.phy.pmf.unizg.hr/~tniksic/

Tamara Nikšić is an associate professor at the Department of Physics, Faculty of Science, University of Zagreb, where she has been employed from 2000. She received her PhD degree from the University of Zagreb in 2004 (*Relativistic description of nuclear structure: models with density-dependent meson-nucleon couplings*, supervisor: prof. Dario Vretenar). She was an Alexander von Humboldt fellow at the Technical University Munich (2005-2006) in the group of professor Peter Ring. Her research interests span both theoretical nuclear physics and computational physics. Most of her work has been on developing the new generation of nuclear energy density functionals and describing the correlations originating from restoration of broken symmetries and fluctuation of the quadrupole and octupole deformations. Recently, she has been involved in describing possible mechanisms of cluster formation in light nuclei. In 2012 she received the Annual Croatian State Award for Science. She teaches at the Department of Physics, Faculty of Science, University of Zagreb.

Five selected publications:

1. Z.X. Ren, J. Zhao, D. Vretenar, T. Nikšić , P.W. Zhao, J. Meng, Microscopic analysis of induced nuclear fission dynamics, Phys. Rev. C 105, 044313 (2022).

2. G. Accorto, T. Naito, H. Liang, T. Nikšić , D. Vretenar, Nuclear energy density functionals from empirical ground-state densities, Phys. Rev. C 103, 044304 (2021).

3. J. Zhao, T. Nikšić , D. Vretenar, S.G. Zhou, Microscopic self-consistent description of induced fission dynamics: Finite-temperature effects, Phys. Rev. C 99, 014618 (2019).

4. T. Nikšić , M. Imbrišak, D. Vretenar, "Sloppy" nuclear energy density functionals II. Finite nuclei, Phys. Rev. C 95, 054304a (2017).

5. T. Nikšić , D. Vretenar, "Sloppy" nuclear energy density functionals: Effective model reduction, Phys. Rev. C 94, 024333 (2016).

Acknowledgments

Relativistic self-consistent models for atomic nuclei derived from the empirical densities

Giacomo Accorto

Abstract

The solution of the inverse problem of Density Functional Theory (DFT), also known as the inverse Kohn-Sham (IKS) problem, is exploited to derive the functional form of the KS potential starting from empirical neutron and proton densities. Two independent numerical routines to calculate the KS potential are studied, encoded, and tested. The formalism for the density-to-potential inversion is developed both in the non-relativistic and relativistic framework. Within the relativistic formalism, starting from a relatively simple functional form, the piece of information encoded in the KS potentials is employed in the framework of Density Functional Perturbation Theory (DFPT). A model is developed to improve a functional towards the exact, unknown, relativistic nuclear energy density functional (NEDF).

Nuclear DFT, expressed through the formalism of NEDFs and self-consistent mean-fields, is identified as the best tool to tackle the microscopic description of the nuclear fission process. A numerical routine is developed to find continuous minimum energy paths (MEP) to eliminate discontinuities on the potential energy surfaces. The capability of the numerical routine to produce smooth fission paths that are related to the correct properties is tested. To these purpose, spontaneous fission lifetimes calculated along smoothed MEPs are compared to the results obtained on the original discontinuous paths and to reference state-of-the-art values.

147 pages, 23 figures, 3 tables, 152 references.

Original language: English.

Thesis deposited in the library of Physics Department, Faculty of Science, University of Zagreb, Bijenička 32.

Sveučilište u Zagrebu

Prirodoslovno-matematički fakultet   Doktorski Rad

Fizički odsjek

Relativistički samosuglasni modeli atomskih jezgara izvedeni iz empirijskih gustoća

Giacomo Accorto

Prošireni sažetak

Iako trenutno ne postoji teorijski okvir koji bi mogao opisati cjelokupnu fenomenologiju nuklearne fizike, dostupni su razni modeli za proučavanje pojedinih aspekata nuklearne strukture. Modeli temeljeni na nuklearnim energijskim funkcionalima gustoće (NEDF) trenutno predstavljaju najpotpuniji opis svojstava osnovnog stanja i kolektivnih pobuđenja atomske jezgre. Niti jedna druga metoda ne može postići usporedivu globalnu preciznost uz jednake računalne resurse te tako omogućujem opis strukture atomskih jezgara preko cijele karte nuklida, počevši od vrlo lakih sustava pa sve do super-teških elemenata, od doline beta-stabilnosti do linije curenja nukleona.

Teorijski okvir nuklearnih energijskih funkcionala gustoće primijenjeni su u razvoju brojnih mikroskopsih modela, primjerice relativističke aproksimacije slučajnih faza, modela međudjelujućih bozona ili metode generatorskih koordinata koja omogućuje istraživanje niskoenergijske spektroskopije i dinamike velikih amplituda.

Temeljna implementacija ovog teorijskog okvira odgovara samosuglasnom modelu srednjeg polja, uz korištenje efektivnog međudjelovanja i određene razine aproksimacije. Takav model uključuje nuklearni energijski funkcional jednočestične matrice gustoće koja odgovara Slaterovoj determinanti.

Samosuglasni modeli srednjeg polja temelje se na konceptu neovisnih čestica koje se nalaze u srednjem polju. Iako jednostavna, slika neovisnih čestica je dosada potvrđena mnogim eksperimentalnim opažanjima. Nukleoni u ovoj slici tvore jezgru kao samo-vezani sustav, a srednje polje nastaje usrednjavanjem dvočestičnih međudjelovanja. Nadalje, srednje polje je statičko, dok su dinamičke korekcije zanemarene.

Ujedinjeni opis srednjeg polja atomske jezgre i korelacija sparivnaja može se postići u okviru nerelativističkog Hartree-Fock-Bogoliubov pristupa ili relativističkog Hartree-Bogoliubov pristupa. Da bi se očuvala slika neovisnih čestica, Bogoliubov transformacijom se prelazi s čestica na kvazičestice. Ovaj pristup se pokazao uspješnim čak i u opisu vrlo egzotičnih jezgara daleko od doline stabilnosti.

U atomskoj fizici je moguće izvesti energijske funkcionale gustoće visoke preciznosti pomoću modela elektronskog plina. Nasuprot tome, u nuklearnoj fizici detalji nuklearne sile nisu dobro poznati, pa se točan oblik efektivnog međudjelovanja može samo približno odrediti pomoću mikroskopskih računa temeljenih na fundamentalnom nukleon-nukleon međudjelovanju. Postoje i dodatne razlike u odnosu na atomsku fiziku, primjerice nuklearno međudjelovanje bitno ovisi o spinu, izospinu i impulsu, a nemoguće je zanemariti i spin-orbit međudjelovanje, tenzorske članove i tročestična međudjelovanja.

Posve fenomenološki nuklearni energijski funkcionali gustoće (Skyrme, Gogny, relativistički funkcionali) uključuju relativno mali broj parametara, ali usprkos tome omogućuju zadovoljavajuću preciznost kroz cijelu kartu nuklida. Dio parametara se može izvesti koristeći poznata svojstva simetrične i asimetrične nuklearne materije u blizini saturacije, dok se ostale parametre prilagođava eksperimentalnim podacima, primjerice masama i radijusima atomskih jezgara.

Među dostupnim računalnim alatima za rješavanje Dirac-Hartree-Bogoliubov jednadžbi, treba istaknuti DIRHB programski paket koji omogućuje rješavanje problema u sfernoj, cilindričnoj i triaksijalnoj geometriji. Paket uključuje najnovije energijske funkcionale gustoće i omogućava precizne proračune kroz cijelu kartu nuklida, a trenutna verzija je ograničena na parno-parne atomske jezgre. Dirac-Hartree-Bogoliubov jednadžbe se rješavaju samosuglasnim iterativnim postupkom koji uključuje izračune gustoća i polja u koordinatnom prostoru i dijagonalizaciju matrične Dirac-Hartree-Bogoliubov jednadžbe u konfiguracijskom prostoru svojstvenih stanja harmoničkog oscilatora. Dijagonalizacija daje kvazičestične energije i valne funkcije koje se koriste u izračunu matrice gustoće i tenzora sparivanja u konfiguracijskom prostoru. U sljedećem koraku se računaju gustoće i polja u koordinatnom prostoru te se zatim pomoću njih gradi Dirac-Hartree-Bogoliubov Hamiltonijan koji se dijagonalizira u sljedećoj iteraciji. Postupak se nastavlja dok razlika u poljima između dva iterativna koraka nije manja od neke unaprijed zadane male vrijednosti. U tom slučaju se kaže da je postupak konvergirao.

Osim traženja osnovnog stanja atomske jezgre, moguće je odrediti rješenje u kojem je fik-

sirana očekivana vrijednost nekog zadanog operatora što se postiže metodom Lagrangeovih multiplikatora. Vrlo uspješna implementacija ovog postupka je tzv. *Multi-Linear Constraint* metoda opisana u appendixu B.

Teorija funkcionala gustoće (*Density Functional Theory* - DFT) predstavlja jedan od najuspješnijih teorijskih pristupa opisu mnogih višečestičnih sustava, npr elektronskih ili atomskoj jezgri. U suštini, DFT govori da postoji jednoznačno mapiranje između egzaktne gustoće osnovnog stanja sustava i gustoće koja minimizira univerzalni i egzaktni funkcional gustoće. Originalna formulacija DFT-a, uspostavljena od strane Hohenberga i Kohna 1964. godine, temelji se ne teoremima egzistencije egzaktnog energijskog funkcionala gustoće, ali ne pruža nikakve smjernice kako konstruirati takav egzaktni funkcional.

Većina primjena DFT-a se stoga okreće Kohn-Sham (KS) shemi. Uvodi se pomoćni sustav neovisnih čestica koji je jednoznačno definiran kada je gustoća jednaka onoj originalnog sustava. Jednom kada je ova jednakost uspostavljena, minimum energijskog funkcionala gustoće pomoćnog sustava podudara se s minimum originalnog sustava. Time se pruža mogućnost opisa svih svojstava osnovnog stanja originalnog sutava. Unutar KS formulacije DFT-a moguće je razložiti energijski funkcional gustoće na član kinetičke energije, Hartree član i nepoznati doprinos efektivnog potencijala izmjena i korelacija (*exchange-correlation*).

U proteklih nekoliko desetljeća napravljeni su brojni pokušaji poboljšanja preciznosti nuklearnih energijskih funkcionala gustoće, no zasada prediktivna moć teorijskih modela ostaje daleko ispod preciznosti suvremenih mjerenja. Trenutni napori u izgradnji općenitijih funkcionala su otežani nedostatkom strategije za sustavna poboljšanja. U tom smislu bi se trebalo istražiti metode i strategije koje su se već pokazale kao obećavajuće izvan uskih okvira nuklearne fizike.

Jedan od takvih alternativnih pristupa je inverzni DFT problem koji se već pokazao uspješnim u opisu elektronskih sustava. Inverzni DFT problem se sastoji u određivanju Kohn-Sham potencijala iz poznate gustoće osnovnog stanja sustava. Time bi se empirijski određene gustoće atomske jezgre mogle upotrijebiti za sustavna poboljšanja egzaktnog, ali nepoznatog, nuklearnog energijskog funkcionala gustoće.

U ovom radu je razmotrena implementacija dva algoritma za rješavanje nerelativističkog inverznog KS problema temeljena na različitim formulacijama DTF-a. Oba algoritma su se dosada pokazala uspješnima u drugim granama fizike te su stoga prilagođena opisu atomske jezgre.

Metoda ograničenih varijacija (*Constrained Variation Method*) temelji se na minimizaciji

kinetičke energije umjetnog KS sustava, čije orbitale su ograničene na način da i) reproduciraju zadanu gustoću sustava, ii) budu ortogonalne. Koristeći metodu Lagrangeovih multiplikatora, postupak ograničene minimizacije pretvara se u optimizaciju Lagrangiana bez ograničenja. Minimizacija funkcionala odstupanja daje skup minimalnih KS orbitala. Funkcionalna forma KS potencijala, po definiciji jednaka Lagrangeovim multiplikatorima povezanim s ograničenjem gustoće, se tada određuje rješavanjem pridruženog skupa Euler-Lagrange jednadžbi. Formalizam ove metode je vrlo općenit i moguće primjene bi trebale biti neovisne o geometriji sustava. S druge strane, praktična implementacija ovog formalizma nije intuitivna niti jednostavna.

Druga razmotrena metoda (van Leeuwen Baerends) sastoji se od invertiranja i iterativnog rješavanja KS jednadžbi. U svakom koraku se ansatz za KS potencijal postupno prilagođava da bi se gustoća KS sustava približila ciljanoj gustoći egzaktnog sustava. Iako bi poopćenje ove metode na razne geometrije ili sustave s otvorenim ljuskama moglo biti nešto složenije, temeljna ideja je vrlo intuitivna, a implementacija za sferne sustave sa zatvorenim ljuskama nije složena. Ipak, da bi se postigla konvergencija metode, potrebno je koristiti napredne numeričke tehnike, npr. Borydenov postupak miješanja iterativnih rješenja.

Oba algoritma su implementirana i provjerena na nekoliko primjera teorijskih i empirijskih gustoća atomskih jezgara sa zatvorenim ljuskama. Kohn-Sham potencijali, izvedeni iz empirijskih protonskih gustoća jezgara ^{40}Ca i ^{208}Pb, kao i neutronske gustoće jezgre ^{208}Pb, imaju razumne vrijednosti kako u unutrašnjosti jezgre, tako i na njezinoj površini. Nasuprot tome, parametrizacije empirijskih gustoća koje koriste sumu Gaussiana, vode na nefizikalne vrijednosti Kohn-Sham potencijala za veće vrijednosti radijusa: u svim slučajevima je potvrđeno divergentnoponašanje vezano uz asimptotsko ponašanje oscilatorskih valnih funkcija. Takvo nefizikalno ponašanje Kohn-Sham potencijala počinje u području izvan radijusa vanjskog Gaussiana iskorištenog u parametrizaciji. Iz toga se može zaključiti da izvedeni Kohn-Sham potencijal postaje nepouzdan u područjima gdje se empirijske gustoće ekstrapoliraju. Da bi se dodatno provjerila ova interpretacija, inverzni Kohn-Sham algoritmi su provjereni tako da se umjesto empirijskih gustoća kosite teorijske vrijednosti dobijene s Hartree-Fock računom pomoću SkX Skyrme parametrizacije. U ovom slučaju je asimptotsko ponašanje gustoća korektno te Kohn-Sham potencijali postaju imaju fizikalne vrijednosti za sve radijalne udaljenosti.

Suvremeni nuklearni energijski funkcionali gustoće ovise o spinskim gustoćama, kao i o gradijentima gustoća koje se ne mogu odrediti eksperimentalno. Nadalje, eksperimentalni po-

daci o neutronskim gustoćama su rijetki. Iako bi pokušaji proširivanja algoritama inverznog Kohn-Shama na veći skup jezgara, uključujući deformirane jezgre, zasigurno bili zanimljivi, razvidno je da su empirijske gustoće raspodjela neutrona i protona nedovoljne za izračun efektivnog Kohn-Sham potencijala. Stoga je raspon primjena inverznog Kohn-Sham problema zasad ograničen.

Iterativna van Leeuwen Baerends metoda je prilagođena relativističkim nuklearnim energijskim funkcionalima gustoće. Jedan od glavnih argumenata za upotrebu relativističkih funkcionala je prirodno pojavljivanje spin-orbit potencijala kao kombinacije skalarnog i vektorskog potencijala. Spin-orbit međudjelovanje je relativistički efekt koji uzrokuje cijepanje i pomake energijskih nivoa atomske jezgre. Spin-orbit član u atomskoj jezgri je bitno veći od spin-orbit člana u atomu, te određuje strukturu ljusaka u atomskoj jezgri i posebno magične brojeve. U nerelativističkim funkcionalima se spin-orbit član dodaje fenomenološki i ne može biti određen iz gustoća osnovnog stanja pomoću inverzne Kohn-Sham metode.

Relativističko poopćenje vLB algoritma je provjereno na nekoliko teorijskih skalarnih i vektorskih gustoća. Pokazana je visoka razina pouzdanosti u određivanju povezanih skalarnih i vektorskih potencijala. Nedostatak ovog poopćenja je činjenica da skalarna gustoće nije eksperimentalna opservabla. Točni i sustavni podaci postoje samo za gustoću raspodjele naboja u jezgri, dok konstrukcija Kohn-Sham potencijala podrazumijeva korištenje skalarnih gustoća i vektorske izovektorske gustoće. Mogućnost nastavka istraživanja u ovom smjeru bilo bi korištenje jednadžbe stanja nuklearne materije za određivanje izoskalarnog-skalarnog i izovektorskog kanala Kohn-Sham potencijala.

Drugi problem primjene inverzne Kohn-Sham metode predstavlja ne sasvim jasna poveznica Kohn-Sham potencijala i nuklearnog energijskog funkcionala gustoće. čak i ako bismo pronašli jednoznačnu poveznicu, nuklearni energijski funkcional gustoće bi sadržavao informacije o nekoliko specifičnih atomskih jezgara što je u suprotnosti s konceptom univerzalnog energijskog funkcionala gustoće. Moguće rješenje je korištenje *ab initio* računa za provjeru inverzne Kohn-Sham metode na sustavima koji imaju slična svojstva. Primjerice, neutronske kapljice bi predstavljale idealan sustav za takav pokušaj. Nuklearni energijski funkcional gustoće bi se tada mogao izvesti koristeći metode funkcionalne integracije.

U ovom radu smo se odlučili za upotrebu kombinacije računa smetnje i teorije funkcionala gustoće budući da se ovakav pristup pokazao uspješnim u atomskoj fizici. Pomoću računa smetnje se može sustavno korigirati zadani nuklearni energijski funkcional gustoće kako bismo se

približili nepoznatom egzaktnom funkcionalu. Stoga smo predložili model koji koristi empirijske gustoće za izvod Kohn-Sham potencijala u nekoliko odabranih atomskih jezgara. Konkretnije, egzaktna vektorska i skalarna gustoća za mali broj jezgara sa zatvorenim ljuskama, zajedno s energijskim nivoima izvedenih Kohn-Sham potencijala, predstavlja nužne ulazne podatke za procjenu prvog reda korekcije početnog funkcionala prema egzaktnom funkcionalu. Pritom se pretpostavlja da je razlika između početnog i egzaktnog funkcionala dovoljno mala da bi se mogao koristiti prvi red računa smetnje.

Predloženi model je provjeren na nekoliko ilustrativnih primjera pri čemu je kao egzaktni ciljani funkcional pretpostavljen relativistički DD-PC1 funkcional. Račun je pokazao da se model može upotrijebiti za popravak aproksimativnog funkcionala prema potpunom DD-PC1 funkcionalu. Prvi test je pokazao da se kao početni funkcional može pretpostaviti dio DD-PC1 funkcionala s konstantnim vezanjima, a model će kao korekciju vratiti potpuni funkcional. Drugi test je kao početni funkcional pretpostavio *Ansatz* u kojem se funkcional parametrizira kvadratičnim polinomom gustoća. Model je i u ovom slučaju kao korigirani funkcional vratio egzaktni DD-PC1 funkcional.

Drugi dio radnje se odnosi na praktične primjene samosuglasnih modela atomske jezgre. Konkretnije, takvi modeli su primijenjeni u opisu procesa nuklearne fisije. Radi se o jednom od najsloženijih procesa u nuklearnoj fizici u kojem se teška atomska jezgra cijepa u dva ili više lakših fragmenata. Fisija može biti spontana ili inducirana.

Spontana fisija sastoji se od cijepanja jezgra u fragmente i promptnoj emisiji neutrona. Prouzročena je natjecanjem između Coulombovog odbijanja među protonima u jezgri i jake nuklearne sile koja veže nukleone u jezgru. Stoga do spontane fisije dolazi u teškim jezgrama s velikim brojem protona, uglavnom u području aktinida i transaktinida. Spontana fisija je glavni proces koji ograničava mogućnosti formiranja super-teških elemenata bogatih protonima. Fisija također može biti inducirana nuklearnom reakcijom između jezgre mete i laganom projektila (neutron, proton, alpha-čestica, gamma-zračenje). Inducirana fisija ima ključnu ulogu u nukleosintezi, posebno u okviru r-procesa gdje ciklusi fisije kontroliraju udjela jezgara bogatih neutrona.

Tijekom procesa fisije oslobađa se velika količina energije, raspoređena na kinetičku energiju fragmenata i energiju pobuđenja fragmenata. Proces fisije je često praćen emisijom neutrona i gamma zračenja. Zbog velike količine oslobođene energije, proces fisije je jedan od najvažnijih izvora električne energije.

Temeljito poznavanje procesa fisije je ključno za dobivanje pouzdanih predikcije, posebno u području karte nuklida gdje eksperimentalni podaci nisu dostupni ili su rijetki. Stoga pouzdani mikroskopski opis procesa fisije predstavlja jedan od najizazovnijih problema suvremene nuklearne fizike. Problem je iznimno složen zbog velikog broja parametara i fizikalnih veličina koje igraju važnu ulogu u procesu fisije, pri čemu su neki vezani na kolektivne stupnjeve slobode atomske jezgre, a neki na stupnjeve slobode pojedinih nukleona koji čine jezgru. Stoga je vrlo složeno uvoditi sustavne aproksimacije koje bi omogućile opis procesa fisije uz prihvatljivu i prediktivnu razinu grešaka.

Modeli temeljeni na nuklearnim energijskim funkcionalima gustoće su identificirani kao najbolji izbor za mikroskopski opis procesa fisije. Većina primjena se oslanja na adijabatsku aproksimaciju, pri čemu se pretpostavlja da je vremenska skala kolektivnih stupnjeva slobode atomske jezgre nekoliko redova veličine veća od vremenske skale intrinzičnih stupnjeva slobode pojedinih nukleona. Stoga se može reći da su kolektivni i intrinzični stupnjevi slobode savršeno razvezani što omogućuje mapiranje nuklearnog problema mnoštva čestica na kolektivnu Schrödingerovu jednadžbu koja uključuje mali skup kolektivnih varijabli. U adijabatskom modelu nije moguće jednoznačno odrediti točku pucanja atomske jezgre te se stoga koriste empirijske definicije, najčešće povezane s brojem nukleona u području između formiranih fisionih fragmenata.

Jedan od problema koji se pojavljuju u realističnim simulacijama procesa fisije, temeljenim na rješavanju kolektivne Schrödingerove jednadžbe, je pojava nefizikalnih diskontinuiteta na energijskim plohama. Ograničena dostupnost računalnih resursa općenito onemogućava korištenje više od nekoliko kolektivnih koordinata, dok se preostale koordinate koje nisu ograničene prilagođavaju u samosuglasnom postupku traženja globalnog minimuma energije. Stoga nema nikakve garancije da će dobijena energijska ploha biti glatka. Prisutnost diskontinuiteta može prouzročiti ozbiljne probleme u simulacijama procesa fisije, primjerice može prikriti pravu visinu fisionih barijera.

U ovom radu smo pokušali definirati pouzdanu proceduru provjere prisutnosti diskontinuiteta na energijskoj plohi, kao i proceduru eliminacije diskontinuiteta pronalaženjem glatke putanje koja minimizira energiju jezgre.

Provjera prisutnosti diskontinuiteta može se provesti izračunom preklopa između susjednih stanja na energijskoj plohi. S tim ciljem smo implementirali formalizam proračuna preklopa koji rješava mnoga ograničenja tradicionalnih pristupa temeljenih na Onishi formuli i korištenju

Pfaffiana i omogućuje račune sa stanjima koja su dobijena u proizvoljnim bazama harmoničkog oscilatora. Ovaj korak je bio ključan jer simulacije procesa fisije uključuju konfiguracije s ekstremnim vrijednostima deformacija pa je za konvergenciju računa nužno koristiti optimiziranu bazu harmoničkog oscilatora s pažljivo odabranom deformacijom oscilatora i uključivanjem samo onih stanja oscilatora koja su nužna za opis dane konfiguracije. Stoga se u računu preklopa pojavljuju baze koje ne moraju nužno imati istu dimenziju, niti istu deformaciju oscilatora. Uvedeni formalizam omogućuje precizan izračun preklopa s takvim različitim bazama što dosada nije bilo moguće.

Nadalje, razvijena je i testirana rutina temeljena na metodi dinamičkog programiranja (DPM). Takva rutina se može koristiti za pronalaženje putanje minimalne energije preko malih dvodimenzionalnih energijskih ploha s ciljem uklanjanja diskontinuiteta koji postoje na jednodimenzionalnim energijskim plohama. DPM s optimiziranim *breadth-first tree serach* (BFS) algoritmom je implementiran na diskretiziranoj energijskoj plohi s ciljem nalaženja glatke krivulje minimalne energije. Optimizacije BFS algortima podrazumjeva proračun samo ograničenog broja putanja u svakom koraku pretrage što bitno smanjuje zahtjeve na računalnu memoriju i računalno vrijeme. Budući da ovi zahtjevi rastu eksponencijalno s veličinom prostora pretrage, optimizacija je nužna za praktične primjene.

Glavna ideja izglađivanja energijskih ploha je korištenje stablaste strukture dvodimenzionalnih energijskih ploha. Počevši od inicijalnog čvora, odabranog među točkama ulazne energijske plohe s diskontinuitetom, BFS algoritam istražuje sve čvorove energijske plohe i na kraju pretrage odabire putanju s najmanjom vrijednosti integrirane energije. Nasuprot tome, DPM uspoređuje sve putanje koje završavaju u istom čvoru i odbacuje sve osim putanje s najmanjom vrijednosti integrirane energije. Stoga DPM uspoređuje bitno manji broj putanja čime se smanjuju zahtjevi na računalne resurse.

Tijekom pretrage se mogu postaviti i dodatni zahtjevi na normu preklopa između susjednih stanja na energijskoj plohi, kao i na prihvatljivu vrijednost gradijenta energije. Iako ovi zahtjevi u načelu mogu pridonijeti izglađivanju plohe, oni istovremeno relaksiraju adijabatsku hipotezu. Tako dobijena putanja neće nužno prolaziti kroz lokalne minimume zadane energijske plohe, iako će integrirana energija biti minimalne. Nadalje, ovi zahtjevi ograničavaju prostor pretraživanja algoritma što u nekim slučajevima može onemogućiti pronalaženje rješenja.

Konačno, provjerena je pouzdanost izglađenih energijskih ploha dobijenih DPM-om. Test je napravljen izračunom fisionih vremena života. Spontana fisija je primjer procesa kvantnog

tuneliranja čestice kroz energijsku barijeru. Tijekom fisije složene jezgre sustav mora savladati dvije ili tri energijske barijere prije nego stigne do sedlene točke kada postaje nestabilna. Vjerojatnost događanja fisije je u kompeticiji s drugim modovima raspada, odnosno vrijeme potrebno za fisiju je vezano uz penetrabilnost jezgre kroz energijsku barijeru koja razdvaja osnovno stanje od konfiguracija s ekstremnim deformacijama. Preciznije, u poluklasičnoj WKB aproksimaciji, vrijeme života je proporcionalno eksponencijalnoj funkciji akcije izračunatoj na fisionoj putanji. Iako se najpouzdaniji pristupi proračunu vremena života temelji na putanji koja minimizira akciju, u literaturi je pokazano da putanje koje minimiziraju energiju također daju prihvatljive rezultate te smo stoga koristili putanju minimalne energije.

Svi dobiveni rezultati su ispravnog reda veličine u odnosu na empirijske podatke pri čemu treba naglasiti da vremena života poprimaju vrijednosti u vrlo širokom rasponu od približno 30 redova veličine. Relaksacija adijabatskog uvjeta koja se koristi u okviru DPM metode za izglađivanje plohe jer također provjerena i ne utječe negativno na izračunata vremena života. Također je utvrđeno da izglađivanje energijskih ploha sustavno poboljšava izračunate vrijednosti vremena života u usporedbi s vrijednostima dobivenim na plohama koje pokazuju diskontinuitete.

Predložene metode predstavljaju pouzdanu i ekonomičnu alternativu tradicionalnim pristupima rješavanju problema diskontinuiteta na energijskim plohama koje podrazumijevaju povećanje dimenzije kolektivnog prostora. Sljedeći korak je generalizacija predloženih metoda kako bi se mogle izglađivati dvodimenzionalne plohe s diskontinuitetima. Preliminarni proračuni pokazuju da je takva generalizacije izvedljiva i predstavljala bi važan korak u daljnjim istraživanjima statičkih i dinamičkih svojstava procesa fisije.

Keywords

Contents

INTRODUCTION

A theoretical framework able to describe nuclear phenomenology in its entirety does not exist. Nonetheless, many models are available on the market for the study of different aspects of nuclear structure. Among them, nuclear energy density functionals (NEDFs) currently provide the most complete description of ground-state properties and collective excitations. No other method achieves comparable global accuracy at the same computational cost, allowing for the description of nuclear structure phenomena throughout the entire chart of nuclides, from light systems to super heavy elements, from the valley of β-stability to the particle drip-lines. The framework of NEDFs has been employed to develop several microscopic models, *e.g.*, the random phase approximation, the interacting boson model, and the generator coordinate method, that allow to explore low-energy spectroscopy and large-amplitude dynamics.

The basic implementation of the framework corresponds to the self-consistent mean-field (SCMF) model, specifically realized by means of an adopted effective interaction solved at a certain level of approximation. It includes a NEDF built as a functional of one-body nucleon density matrices corresponding to a single product state. SCMF models are based upon an important concept supported by many phenomenological evidences: the independent particle picture. Kept as a guidance for all attempts of systematic improvement, it considers nucleons to be self-bound by the average of two-body interactions over the states occupied by the other particles. The mean-field, created in a self-consistent way, is considered to be static, so that dynamical corrections are, at least to some extent, neglected. A unified description of the nuclear mean-field and of the strong pairing correlations can be achieved within the Hartree-Fock-Bogoliubov (HFB) or the relativistic Hartree-Bogoliubov (RHB) approximations. In order to preserve the independent particle picture, the focus of study is shifted from nucleons to quasi-particles defined by the Bogoliubov transformation. The theory can then be successfully applied even to the physics of exotic nuclei far from stability.

In atomic physics, energy density functionals of remarkable accuracy can be derived from

the electron gas theory. In contrast, in nuclear physics, where the details of the nuclear force are not well known, the specific form of the effective interaction might be at most motivated from some microscopic calculation based on the underlying nucleon-nucleon interaction. Unlike the atomic case, the nuclear interaction is strongly spin-, isospin- and momentum-dependent. Spin-orbit and tensor terms, as well as three-body components, cannot be neglected. Fully phenomenological NEDFs, such as Skyrme, Gogny, and relativistic ones, adopt a small number of model parameters to reach satisfactory accuracy across the whole nuclear chart. Some of the parameters of the functional can be derived, at least qualitatively, exploiting bulk properties of symmetric and asymmetric infinite nuclear matter at saturation. The rest are usually fitted to ground-state experimental data of finite nuclei, such as masses and charge radii.

Density Functional Theory (DFT) represents one of the most successful theoretical approaches to the study of both electronic and nuclear structure. The usage itself of a NEDF for the description of nuclear systems finds a robust justification only when encapsulated within this exact theory. Expressly, DFT states a one-to-one mapping between the correct ground-state density of a fermion system and the minimum of a universal and exact energy density functional. The original formulation of DFT is based on existence theorems of this exact energy density functional but it does not point to any constructive method to get its form, which remains basically unknown. Most applications of DFT for precise calculations resort therefore on a mathematical reorganization of the energy density functional: the Kohn-Sham (KS) scheme. An auxiliary non-interacting system is uniquely defined once its density is set equal to that of the original system. Once this equality is established, the minimum of the energy density functional of the fictitious system coincides with that of the original one. One gets thereby access to all ground-state properties of the original system. Within the KS formulation of DFT one is able to write down the terms that compose the NEDF, namely a non-interacting kinetic energy term and a contribution given by an effective exchange-correlation KS potential coupled to the density.

Across the last decades, many have been the attempts to improve the accuracy of NEDFs, and yet the present predictive power of theoretical models remains far below the precision of modern experimental results. Specifically, current efforts to build more general NEDFs are hindered by the lack of a strategy for systematic improvement. In this context alternative approaches should be pursued, possibly gazing beyond the landscape of nuclear physics in search of innovatory ideas. In this sense, the inverse DFT problem has already proved to be useful in

the case of electronic systems. The problem consists in deducing the form of the Kohn-Sham potential once the density function of a nucleus is given. The information encoded into empirical nuclear densities might then be used to improve a given functional towards the exact but unknown NEDF.

The first chapter of this thesis should be intended as a collection of useful concepts concerning the nuclear many-body problem. After a quick overview about the main empirical features of the nuclear force, theoretical methods commonly used to tackle the nuclear many-body problem are discussed. A special eye is constantly kept on the SCMF model. The incorporation of pairing correlations within the SCMF model, the construction of NEDFs, and the idea of breaking symmetries in order to preserve the independent particle picture, are then discussed. DFT is presented in its original formulation, together with the main issues related to that. Finally, the well-celebrated KS scheme and the main concepts of the DFT inverse problem are treated. A particular focus is given to the argument of inverse problems and how they require a more careful treatment than direct ones.

The second chapter presents the first set of results obtained in the course of this work. First, the implementation of two algorithms for the solution of the non-relativistic inverse KS problem is discussed. The algorithms are tested using theoretical and empirical densities of spherical, closed-shell nuclei. The obtained KS potentials are analyzed. In the rest of the chapter, the main limitations associated with the solution of the inverse Kohn-Sham problem are dealt with. The relativistic generalization of the inverse DFT problem is presented. A model that manages to exploit the piece of information encoded in empirical densities and KS potentials is designed and tested in the final part of the chapter. The model can be used to improve a simple NEDF towards the unknown exact one, by developing a relativistic version of Density Functional Perturbation Theory.

The nuclear fission process is a remarkable phenomenon whose microscopic description is one of the most challenging tasks in the field. In fission, the quantal features of the many-body problem are sharply intertwined to the complex dynamic collective evolution of a nuclear compound. The framework provided by NEDFs is identified as the best for a fully microscopic study of the process. The focus of the third chapter is then spontaneous fission, that is the non-induced splitting of a parent nucleus into two fragments. The chapter begins with a brief review of the process and discusses the techniques apt to calculate one of the main quantities used to characterize it, namely the spontaneous fission lifetime. The second part of this work

deals with one of the main problems that stem out in adiabatic simulations of fission based on the SCMF model: the inevitable risk of appearance of artificial discontinuities on potential energy surfaces (PESs). The presence of discontinuities on PESs creates several issues in the calculation of fission properties, by, for instance, hiding the real height of the energy barriers. A routine, based on the Dynamic Programming Method (DPM), is discussed. It quantifies the quality of a given PES, and it stitches discontinuities eventually present on that. The final part of the chapter is devoted to the calculation of fission lifetimes along the obtained smooth minimum energy paths that lead the nuclei towards scission. The purpose of the calculation is to establish if there is any impact of the stitching procedure on nuclear properties. Moreover, one would like to quantify the level of improvement brought by the smoothing process in comparison to the original, discontinuous, potential energy surface.

Chapter 1

NUCLEAR MANY-BODY PROBLEM

Nuclei are quantum many-body systems composed by self-bound protons and neutrons. Together, these two types of fermions are called nucleons; in fact, the charge independence of the nucleon-nucleon interaction, namely the equality $V_{\text{np}} = V_{\text{pp}} = V_{\text{nn}}$, allows to see them as two isospin projections of one same entity. Nuclei are kept bound by the nuclear forces, a general set of interactions comprising nucleon-nucleon, pionic and heavy mesons interactions. A standard feature of the interactions of the many-body nuclear problem is that the forces acting between each pair of fermions involve the complicated interplay of all hadrons, at least to some extent. Depending on the scale of energy at which the phenomena of interest happen, there is a different probability of producing a variety of strongly interacting particles.

A historical challenge of theoretical nuclear physics is the comprehension of the properties of atomic nuclei in terms of the bare interactions between pairs of nucleons. Undertaking this task proves to be daunting and requires an incredible amount of computional resources. Moreover, the underlying theory of strong interactions, QCD, shows that the nucleon-nucleon interaction is not a fundamental one. Thankfully, a number of sharp observations come in aid in this regard, justifying the assumption of several useful approximations for the study of the nuclear many-body problem:

- The distance between nucleons in nuclei is large enough for the strong repulsive core of the interaction not to be felt at full by nucleons. Instead, the particles composing nuclei mostly experience the softer tail of the interaction. To this purpose, it is noteworthy to consider the energy scale for removing a nucleon from a nucleus, $S_{(\text{n,p})} \approx 10$ MeV, or the average kinetic energy of nucleons in nuclei, $T \approx 40$ MeV, in comparison to the rest mass of a single nucleon, $m_{(\text{n,p})}c^2 \approx 1$ GeV, and the one of the lightest existing hadron,

the pion, $m_\pi c^2 \approx 137$ MeV. A reasonable first approximation is therefore to account for the exchange of mesons between nucleons with the action of effective forces. In this sense the full complexity of the nuclear forces does not come into play.

- In addition to the nuclear interactions, the influence of other weaker forces cannot be neglected. Protons feel and generate electromagnetic fields. The presence of weak interactions manifests itself in important processes, such as β-decays. Although taking into consideration these minor forces is not strictly required in order to establish main bulk properties of nuclear structure, they indeed play a key role in determining the stability of bound states.

- Because of the short range of the nuclear forces, all nuclei are characterized, in their interior, by an approximately constant saturation density, with value $\varrho_{\mathrm{sat}} = 0.16$ fm^{-3}, and by a volume that grows in proportion with the mass number A. The density typically decays to zero in proximity of the nuclear surface over a distance of about 2 fm. The surface thickness of nuclei is thus rather small if compared to their radial extent, defined as the distance at which the density has become half of its interior value ϱ_{sat}. An empirical value for this quantity is given by $R = r_0 A^{1/3}$, where $r_0 = 1.2$ fm can be determined by electron elastic scattering data. The experimental data available for nuclear matter distributions almost entirely consists of proton densities [1], even if the neutron density of few isotopes of lead and tin has been obtained via proton scattering [2]. In heavy nuclei, the excess of neutrons with respect to protons gives rise to differences between the densities of the two types of nucleons.

- Another important feature of nuclei is the value of the mean free path for the collision between the constituent nucleons. Many are the evidences that this quantity is large in comparison with the size of the nucleus. A long mean free path of the nucleons in nuclei entails that the interactions result in a smooth average potential, in which the particles move independent one of each other.

A simple yet effective way to understand the main trends that characterize nuclear structure is to analyze the well-celebrated semi-empirical Weizsäcker expression [3] for the total nuclear binding energy (Figure 1.1). This quantity, defined as the difference between the observed total

nuclear energy in the ground-state and the rest masses of the separated nucleons, reads

$$\mathcal{B} = b_{\text{vol}}A - b_{\text{sur}}^{2/3} - b_{\text{sym}}\frac{(N-Z)^2}{2A} - \frac{3(Ze)^2}{5R_c} \ . \tag{1.1}$$

The first term is the main, volume energy term. It represents the limit of the binding energy for heavy symmetric ($N = Z$) nuclei, in the absence of Coulomb forces. The bulk binding energy of a nucleus is proportional to A, and not to $\frac{A(A-1)}{2}$, due to the short range of the interaction. Each nucleon interacts with its neighbors, only. The second term is the surface energy. This is a contribution typical of finite systems, reflecting the fact that particles are less bound at the surface, where they have less neighbors. The third term takes into account the fact that symmetric configurations of nuclei are energetically preferred. The Pauli principle enforces protons and neutrons to occupy energy levels with increasing energy. An unbalance of any type of fermion over the other implies higher energy levels to be occupied. The last term represents the Coulomb energy of a uniform sphere with radius R_C. It is responsible for the gradual decrease of the binding energy per particle that can be observed in heavy nuclei. Also, it causes an excess of neutrons in heavy stable nuclear systems.

The Weizsäcker formula, purely qualitative and not taking into account important pairing correlations or quantum phenomena, is a noteworthy example of how many different effects, some weighting more than others, do interplay in nuclear systems. From the observed binding energies, one can deduce the order of magnitude of the average potential energy that a single nucleon feels in a nucleus. The energy required to remove a neutron from a nucleus, namely the neutron separation energy, is $\mathcal{B}(N, Z) - \mathcal{B}(N - 1, Z) \approx -(V_n + \epsilon_F) \approx 10$ MeV. Since $\epsilon_F \approx 40$ MeV, the average potential felt by a single nucleon has a depth of $|V_n| \approx 50$ MeV.

1.1 Theoretical Models For The Study Of Nuclear Structure

As well as the Nuclear Shell Model, the self-consistent mean-field (SCMF) approach presents a compromise between *ab initio* methods and macroscopic (mic-mac) models. The first kind of approaches, that start from a given nucleon-nucleon potential, are very effective in reproducing nucleon-nucleon scattering data, yet fail in predicting quantitatively the saturation point [4] if three-body interactions are not accounted for. Moreover, issues stem out when one tries to apply them in describing many-body systems. In contrast, mic-mac models can reproduce quite well some average trends, but are highly based on the phenomenology.

The next sections are dedicated to a brief overview of *ab initio* methods, mic-mac models,
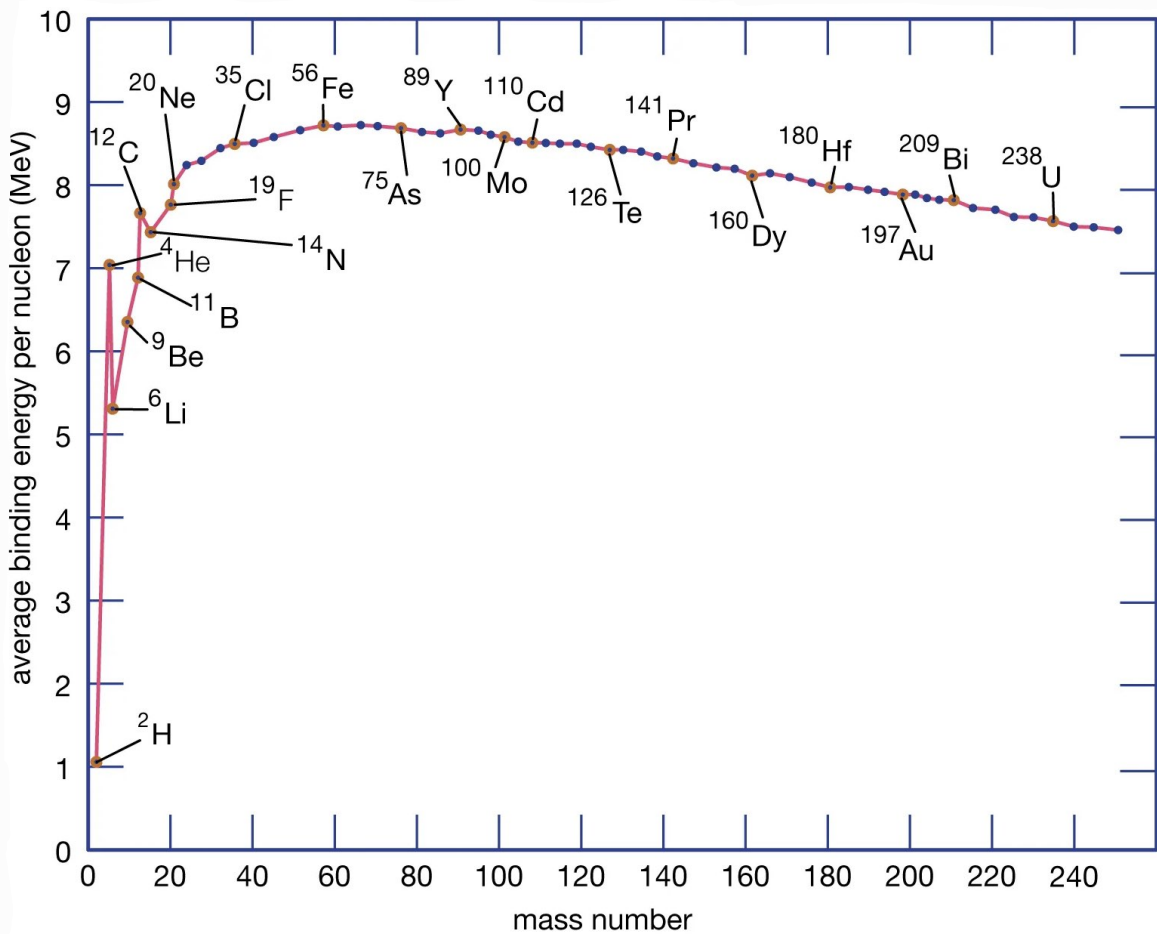
Figure 1.1: *© 2012 Encycloplædia Britannica, Inc.*
The average binding energy per nucleus as a function of the mass number.

and the Nuclear Shell Model, since several concepts discussed there might result instructive for the upcoming detailed exposition of the SCMF framework.

1.1.1 *Ab initio* methods

Ab initio methods accept few compromises to tackle the nuclear many-body problem. They look at nuclei as pure collections of nucleons that interact through realistic two- and three-body potentials, *e.g.*, the Argonne [5] or the Bonn potentials [6]. These realistic interactions are extremely effective at describing nucleon-nucleon scattering data and phase shifts. Of course, the price to be paid is the extremely high computational cost, which severely limits the range of applicability of the models only to light or, more recently, medium-sized nuclei.

The first mandatory step of any kind of *ab initio* method consists in specifying the Hamiltonian of the nuclear system as the sum of the non-relativistic kinetic energy, a two-body (NN) and a three-body (NNN) potential:

$$\mathcal{H} = \sum_i K_i + \sum_{i<j} V_{ij} + \sum_{i<j<k} V_{ijk} \, . \tag{1.2}$$

At this point, different theoretical approaches are employed to solve the Schrödinger equation for A nucleons with spin $s_i = \pm\frac{1}{2}$ and isospin $t_i = \pm\frac{1}{2}$ (proton or neutron). The many-body Schrödinger equation

$$\mathcal{H}\Psi(\vec{r}_1, \vec{r}_2, \ldots, \vec{r}_A; s_1, s_2, \ldots, s_A; t_1, t_2, \ldots, t_A) =$$
$$E\Psi(\vec{r}_1, \vec{r}_2, \ldots, \vec{r}_A; s_1, s_2, \ldots, s_A; t_1, t_2, \ldots, t_A) \, , \tag{1.3}$$

is a set of $2^A \binom{A}{Z}$ complex coupled equations in $3A - 3$ variables. Its approximate solution enables the calculation of basic features of finite nuclei: binding energies, excitation spectra, densities, systematic trends of charge radii in isotopic chains [7, 8], and so on. Three main methods exist to deal with the solution of Equation (1.3):

- Quantum Monte Carlo Methods [9] are used to perform a variation of the parameters of a wisely chosen trial wave function, in order to minimize the expectation value of the nuclear Hamiltonian

$$E_T = \frac{\langle \Psi_T \, | \, \mathcal{H} \, | \, \Psi_T \rangle}{\langle \Psi_T \, | \, \Psi_T \rangle} \geq E_0 \, . \tag{1.4}$$

  To obtain accurate enough results, Green's Function Monte Carlo techniques [10] are

needed to project the exact eigenfunction out of the trial wave funtion.

- The No-Core Shell Model [11, 12] interprets nuclei as systems of A point-like nucleons bound by realistic two- and three-body interactions. All nucleons are considered active (no-core), in contrast to what happens in standard shell model calculations (section 1.1.3). A large but finite harmonic oscillator (HO) basis, truncated by a total harmonic oscillator energy, is used to generate a model space. Thanks to this choice, one is able to use single-nucleon coordinates and wave functions

$$\phi_{nlm(\vec{r};b)} = R_{nl}(\vec{r};b)Y_{lm}(\hat{r}) \; , \tag{1.5}$$

where R_{nl} are the radial HO wave function, equations (1.17 - 1.21), and b is the harmonic oscillator length, related to the harmonic oscillator by the relation frequency,

$$b = \sqrt{\frac{\hbar}{m\Omega}} \; . \tag{1.6}$$

Second-quantization formalism is enabled, and the translational symmetry is never broken. On the other hand, the non-physical asymptotic behavior of the harmonic oscillator potential must be dealt with. The method considers an Hamiltonian of the type (1.2), but the inter-nucleon interaction, which acts on the full space, is renormalized via a similarity transformation to the reduced harmonic oscillator model space. The process generates an effective Hamiltonian which contains many-body terms. The renormalization is necessary to make the calculations as close as possible to the full space exact results, but also to improve the convergence rate.

- Chiral Effective Field Theory (χ-EFT) [13–15] recently became very popular, especially for precision calculations of light nuclei. The nuclear forces are derived as kernels of dynamical equations, order by order, within an EFT expansion [16]. Starting from a nucleon-pion system and the spontaneous breaking of chirality, the strong interaction Lagrangian is expanded in terms of small momenta. The model is based on solving the Hamiltonian with interactions between nucleons that are derived from QCD via symmetries. The approach has the advantage of explaining the hierarchy of many-body forces, estimating well theoretical uncertainties.

High performance computing, many-body methods with polynomial scaling, and ideas from

EFT are pushing the frontier of *ab initio* computations of nuclei. Recently, bulk properties of medium-mass and neutron-rich nuclei became accessible by using reference states that break rotational symmetry and keeping axial symmetry [17, 18].

Although NEDFs derived from effective forces obtained with *ab initio* calculations may never arrive to incorporate all the correlations necessary for a fine-tuning of the binding energies, several attempts are being done on this line of research, see [19] and references cited therein.

1.1.2 Macroscopic approaches

Mic-mac models try to obtain generic trends and nuclear features in an up-to-bottom philosophy. They claim that the available precise experimental knowledge represents a source of information that must be exploited as much as possible for predictive purposes. They begin with a simple framework inspired to the liquid drop model, and add *a posteriori* quantum, pairing, compressibility and finite-range effects. This allows to define very efficient models for a wisely chosen set of macroscopic features, and of course to keep the computational resources under control in favor of practical results.

The Strutinsky theorem [20, 21] establishes that the ground-state energy of a nucleus can be decomposed into the sum of two terms:

$$E = \bar{E} + \delta E \tag{1.7}$$

$$\delta E = \sum_{\alpha} \epsilon_{\alpha} - \int_{-\infty}^{\infty} \sum_{\alpha} g(\epsilon - \epsilon_{\alpha}) \,. \tag{1.8}$$

The major term, $\bar{E}$, smoothly varies with mass and atomic numbers, and can be accounted by the traditional liquid drop formula, Equation (1.1). The second term, δE, is instead built with a Gaussian smoothing function adjusted to the contributions related to the shell correction energy and to particle-particle correlations. The single-particle energies ϵ_{α} are computed by adopting a modified harmonic oscillator potential or a Woods-Saxon potential [22]. The key idea of mic-mac models is to parameterize $\bar{E}$, the smooth background energy, with the highest possible accuracy. The most important set of quantities used to this purpose is made of the degrees of freedom that describe the shape of the nuclear surface. The set of choices available in the literature for this parameterization is remarkably extended [23].

Mic-mac models, keeping macroscopic and microscopic effects well separated, have some

very clear practical advantages. For example, the estimation of zero-point energies can be directly fitted in the models. Different parametrizations can be used, devised and customized to deal with a specific problem. Relatively easy to be understood and programmed, they can also be very instructive with a view to SCMF approaches. In fact, a semi-classical approximation such as the Thomas-Fermi model [24, 25], possibly containing gradient corrections, can be used to get an estimate of the macroscopic energy (1.7) starting from a SCMF calculation. In general, the long history and the great number of interesting theoretical ideas present in mic-mac approaches should be constantly taken into account for possible future developments of SCMF approaches.

1.1.3 Nuclear Shell Model

The Nuclear Shell Model must be discussed, as it shares several key ideas with the SCMF framework. The approach is based on an independent particle picture, where nucleons are considered to be self-bound by the average of the two-body interactions over the states occupied by all other particles. The mean-field is static: dynamical corrections are neglected.

The average potential, denoted here $U(\vec{r})$, is usually taken as a standard phenomenological single-particle potential, and the shell model Hamiltonian reads

$$\mathcal{H} = \sum_{i=1}^{A}(K_i + U_i) + \frac{1}{2}\left(\sum_{i,j=1}^{A} V_{ij} - \sum_{i=1}^{A} U_i\right) \tag{1.9}$$

$$= \sum_{i=1}^{A} h_0(i) + \mathcal{H}_{\text{RES}} . \tag{1.10}$$

At the roughest approximation the single-nucleon average potential may be a square-well potential or an harmonic oscillator potential, in spherical symmetry; In the former case,

$$U(r) = \begin{cases} U_0 & \text{if } |r| < R \\ +\infty & \text{if } |r| \geq R , \end{cases} \tag{1.11}$$

and the corresponding eigenfunctions of the Schrödinger equation are

$$\Psi_{nlm}(\vec{r}) = N_{nl} j_l(k_{nl}r) Y_{lm}(\theta, \phi) , \tag{1.12}$$

where N_{nl} is a normalization constant, j_l are Bessel functions, while Y_{lm} are the spherical

harmonics built via the associated Legendre polynomials $P_l^m(x)$,

$$Y_l^m(\theta, \phi) = \sqrt{\frac{2l+1}{4\pi}\frac{(l-m)!}{(l+m)!}}P_l^m(\cos\theta)e^{im\phi} \tag{1.13}$$

$$P_l^m(x) = \frac{(-1)^m}{2^l l!}(1-x^2)^{\frac{m}{2}}\frac{d^{l+m}}{dx^{l+m}}(x^2-1)^l . \tag{1.14}$$

The eigenfunctions must vanish at the boundary R of the square-well potential, condition leading to the requirement that $k_{nl}R = X_{nl}$ must be the n-th zero of the l-th Bessel function. The corresponding eigenenergies,

$$\epsilon_{nl} = \frac{\hbar^2}{2m}k_n l - U_0 , \tag{1.15}$$

determine the nuclear energy levels.

If the average potential is taken as a three-dimensional spherical harmonic oscillator,

$$U(r) = \frac{1}{2}m\omega_0^2 r^2 , \tag{1.16}$$

one starts from the *Ansatz*

$$\Psi_{nlm}(\vec{r}) = \frac{u_{nl}(r)}{r}Y_{lm}(\theta, \phi) . \tag{1.17}$$

The resulting Schrödinger equation reads

$$\left[-\frac{\hbar^2}{2m}\frac{d^2}{dr^2} + U(r) + \frac{\hbar^2 l(l+1)}{2mr^2} - (\epsilon_{nl} + U_0)\right], \tag{1.18}$$

which is solved by

$$u_{nl}(r) = N_{nl}q^{l+1}e^{-q^2/2}L_{n-1}^{l+1/2}(q^2) \tag{1.19}$$

$$L_p^a(z) = \frac{\Gamma(a+p+1)e^z}{\Gamma(p+1)z^a}\frac{d^p}{dz^p}z^{a+p}e^{-z} \tag{1.20}$$

$$N_{nl} = \frac{2(n-1)!}{b[\Gamma(n+l+\frac{1}{2})]^3} , \tag{1.21}$$

where $L_p^a(z)$ are the generalized Laguerre polynomials, $b = \sqrt{\frac{\hbar}{m\omega_0}}$ is the harmonic oscillator length, and $q = \frac{r}{b}$. Finally, the energy levels

$$\epsilon_{nl} = \hbar\omega_0(N + \frac{3}{2}) - U_0 , \tag{1.22}$$

with $N = 2(n-1) + l$, are the equally spaced oscillator shells. A semi-empirical value for the level spacing is $\hbar\omega_0 = 41A^{-\frac{1}{3}}$MeV, estimated to fit mean-square radii of nuclei.

Even if a realistic average nuclear single-particle potential should have a finite depth, the two previous approximations yield acceptable predictions of low-lying energy levels. The square-well potential tends to predict stronger bindings than the harmonic oscillator potential. Having defined the shell configuration of nucleons, one finds that a special stability is reached for closed-shell configurations. In particular, the highest stability is found in correspondence of numbers of protons or neutrons equal to 2, 8, 20, 28, 50, 82, 126. Nuclei with such number of each type of fermions are called magic, and they are characterized by spherical symmetry and absence of pairing effects. Unfortunately, both the harmonic oscillator and the square-well shell model correctly predict only the first three shell-closures.

It was then proposed [26] to add a spin-orbit term $\zeta(r)(\vec{l} \cdot \vec{s})$ to the average single-nucleon potential. The spin-orbit correlation is an intrinsically relativistic effect that provokes a splitting and shifting of the energy levels, and allows to explain the observed nuclear magic numbers. The term is way more relevant that in the atomic case, and its presence leads to the appearance of a splitting of levels characterized by different total angular momentum $\vec{j} = \vec{l} + \vec{s}$. In the case of nuclear bindings the spin-orbit levels with higher j for a given orbital momentum l are found to lie lower in energy. To account for this evidence, the spin-orbit interaction must be attractive, meaning that the coupling constant $\zeta(r)$ must be negative. The best choice for the quantum numbers to treat the spin-orbit term is the coupled basis, $\left|nl\frac{1}{2}jm_j\right\rangle$. The first-order splitting is equal to

$$\epsilon_{l-\frac{1}{2}} - \epsilon_{l+\frac{1}{2}} = -\zeta nl\frac{2l+1}{2} \tag{1.23}$$

where $\zeta_{nl} = \int dr \, u_{nl}^2(r)\zeta(r)$.

In practical calculations one considers an Hamiltonian composed of an inert closed-shell core and a separated band of valence nucleons around the Fermi energy. The core properties are described by a single-particle average potential $U(r)$, such as the two previously discussed. Then, one performs a configuration-mixing calculation that involves all many-body states that can be constructed within the model space used to describe the valence band [27]. The Nuclear Shell Model has the ability to describe simultaneously all spectroscopic properties of low-lying states with very different structure within a nucleus. On the other hand, the effective interactions strongly depend on the choice of the active shells and on the truncation scheme. Shell model calculations of nuclei very far from stability are therefore unreliable, since numerical costs grow

explosively with the model space size.

1.2 Self-Consistent Mean-Field Model

In the same fashion of the Nuclear Shell Model, the Self-Consistent Mean-Field approach [28] is based on the independent particle picture. The resulting mean-field is however generated in a self-consistent way, after a global effective interaction, suitable to the study of all nuclei, has been adopted. Once this effective interaction is defined, the nuclear many-body problem is solved at a certain level of approximation, *e.g.*, the Hartree-Fock or Hartree-Fock-Bogoliubov approximation.

The approach enables a description of the nuclear many-body problem in terms of a universal nuclear energy density functional (NEDF). The term universal means that the functional has the same form for all nuclei through the chart of nuclides. An important class of them are relativistic NEDFs, whose applications have reached an accuracy level comparable to their non-relativistic counterparts, based on Skyrme or Gogny effective interactions.

It is also necessary to extend the framework to include correlations originating from the restoration of broken symmetries (translational, rotational, particle number) and from fluctuations of the collective coordinates. Such collective correlations cannot be included in a universal NEDF, because of their high sensitivity to shell effects and pronounced variations with particle number. Hence, a second level of the NEDF framework considers collective correlations via the restoration of broken symmetries and configuration mixing of symmetry-breaking product states. The NEDF is then constructed as a functional of all transition density matrices that can be obtained from the chosen set of product states. This set is chosen with the purpose of restoring symmetries and/or to perform mixing of configurations corresponding to specific collective modes, *e.g.*, QRPA [29], GCM [30], collective Hamiltonian model [31].

The upcoming sections are devoted to a detailed exposition of the framework: the Hartree-Fock-Bogoliubov and relativistic Hartree-Bogoliubov formalism, the construction of the NEDF with the possible choices for the effective force, and a final brief overlook to the landscape of beyond-mean-field approaches.

1.2.1 Pairing correlations

The staggering trend that characterizes the one-neutron separation energies [32] shows that even-even nuclei are significantly more bound than their odd-A neighbors. The energy gap $\Delta \approx 2$ MeV between the ground-state and the lowest single-particle excitation of even-even

nuclei can be explained by the presence of a residual bond between pairs formed within the last shell. These are some of the many empirical evidences that point to the existence of a strong, short-range, attractive particle-particle residual nuclear force: the pairing force. In the framework of nuclear physics, pairing correlations cannot be treated in a perturbative way as it is done in atomic physics. Pairing even arrives to impact dynamical properties, such as the value of nuclear momenta of inertia [33].

The relevance of pairing for nuclear structure makes the Hartree-Fock (HF) level of approximation highly inadequate. Specifically, properties of open-shell and deformed nuclei cannot be properly reproduced without taking it into account. To obtain solid results, it is necessary, at the very least, to add pairing effects on top of the results provided by the HF approximation. This can be done by means of the BCS[1] theory: the BCS equations are solved starting from a set of solutions of the HF problem. This level of approximation is valid in the case of time-reversal-invariant systems, namely for even-even nuclei. A Kramers energy degeneracy of time-conjugated single-particle states, $\epsilon_n = \epsilon_{\bar{n}}$, is then present. Because of this, within the HF+BCS approximation, the pairing field Δ is diagonal in the same basis that diagonalizes the mean-field h.

The inclusion of pairing *a posteriori* may have an impact on the HF mean-field potential, for example by shifting the energy minimum to become less deformed than it actually is. The HF+BCS level of approximation holds very well for the description of spherical and deformed nuclei not too far from stability. In fact, usually the constant-gap approximation is adopted: densities are calculated using BCS occupation factors with the gap parameter Δ being determined from empirical mass differences. However, for exotic nuclei far from the valley of stability, masses are often unknown, and, most important, the BCS model only provides a poor approximation. In such a case, the BCS treatment gives completely wrong predictions for observables related to the nucleon density. For instance, it predicts a dramatic increase of neutron radii for neutron-rich open-shell nuclei.

A more robust and elegant way to consider pairing correlations consists in incorporating a pairing field in the Hamiltonian of the system, treating the pairing interaction and the mean-field on an equal footing. This unified description can be achieved at the level of the Hartree-Fock-Bogoliubov (HFB) approximation [34, 35], or, in the relativistic case, the relativistic Hartree-Bogoliubov (RHB) approximation [36,37]. Both will be discussed in the next section. An ample

---

[1]Bardeen-Cooper-Schrieffer

exposition of the nuclear BCS theory can instead be found in [38] and in references therein.

1.2.2 Hartree-Fock-Bogoliubov and relativistic Hartree-Bogoliubov formalism

Let the single-nucleon wave functions be denoted by $\psi_i(\vec{x})$, $\vec{x} = (\vec{r}, s_i, t_i)$, with $i = 1, \ldots, N_{\mathrm{wf}}$ and $N_{\mathrm{wf}} \geq A$. Consider the creation operator $a_i^\dagger$ of a nucleon in the state $\psi_i(\vec{x})$.

The HF method considers the total wave function of the nucleus, $|\Phi\rangle$, to be a Slater determinant of the single-nucleon states ψ_i. Occupied states satisfy $a_i^\dagger |\Phi\rangle = 0$ for $i = 1, \ldots, A$, and $a_i |\Phi\rangle = 0$ for $i > A$.

The Hartree-Fock-Bogoliubov (HFB) formalism incorporates instead particle-particle correlations with the will of sticking to the independent particle picture of the nucleus. This can be done by shifting the object of study from particles to quasiparticles, whose creation operators are defined by the Bogoliubov transformation as a general linear superposition of particles operators:

$$b_n^\dagger = \sum_i U_{in} a_i^\dagger + V_{in} a_i \ . \tag{1.24}$$

The Bogoliubov transformation connects the single-nucleon states to the quasiparticle states. In the matrix notation, Equation (1.24) reads

$$\begin{bmatrix} b \\ b^\dagger \end{bmatrix} = \mathcal{W}^\dagger \begin{bmatrix} a \\ a^\dagger \end{bmatrix} \ , \tag{1.25}$$

where the Bogoliubov matrix

$$\mathcal{W} = \begin{bmatrix} U & V^* \\ V & U^* \end{bmatrix} \tag{1.26}$$

is unitary[2]. The nuclear ground-state is given by the quasiparticle vacuum condition,

$$b_n |\Phi\rangle = 0 \tag{1.27}$$

for all n.

Treating the mean-field and the pairing correlations at the same level means that the energy

---

[2]The unitary condition of the Bogoliubov matrix implies $U^\dagger U + V^\dagger V = 0$, $UU^\dagger + V^* V^\intercal = 0$, $U^\intercal V + V^\intercal U = 0$, and $UU^\dagger + V^* U^\intercal = 0$.

functional must not depend only on the single-particle density matrix, the normal density

$$\varrho_{ij} = \left\langle \Phi \,\middle|\, a_j^\dagger a_i \,\middle|\, \Phi \right\rangle = \varrho_{ji}^* \,, \tag{1.28}$$

but also on the pairing tensor, the abnormal density

$$\kappa_{ij} = \left\langle \Phi \,\middle|\, a_j a_i \,\middle|\, \Phi \right\rangle = -\kappa_{ji} \,. \tag{1.29}$$

In terms of the Hartree-Fock-Bogoliubov matrices, they read

$$\varrho = V^* V^T \tag{1.30}$$

$$\kappa = V^* U^T \,. \tag{1.31}$$

The density matrix and the pairing tensor can be combined to build the generalized density matrix

$$\mathcal{R} = \begin{bmatrix} \varrho & \kappa \\ -\kappa^* & 1 - \varrho^* \end{bmatrix} \,, \tag{1.32}$$

which is Hermitian, $\mathcal{R}^\dagger = \mathcal{R}$, idempotent, $\mathcal{R}^2 = \mathcal{R}$, and has eigenvalues equal to either 0 or 1. Thanks to this definition, most of the formalism and rules originally developed within the Hartree-Fock scheme can be generalized to the Hartree-Fock-Bogoliubov framework by simply working with the generalized density and the Bogoliubov matrices in place of the normal density and single-nucleon wave functions. As a first useful application of this concept, the equation of motion for the matrix $\mathcal{R}$ (1.32) reads

$$i\partial_t \mathcal{R}(t) = [\mathcal{H}, \mathcal{R}(t)] \,, \tag{1.33}$$

where the generalized Hamiltonian $\mathcal{H}$ is calculated as the functional derivative of the energy with respect to the generalized density:

$$\mathcal{H} = \frac{\delta E}{\delta \mathcal{R}} \,. \tag{1.34}$$

The ground-state of an open-shell even-even (time-reversal invariant) nucleus is then described

by the stationary limit of Equation (1.33),

$$[\mathcal{H}, \mathcal{R}] = 0 . \tag{1.35}$$

The nuclear ground-state $|\Phi\rangle$ can be calculated by minimizing the total energy

$$E = \langle \Psi \,|\, \mathcal{H} \,|\, \Psi \rangle = E[\varrho, \kappa] , \tag{1.36}$$

with a constraint on the proton and neutron numbers N_t. It will be clear below, within the more general framework of Density Functional Theory, that not only the energy, but all one-body operators, can be expressed in terms of one-body densities, only. The minimization of the Routhian

$$E[\lambda] = E - \lambda_t \langle \Psi \,|\, \mathcal{N}_t \,|\, \Psi \rangle \tag{1.37}$$

leads to the HFB equations, expressed in terms of the matrices U and V

$$\mathcal{H} \begin{bmatrix} U_n \\ V_n \end{bmatrix} = E_n \begin{bmatrix} U_n \\ V_n \end{bmatrix} \tag{1.38}$$

$$\mathcal{H} = \begin{bmatrix} h - \lambda_t & \Delta \\ -\Delta^* & -h + \lambda_t \end{bmatrix} , \tag{1.39}$$

The Hamiltonian is composed of three ingredients: the self-consistent mean-field h, responsible for long-range particle-hole interactions, the pairing field Δ, accounting for particle-particle short-range correlations, and the chemical potentials λ_t, the Lagrange multipliers associated to the constraint that the expectation values of the particle number operators N_t equal the number of protons and neutrons. The mean-field and the pairing field are respectively defined by

$$h_{ij} = \frac{\delta E}{\delta \varrho_{ji}} = h_{ji}^* \tag{1.40}$$

$$\Delta_{ij} = \frac{\delta E}{\delta \kappa_{ij}^*} = -\Delta_{ji} . \tag{1.41}$$

The quasiparticle energies E_n can also be viewed as Lagrange multipliers that enforce the orthonormality of the quasiparticle states. This concept will be developed and clarified in the implementation of the Constrained Variation method for the solution of the inverse Kohn-Sham problem, section 2.1.2.

Given a Hamiltonian $\mathcal{H} = \mathcal{T} + \mathcal{V}$, $\mathcal{V}$ being a two-body effective interaction composed by a particle-hole channel $V^{(ph)}$ and a particle-particle channel $V^{(pp)}$, the definitions above lead to the following expression for the mean-field,

$$h_{ij} = T_{ij} + \sum_{kl} V^{(ph)}_{ijkl} \varrho_{lk} \, , \tag{1.42}$$

and for the pairing field

$$\Delta_{ij} = \frac{1}{2} \sum_{kl} V^{(pp)}_{ijkl} \kappa_{kl} \, . \tag{1.43}$$

Different bases may be used to express the solution of the HFB equation:

- The quasiparticle basis that diagonalizes the generalized density $\mathcal{R}$.

- The canonical basis diagonalizes the density operator ϱ and sets the pairing tensor κ in its canonical form, obtained thanks to the fact that the U matrix becomes diagonal and the V matrix gets decomposed into 2×2 anti-diagonal sub-matrices. The transformation to the canonical basis determines the energies and occupation probabilities of single-nucleon states. The localization of the canonical basis enables the description of the bound states and the single-particle continuum [39].

- The HF basis is the one in which the mean-field h is diagonal.

At this point is indeed worth mentioning the HFBTHO code [40], able to solve the HFB problem with Skyrme and Gogny forces by expanding the nuclear states on the harmonic oscillator basis in cylindrical coordinates. Advanced symmetry restoration techniques (section 1.2.4) for particle number, reflection and rotational symmetry are implemented. The software can be also used to calculate several nuclear fission related properties (refer to chapter 3), such as the nuclear collective inertia, the fission fragment charge, mass and deformations based on the determination of the fission neck.

The relativistic generalization of the HFB formalism, leading to the relativistic Hartree-Bogoliubov (RHB) equations, is straightforward. Again, the relativistic mean-field energy functional is extended to include the pairing tensor in addition to the density matrix and the meson fields ϕ_m. This is accomplished by adding the pairing energy

$$E_{pair}[\hat{\kappa}] = \frac{1}{4} \text{Tr} \left[\kappa^* V^{(pp)} \kappa \right] \tag{1.44}$$

to the NEDF:

$$E[\varrho, \kappa, \phi_m] = E_{RMF}[\varrho, \phi_m] + E_{pair}[\kappa] \ . \tag{1.45}$$

The generalized Hamiltonian is defined in the same way as Equation (1.34), with the Dirac mean-field relacing the mean-field h. The Dirac mean-field and the pairing field are, again, integral operators with the kernels of equations (1.42) and (1.43), but the indexes now denote quantum numbers that specify the Dirac indexes of the spinors. The RHB equations are solved via the diagonalization of the generalized Hamiltonian $\mathcal{H}$, as in Equation (1.38). The generalized density matrix $\mathcal{R}$ is constructed from the eigenvectors of $\mathcal{H}$.

The dimension of the HFB (RHB) matrix equation is twice that of the corresponding Schrödinger (Dirac) equation. For each eigenvector (U_n, V_n) with positive quasiparticle energy $E_n > 0$, there exists an eigenvector (V_k^*, U_k^*) with opposite quasiparticle energy. However, the quasiparticle operators must satisfy fermion commutation relations, and the levels $\pm E_n$ cannot be occupied simultaneously. For the solution that corresponds to the ground-state of a nucleus with even particle number, one commonly chooses the eigenvectors with positive eigenvalues E_n.

Among the available codes able to solve the relativistic Hartree-Bogoliubov (RHB) equations it is worth mentioning the DIRHB code [41], able to solve the relativistic equations for spherical, cylindrical, and triaxial systems. State-of-the-art relativistic nuclear energy density funtionals are implemented in the suite, enabling precise calculations throughout the whole nuclear chart. The routine calculates the mean-field solution of the nuclear many-body problem for even-even open-shell nuclei. The relativistic RHB equations are solved in a self-consistent iteration scheme. The method combines the coordinate space and the harmonic oscillator configuration representations. The diagonalization of the RHB matrix, Equation (1.38), gives access to the RHB amplitudes U_n and V_n and to the single-quasiparticle energies E_n. The normal and abnormal densities built from the wave functions are first calculated in the configurational harmonic oscillator space and afterwards transformed to the coordinate space. The density and the pairing tensor in the coordinate space are used to calculate the potentials used in the next iteration of the routine. It is possible to constrain the solution to reproduce the desired value of some operators. This can be done by following the the method of the Lagrange multiplier. A remarkable example of this procedure is the Multiple Constraint Method, implemented in this work and discussed in appendix B.

1.2.3   Nuclear energy density functionals

The specific functional form of the NEDF used within the HFB or RHB formalism is obtained by adopting an effective interaction. There exist mainly three possible choices for the form of the effective interaction, but several hundreds of different parameterizations of them are available on the market. Effective interactions may differ for the choice of the nuclear data they are fitted to, as well as for the level of empiricity of the techniques with whom they are derived.

The most straightforward choice for the effective interaction, justified by the short range of the nuclear forces and by the long wavelength of the single-nucleon states, consists of an expansion in terms of zero-range, delta-shaped, contact forces. Following this idea, one obtains the so-called Skyrme-type interactions [42]. A simplified version of state-of-the-art Skyrme energy density functionals, useful to catch the idea that lies behind all of them, is the following:

$$
\begin{aligned}
V_{\text{pseudo-Skyrme}}(|\vec{r}_1 - \vec{r}_2|) = {} & t_0 \delta(|\vec{r}_1 - \vec{r}_2|)(1 + x_0 P_s) \\
& + \frac{t_3}{6} \delta(|\vec{r}_1 - \vec{r}_2|)(1 + x_3 P_s)\varrho^\alpha\left(\frac{\vec{r}_1 + \vec{r}_2}{2}\right),
\end{aligned}
\tag{1.46}
$$

where t_0, t_3, x_0, x_3, and α are the above mentioned fit parameters of the interaction, whereas $P_s = \frac{1 + s_1 \cdot s_2}{2}$ is the spin exchange operator. The interaction explicitly depends on the density: at this point of the exposition, this is just a semi-empirical necessity based on the fact that several nuclear properties, such as the incompressibility and the effective mass, cannot be reproduced without a density-dependence of the effective force. In section 1.3, the framework of Density Functional Theory will provide a solid theoretical background to this feature. State-of-the-art functionals may as well contain terms proportional to gradients of the density up to a given order, effectively making the interaction velocity-dependent [43].

A different possible choice for the effective interaction, first proposed in [44], is the following:

$$
V_{\text{Brink-Boeker}}(|\vec{r}_1 - \vec{r}_2|) = \sum_{i=1,2} S_i(1 - m_i + m_i P_M)e^{-\frac{|\vec{r}_1 - \vec{r}_2|^2}{\mu_i^2}},
\tag{1.47}
$$

where S_i, m_i, μ_i are parameters, and P_M is the Majorana operator that exchanges the coordinates of two interacting nucleons. Later on, this simple interaction has been refined [45] by adding new terms and parameters and including density-dependencies and a spin-orbit term. Named Gogny-type interaction, it relies on finite-range, Gaussian-shaped forces. One of the main advantages of the Gogny interaction is the possibility of using it both in the particle-hole

and in the particle-particle channels. In fact, finite-range interactions avoid the divergence problem that affects zero-range forces in the pp-channel of the interaction.

Finally, a last important class is that of the relativistic nuclear energy density functionals, developed to make up for the empirical assumptions of their non-relativistic counterparts. As an example, the necessity of Skyrme and Gogny interactions to include a spin-orbit term *ad hoc*. The starting point is a covariant Lagrangian that contains the nucleonic degrees of freedom. Relativistic mean-field (RMF) models [46–48] use coupling constants as parameters to be fitted to data of nuclear matter or finite nuclei. In this framework, one usually neglects exchange-correlation (Fock) potentials, as they are absorbed by the phenomenological fit of the coupling constants, as well as the contribution of the antiparticles to the mesonic fields (no-sea approximation). While non-relativistic NEDFs treat the spin-orbit potential as a completely phenomenological addition, relativistic NEDFs automatically incorporate spin and the spin-orbit potential terms with the proper strength, via the constructive combination of the scalar long-range attractive field and the vector short-range repulsive field. In fact, as already mentioned in section 1.1.3, the energy spacing between spin-orbit partner states can become as large as the gaps between major shells, and the strong coupling between the orbital angular momentum and nucleon spin is fundamental to obtain correct magic numbers and shell gaps. RMF are thus calculated from the nucleonic wave-functions, now four-components Dirac spinors, by iteratively solving the RHB equations. RMF models can reproduce binding energies and charge radii across the nuclear table, as well as density distributions comparable with those obtained in electron scattering experiments [49]. One of the main issues of the model, the inability to reproduce nuclear matter incompressibility, can be solved by including nonlinear self-coupling of the sigma-field [50]. Several other ground-state properties have been calculated, such as single-particle spectra of adjacent odd-mass nuclei, magnetic moments [51], and excited collective states [52]. In general one chooses between effective point-coupling (PC) zero-range forces and effective finite-range interactions based on meson-exchange (ME). A remarkable example of a relativistic energy density functional is the DD-PC1 [53], Equation (2.85), in which only nucleon degrees of freedom are explicitly used for the construction of effective interaction terms. A phenomenological form for the density-dependence is also present. The set of parameters of the functional is adjusted in a χ^2-fit to the experimental masses of sixty-four axially deformed nuclei in the mass regions $A \approx 150 - 180$ and $A \approx 230 - 250$. The resulting functional is further tested in calculations of binding energies, charge radii, deformation parameters, neutron

skin thickness, and excitation energies of giant monopole and dipole resonances. During the last decade the functional DD-PC1 has successfully been applied in a number of studies of various nuclear phenomena, from ground-state properties to the description of collective spectra, giant resonances, shape-phase transitions and the dynamics of nuclear fission.

For the pp-channel, both in the case of Skyrme and relativistic EDF, a phenomenological non-relativistic pairing interaction is adopted. In the RMF case, the pairing field Δ can be written in the form

$$\Delta = \left(\begin{array}{cc} \Delta_{++} & \Delta_{+-} \\ \Delta_{-+} & \Delta_{--} \end{array} \right) \tag{1.48}$$

by separating the large and the small components of the quasiparticle wave functions. Calculations of finite nuclei [54] show that the off-diagonal blocks Δ_{-+} and Δ_{+-}, which couple large and small components, are considerably smaller than the matrix elements of the corresponding off-diagonal term of the Dirac mean-field h_D. Moreover, as the pairing properties are determined in an energy window of a few MeV in proximity of the Fermi surface, also Δ_{--} plays no relevant role on pairing in finite nuclei. Thus, in the RHB equations, one uses a non-relativistic potential in the calculation of the field Δ_{++}. To avoid divergence problems that would require introducing an additional energy cut-off parameter, it was suggested [55] that the pairing part of the Gogny force [56] could be employed in the RHB model.

1.2.4 Beyond mean-field methods

The *leitmotiv* of all extensions of the SCMF model is the desire to stick to the independent particle picture. This is the idea that leads to the definition of linear combination of single-nucleon states, that is to the concept of quasiparticle. This way, the independent particle picture manages to thoroughly account for pairing effects without waiving the possibility of describing the total ground-state wave function in the form of a Slater determinant. The advantage of this representation is the straightforward implementation of the anti-symmetrization principle for identical particles, as well as the applicability of the Wick's theorem used for the evaluation of the matrix elements of many-body operators.

Of course there is a price that has to be paid in exchange. On one hand, the linear many-body Schrödinger equation becomes a set of non-linear, density-dependent one-body mean-field equations. The numerical methods used to solve them are therefore conceptually more advanced and require the implementation of iterative-based routines and smart mixing procedures. On the other hand, the independent particle picture is preserved at the expense of breaking several sym-

metries of the underlying Hamiltonian. In particular, consider the HFB equations, summed up by the synthetic condition (1.35) of commutation between the Hamiltonian and the generalized density. Given a symmetry $\mathcal{S}$, consider the transformation

$$\mathcal{H}[\bar{\mathcal{R}}] = \mathcal{S}\mathcal{H}[\mathcal{R}]\mathcal{S}^\dagger \; ; \tag{1.49}$$

the symmetry is broken if $[\mathcal{H}, \mathcal{S}] \neq 0$, which implies $\bar{\mathcal{R}} \neq \mathcal{R}$.

In the HFB and RHB models, the translational, rotational, particle number, and reflection symmetries are broken. Nonetheless, breaking symmetries is a price worth paying, since correlations between nucleons might have not been taken into account while requiring, at the same time, for the mean-field and wave functions to respect the symmetries of the underlying Hamiltonian. For instance, the desire to stick to translational-invariant, product-type, wave functions, would force one to make use of plane waves, definitely inadequate to seize a fine-size cluster of nucleons. This means that constraining the symmetries *a priori* actually reduces the flexibility of the model. The answer to the symmetry dilemma, namely choosing between lower-energy states that break symmetries or good quantum numbers that bring along higher energies, is obvious.

If the concept of symmetry-breaking enables a description of dynamical correlations on top of simple product-type states, on the other hand, the mean-field wave functions cannot be labeled anymore by good quantum numbers, and, most important, cannot be used as they are to calculate quantities comparable to experimental data. Another drawback is the sharp transitions between symmetry-conserving and symmetry-breaking solutions that may appear as a function of parameters of the Hamiltonian. This is the case, for instance, of the phenomenon of pairing collapse of the nuclear momentum of inertia at high angular momentum [57].

There exist several techniques apt to restore broken symmetries, based on the linear superposition of the degenerate deformed HFB or RHB wave functions to project out components with good quantum numbers. These procedures lower the energy of the mean-field solution by lifting its degeneracy and represent a step beyond the mean-field approximation. Symmetry restoration [58] may be applied after the HFB or RHB variation has been carried out. This is a relatively simple method to implement it at the cost of loosing the warranty that the projected energy corresponds to a minimum of the projected potential energy surface. Otherwise, one projects the HFB or RHB equation before the minimization process. This way, intrinsic states for each quantum number of the restored symmetry are obtained. The cost of the latter

procedure is unfortunately much higher and can be applied only to medium-sized nuclei. This computational challenge led to the development of several approximate methods for symmetry restoration, useful to deal with systems characterized by triaxiality or weak symmetry breaking[3]. In particular, the Lipkin [59], the Lipkin-Nogami [60], and the Kamlah [61] methods are all based on the idea of approximating the kernels of operators between deformed states, giving access to the matrix elements of symmetry-projected states.

1.3   Density Functional Theory

At this point, the important role played by nuclear energy density functionals in the study of nuclear matter should be clear. Since the very first works on NEDFs, it has been noticed that a density-dependence of the effective potentials is necessary to the aim of reproducing basic many-body properties of nuclear structure. This semi-empirical feature has a sound explanation within the framework of nuclear Density Functional Theory. The charm of the theory lies in the possibility of predicting, in principle exactly, the ground-state properties of the system under investigation. Moreover, the computational cost that must be paid is surprisingly low. The advantage of dealing with the density, a function of three space variables, in place of the cumbersome many-variable total wave function, is evident. DFT, given the knowledge of the nuclear density of the physical system of interest, gives then access to the study of systems that can be very large in the sense of their degrees of freedom.

The nuclear density is defined as the number of nucleons per unit of volume in a given state Ψ,

$$\varrho(\vec{r}_1) = A \int \cdots \int ds_1 d\vec{x}_2 \ldots d\vec{x}_A |\Psi(\vec{x}_1, \ldots, \vec{x}_A)| \,, \tag{1.50}$$

and it integrates up to the total number of nucleons in the system, that is

$$\int d\vec{r}_1 \, \varrho(\vec{r}_1) = A \,. \tag{1.51}$$

For a more general definition of the nuclear density, the reader may refer to appendix A.

1.3.1   Hohenberg-Kohn theorems

The Thomas-Fermi model was the first to suggest the possibility of determining the energy of an electronic system as an approximate functional of the density, only. For decades, the

---

[3]In this case, a large number of eigenstates of the symmetry generators are mixed up in the broken-symmetry state, increasing the computational resources required.

Thomas-Fermi model has been thought to be oversimplified, because of its very limited predictive power mainly due to its strong assumptions. The idea of treating the properties of a system as functionals of the density alone was later developed by Hohenberg and Kohn. In [62], they provided three fundamental theorems, that showed that the Thomas-Fermi model might be as well thought as an approximation of a many-body exact theory: Density Functional Theory.

The determination of the ground-state energy and wave function of a given fermion system requires both the knowledge of the number A of the particles composing the system, and that of the external potential $v(\vec{r})$ to which the system is subject. The first Hohenberg-Kohn (HK) theorem justifies the usage of the local density $\varrho(\vec{r})$ as a basic variable, in place of A and $v(\vec{r})$. It is evident that the density uniquely determines the number A of particles in the system. Way more remarkable is the fact that also the external potential $v(\vec{r})$ can be identified, up to an arbitrary constant, by the information encoded in the density. The inter-particle interaction and the kinetic term are instead fixed once one considers a specific type and number of fermions. These are some of the consequences of the HK theorems:

HK1 Given a system of A interacting particles, described by the Hamiltonian

$$\mathcal{H} = \mathcal{T} + \mathcal{V} + \mathcal{W} = -\sum_{i=1}^{A} \frac{\nabla_i^2}{2m_i} + \sum_{i=1}^{A} v(\vec{r}_i) + \sum_{i \neq j}^{A} w(\vec{r}_i, \vec{r}_j) \,, \qquad (1.52)$$

the A-body wave function Ψ, and the corresponding density calculated according to Equation (1.50), the non-degenerate ground-state wave function is a unique functional of the ground-state density:

$$\Psi_0(\vec{r}_1, \ldots, \vec{r}_A) = \Psi[\varrho_0(\vec{r})] \,. \qquad (1.53)$$

As a consequence, the ground-state expectation value of each observable is a functional of the nuclear density, alone.

Proof. The density trivially determines A by quadrature. The fact that the expectation value of each observable is a functional of the nuclear density is shown in appendix A. It is then just necessary to demonstrate that the density determines $v(\vec{r})$. Suppose there were two external potentials, v and v', differing by more than just an arbitrary constant, related to the same ground-state density $\varrho(\vec{r})$, solution of the Schrödinger equation. Then, two different Hamiltonians $\mathcal{H}$ and $\mathcal{H}'$ would exist, their ground-state densities being the same, and yet the normalized wave functions Ψ and Ψ' would be different. Let Ψ' be a

trial wave function for the $\mathcal{H}$ problem and vice versa:

$$E_0 < \langle \Psi' \,|\, \mathcal{H} \,|\, \Psi' \rangle = \langle \Psi' \,|\, \mathcal{H}' \,|\, \Psi' \rangle + \langle \Psi' \,|\, \mathcal{H} - \mathcal{H}' \,|\, \Psi' \rangle =$$

$$= E_0' + \int d\vec{r}\, \varrho(\vec{r})(v(\vec{r}) - v'(\vec{r})) \tag{1.54}$$

$$E_0' < \langle \Psi \,|\, \mathcal{H}' \,|\, \Psi \rangle = \langle \Psi \,|\, \mathcal{H} \,|\, \Psi \rangle + \langle \Psi \,|\, \mathcal{H}' - \mathcal{H} \,|\, \Psi \rangle =$$

$$= E_0 + \int d\vec{r}\, \varrho(\vec{r})(v'(\vec{r}) - v(\vec{r})) \,. \tag{1.55}$$

This leads to an absurd. There cannot be two different potentials v providing the same ground-state density ϱ. $\qquad\square$

HK2 For a given external potential $v(\vec{r})$ to which the system is subject, there exists a universal functional $F[\varrho]$, such that the total energy density functional reads

$$E_v[\varrho] = F[\varrho] + V[\varrho] = T[\varrho] + W[\varrho] + V[\varrho]. \tag{1.56}$$

The HK functional $F[\varrho]$ is universal for a given particle-particle interaction and for a given number of particles in the system, since it does not depend on the external potential $v(\vec{r})$.

HK3 For a given density $\tilde{\varrho}(\vec{r})$ such that

$$\tilde{\varrho}(\vec{r}) \geq 0 \tag{1.57}$$

$$\int \tilde{\varrho}(\vec{r}) = A \tag{1.58}$$

The ground-state energy is a global minumum of the total energy:

$$E_0 = E_v[\varrho] \leq E_v[\tilde{\varrho}]. \tag{1.59}$$

Proof. Because of the first HK theorem, $\tilde{\varrho}(\vec{r})$ determines the potential $\tilde{v}$ up to an arbitraty constant and the total wave function $\tilde{\Psi}$ up to a phase factor. Consider $\tilde{\Psi}$ as a trial wave function of the $\mathcal{H}$ problem

$$\left\langle \tilde{\Psi} \,\middle|\, \mathcal{H} \,\middle|\, \tilde{\Psi} \right\rangle = F[\tilde{\varrho}] + \int d\vec{r}\, \tilde{\varrho}(\vec{r})v(\vec{r}) = E_v[\tilde{\varrho}] \geq E_v[\varrho] \tag{1.60}$$

If $E_v[n]$ is differentiable, the third HK theorem can be written in the same fashion of the

method of Lagrange multipliers,

$$\delta\left[E_v[\varrho] - \mu\left(\int d\vec{r}\, \varrho(\vec{r}) - A\right)\right] = 0, \tag{1.61}$$

where μ is the chemical potential

$$\mu = \frac{\delta E_v[\varrho]}{\delta\varrho} = \frac{\delta F[\varrho]}{\delta\varrho} + v(\vec{r}). \tag{1.62}$$

$\square$

The attractive possibility of having an exact theory has led to attempts to determine the exact, or at least a properly approximate, structure of the universal functional $F[\varrho]$. In fact, once its explicit form were available, it would be possible to apply DFT to all nuclear systems. Unfortunately, this reveals to be a terribly difficult task. The reason is of course that all of the complications contained in the many-variable wave function of the system could not have disappeared at once by moving to the usage of the simpler density function as the basic variable of the many-body problem. Most of the attempts to provide an approximate form of the exact universal functionals rely on drastic assumptions, but it is still very remarkable that one has a well-defined procedure for finding the ground-state properties of a possibly huge amount of systems.

1.3.2   Levy-Lieb constrained-search formulation

The ground-state wave function of a system described by a Hamiltonian determines uniquely the ground-state density. The HK theorems define then a one-to-one mapping between the density function and the external potential $v(\vec{r})$, up to an arbitrary constant. If one were able to provide a form of the universal functional $F[\varrho]$, the correct ground-state density then would determine uniquely the ground-state energy.

A density is called v-representable if it is related to the antisymmetric ground-state wave function of an Hamiltonian of the type (1.52). It is important then to give a more precise formulation of the first HK theorem: There exists a one-to-one map between the ground-state wave function of a many-body quantum system and its v-representable density. Energy density functionals are at this point defined for v-representable densities, only. A major complication is associated to v-representable densities: there does not exist any condition for a trial density to be v-representable. In fact, many densities have been shown to be not v-representable [63].

Here it comes the relevance of a new formulation of DFT, in terms of densities that satisfy a weaker condition, namely the N-representability condition. A density is N-representable if it can be obtained from an anti-symmetric wave function. This condition is satisfied by any reasonable one-body local density and it is a necessary condition for v-representability. By reasonable density one means that a density is N-representable if it satisfies the Gilbert conditions, equations (1.57), (1.58), and

$$\int d\vec{r} \left| \nabla \sqrt{\varrho(\vec{r})} \right|^2 < \infty \, , \tag{1.63}$$

a smoothness requirement for the functional form of the density. For instance, wild oscillations of the density preclude N-representability. In other words, a N-representable density can be written in terms of N orthonormal orbitals, that generate $\varrho(\vec{r})$ from a Slater determinant wave function.

By definition, there exists an infinite number of anti-symmetric wave functions that reproduce the same correct ground-state density; thereby, one could ask how to distinguish the true ground-state wave function Ψ_0 from any Ψ_{ϱ_0} which also integrates to the correct ground-state density ϱ_0. In other words, the question is how to identify, among all the N-representable densities, the one v-representable density coming from the true ground-state wave function of the Hamiltonian. This critical theoretical issue of the HK formulation of DFT can be solved by extending the domain of the energy density functional $E_v[\varrho]$ from v-representable densities to the larger set of N-representable densities. The idea is to exploit the minimum energy principle, that uniquely identifies the true ground-state wave function,

$$\langle \Psi_{\varrho_0} \,|\, \mathcal{H} \,|\, \Psi_{\varrho_0} \rangle \geq \langle \Psi_0 \,|\, \mathcal{H} \,|\, \Psi_0 \rangle = E_0 \, . \tag{1.64}$$

This expression is given by the sum of the expectation value of the universal functional

$$F[\varrho_0] = \langle \Psi_{\varrho_0} \,|\, \mathcal{T} + \mathcal{W} \,|\, \Psi_{\varrho_0} \rangle = \min_{\Psi \to \varrho_0} \langle \Psi \,|\, \mathcal{T} + \mathcal{W} \,|\, \Psi \rangle \, , \tag{1.65}$$

defined for any v-representable density, and that of the external potential term, which is one-to-one coupled to the density. The Levy-Lieb (LL) formulation rewrites the minimum energy principle in order to make explicit the fact that the variational search is constrained: the trial space for the wave functions is restricted only to those that reproduce the requested v-representable

density ϱ_0 by quadrature. Using this clever reorganization, one extends the domain of the universal functional to N-representable densities:

$$F_{LL}[\varrho] = \min_{\Psi \to \varrho} \langle \Psi \,|\, \mathcal{T} + \mathcal{W} \,|\, \Psi \rangle \; , \tag{1.66}$$

with $F_{LL}[\varrho_0] = F_{HK}[\varrho_0]$.

A double-hierarchy minimization for the ground-state energy calculation stems out:

$$\begin{aligned}
E_0 &= \min_{\Psi} \langle \Psi \,|\, \mathcal{T} + \mathcal{W} \,|\, \Psi \rangle \\
&= \min_{\varrho} \left[\min_{\Psi \to \varrho} \langle \Psi \,|\, \mathcal{T} + \mathcal{W} \,|\, \Psi \rangle \right] \\
&= \min_{\varrho} \left[F_{LL}[\varrho] + \int d\vec{r} \, \varrho(\vec{r}) v(\vec{r}) \right].
\end{aligned} \tag{1.67}$$

The existence of the minimum has been proved by Lieb in [64]. The LL constrained-search formulation of DFT removes the original issues associated to v-representability. The optimization proceeds in two different steps; first one search the optimal wave function which reproduce a given density. The trial space of densities is explored, and at the end of the first minimization one has in its hands a set of local minima. The sense of the second minimization is simply to identify the global minimum among those.

1.3.3 Kohn-Sham scheme

The Kohn-Sham (KS) scheme gives an insight on the HK theorems and on the structure of the universal functional $F[\varrho]$. In [65] Kohn and Sham, by mathematical reorganizing the EDF, reformulated DFT, turning a theory highly difficult to be handled into a practical tool for precise calculations. A set of effective single-particle KS equations are introduced for an auxiliary KS system of N non-interacting particles, described by the Hamiltonian $\mathcal{H}_{KS} = \mathcal{T}_{KS} + \mathcal{V}_{KS}$. Exploiting the first HK theorem, one asserts that for any interacting system there exists a unique, local, single-particle potential $v_{KS}(\vec{r})$, such that the exact ground-state density of the interacting system equals that of the non-interacting KS reference system:

$$\varrho(\vec{r}) = \varrho_{KS}(\vec{r}) = \sum_{i=1}^{N} |\phi_i(\vec{r})|^2 \; . \tag{1.68}$$

The total ground-state wave function of this fictitious system is fully determinantal,

$$\Phi_{KS} = \frac{1}{N!} \det[\phi_1 \ldots \phi_N] \,, \tag{1.69}$$

and the single-particle wave functions ϕ_i, also unique functionals of the density, can be found as the lowest-energy eigenstates of the single-particle Hamiltonian,

$$\mathcal{H}_{KS}\phi_i(\vec{r}) = \epsilon_i\phi_i(\vec{r}) \,. \tag{1.70}$$

The energy functional of the original system, that reads

$$E[\varrho] = F[\varrho] + \int d^3r \; \varrho(\vec{r})v(\vec{r}) \tag{1.71}$$

$$= T[\varrho] + W[\varrho] + \int d^3r \; \varrho(\vec{r})v(\vec{r}) \,, \tag{1.72}$$

is equal to the energy density functional of the auxiliary KS system,

$$E_{KS}[\varrho] = T_{KS}[\varrho] + \int d^3r \; \varrho(\vec{r})v_{KS}(\vec{r}) \tag{1.73}$$

$$= -\frac{\hbar^2}{2m} \sum_i \langle \phi_i \,|\, \nabla_i^2 \,|\, \phi_i \rangle + \int d^3r \; \varrho(\vec{r})v_{KS}(\vec{r}) \,. \tag{1.74}$$

The KS EDF is minimized by the ground-state density associated to $\mathcal{H}_{KS}$. This scheme entails that the universal functional splits into

$$F[\varrho] = T_{KS}[\varrho] + U[\varrho] + E_{\text{xc}}[\varrho] \tag{1.75}$$

where the first term is the non-interacting kinetic energy, the second is the local Hartree term, while the exchange-correlation term is formally defined by the previous equations as

$$E_{\text{xc}}[\varrho] = T[\varrho] + W[\varrho] - U[\varrho] - T_{KS}[\varrho], \tag{1.76}$$

and it captures all dynamical quantum many-body effects. Thereby, one has a structure for the Kohn-Sham potential,

$$v_{KS}[\varrho] = v_{\text{H}}[\varrho] + v_{\text{xc}}[\varrho], \tag{1.77}$$

where the exchange-correlation potential reads

$$v_{xc}[\varrho] = \frac{\delta E_{xc}}{\delta \varrho} \tag{1.78}$$

The Kohn-Sham formulation of Density Functional Theory has the advantage of being fully local. Its accuracy depends only on the approximation of the unknown exchange-correlation energy, which is nevertheless universal. The first level of approximation, consisting in fully neglecting E_{xc}, delivers the Hartree equations. Still, the scheme goes far beyond the Hartree mean-field approximation, even only because it takes into account all the correlation effects, and it is, at least in principle, exact. Another possible approximation scheme is the local density approximation (LDA), in which the exchange-correlation term is taken equal to that of an infinite uniform system:

$$E_{xc} = \int d\vec{r}\, \varrho(\vec{r})\epsilon_{xc}[n] \tag{1.79}$$

Among the state-of-the-art beyond-LDA approximation schemes, the most relevant is the generalized-gradient-approximation (GGA). See [66] for more details.

1.4   Inverse Problems

The definition of inverse problem comes in opposition to that of direct, or forward, problem. A direct problem deals with the calculation of a quantity, for instance the density of some system or its evolution in time, as a function of its causes, say the interaction between the constituent particles of the system or the equation of motion. Direct problems can usually be expressed through a system of differential equations that fully determine their evolution. On the other hand, inverse problems typically arise whenever one tries to perform the indirect observation of some quantity of interest. Here, the knowledge of some observable is given and one aims to derive the causes that have resulted in that. It is a matter of fact that inverse problems often present features of non-locality and non-causality. Those features contributes generating instabilities of the solution of the problem [67]. Consider the inverse heat equation problem, namely the attempt of estimating an initial temperature distribution, based on the measurement of the temperature distribution at some final time. An infinity of different initial conditions may have ended up into the same final state; small changes in the initial temperature could have smeared out in time. On the contrary, however complex the system might be, the corresponding forward problem is local and casual: it is guided by the heat equation. Another

example is given by the calculation of the gravitational field of the Earth, given the knowledge of its density (direct problem) versus the estimate of the density the Earth given the knowledge of the generated gravitational field (inverse problem). In the case of the inverse problem, one must incorporate all available information about the initial data that one may had prior to the measurement.

1.4.1 Ill-posed problems

The mathematical definition of well-posed problems was first stated in [68]. Any mathematical model apt to describe a physical system should respect the three Hadamard criteria:

HC1 The existence of a solution of the problem.

HC2 The uniqueness of the solution of the problem.

HC3 The continuous and smooth dependence of the solution of the problem as function of its initial conditions.

A problem is well-posed when the above three conditions are fulfilled, while it is said to be an ill-posed problem if any of those is defective.

Forward problems are, in most of the cases, well-posed. Because of that there is a good chance of being able to implement stable algorithms to produce solutions. On the other hand, inverse problems are often ill-posed. The existence of an analytic solution is not guaranteed. It is then necessary to implement numerical methods to obtain results. When an inverse problem is formulated within a continuous space which gets discretized for computational purposes, discretization errors may appear. Finite precision easily leads to numerical instabilities and to unexpected, possibly non-physical, behaviors. Among those, numerical methods, because of their intrinsic rounding and approximations, might make inverse problems less ill-posed than they actually are, and produce solutions that contain more information than that actually carried by the input. To ignore the discretization errors results in overly optimistic expectations about the performance of the inversion method [69]. In those cases, one says that the model is over-fitting to the input data. A wrong model is reproducing the data too well in comparison to the factual knowledge given by the input data. This type of behaviors of inversion methods go under the name of inverse crimes.

1.4.2   Inverse Kohn-Sham problem

The inverse Kohn-Sham (IKS) problem consists in deducing the form of the KS potential, Equation (1.77), given the knowledge of the density of a nuclear system. The solution of the inverse problem in DFT may reveal useful to benchmark the approximate EDFs available on the market. In this sense, it can represent an independent strategy to fine-tune theoretical models employed to describe nuclear structure.

The direct problem in the KS scheme of DFT, namely the potential-to-density problem, is widely considered to be well-posed, above all thanks to the HK theorems and to the LL constrained-search formulation already discussed above. On the other hand, although the IKS problem can also be well-posed for some specific discretized systems [70], in most of the cases errors and lack of detailed information about the input density make the problem ill-posed. The nuclear density determines a set of single-particle wave functions, up to an overall phase factor; also, unitary transformations of the KS orbitals wind up in generating the same density. The orbitals in turn identify the form of the KS potential, up to an arbitrary constant, via the KS equations. Special attention must be paid then in developing an inversion method that converges to the true solution of the inverse problem, because non-uniqueness features are a matter of fact.

In general, both the direct and inverse KS problems share the same set of equations: the Kohn-Sham equations. Yet, there are some differences that imply developing completely independent algorithms to solve them. For a closed-shell, spin-saturated system of neutrons and protons, the KS equations read:

$$\left[-\frac{\hbar^2}{2m}\nabla^2 + v_{KS}(n(\vec{r})) \right] \phi_i(\vec{r}) = \epsilon_i \phi_i(\vec{r}) \tag{1.80}$$

$$n(\vec{r}) = 2\sum_{i=1}^{N_{\text{orb}}} |\phi_i(\vec{r})|^2 \tag{1.81}$$

$$v_{KS}[n] = v_{\text{H}}[n] + v_{\text{xc}}[n] \, , \tag{1.82}$$

where the orbitals are considered to be orthonormal and the external potential is absent in the nuclear case. In the case of the direct problem, the unknowns are the set of the wave functions and the density, while for the inverse problem the unknowns are the Kohn-Sham potential and the wave functions. In the forward problem one must deal with a non-linear eigenvalue problem, since assumptions for v_{KS} may contain powers of ϱ, $\nabla\varrho$, and so on; instead, in the inverse problem the eigenvalue problem is fully linear, and non-linearity features are encoded in the

definition of the density. It is such subtle difference that entails the necessity of using different methods for the solutions of the two problems. Moreover, the inverse problem is highly constrained, while the forward problem is free. In fact, in the former case the knowledge of the density defines several constraints to be respected by the Kohn- Sham orbitals. Those formal constraints will be made explicit in the next chapter, in the definition of the Constrained Variation inversion algorithm, section 2.1.2.

Chapter 2

SOLUTION AND APPLICATIONS OF THE INVERSE KOHN-SHAM PROBLEM

A general nuclear energy density functional should be a functional of isoscalar, isovector and spin densities, as well as corresponding currents. The systematic construction of all possible densities and their gradients has been described in [71], while a classification of all possible terms that should compose a NEDF has been treated in [72]. These terms are all the scalar quantities that can be built out of densities and that are invariant under parity, time-reversal, rotational, translational and isospin transformations. The number of such terms easily becomes very large, making the EDF fitting procedure rather prohibitive. During the last decade, many groups took up the quest of building more general energy density functionals, in which one starts from density-dependent terms, and progressively incorporates other terms that depend on density gradients [73, 74]. Others have tried to derive the nuclear EDFs from fundamental approaches [75].

Current efforts to build a nuclear EDF are hindered by the lack of a clear strategy for systematic improvement. The solution of the inverse Kohn-Sham problem, scarcely discussed in nuclear physics literature, may be a road worth trying to undertake. As already discussed in section 1.3.3 of this manuscript, the Kohn-Sham scheme for the formulation of Density Functional Theory represents one of the most successful theoretical approaches to the study of both electronic and nuclear structure. The possibility of obtaining an exact solution of a well-established theory in physics always represents a source of knowledge that one should investigate. This is

especially true in nuclear physics, where most theoretical models are highly dependent on the phenomenology and heavily lean on experimental data. The construction of exact Kohn-Sham potentials from nuclear empirical densities is promising and pioneering, since it may provide a reliable benchmark against which approximate energy density functional can be tested. In the present chapter, the practical methods for the solution of this inverse problem, presented in section 1.4.2, is addressed. To this end, different algorithms have been proposed across the last thirty years, in atomic and condensed-matter physics, as well as in quantum chemistry. They all emerge from alternative formulations of the inverse problem; some of them are based on the optimization of a functional, whereas others are iterative.

The solution of the inverse problem can be addressed both to finite and extended systems, once appropriate boundary conditions are applied. The main issue is however that one generally lacks the exact boundary conditions that must be applied *a priori* to the potential. Only some phenomenological knowledge of the expected asymptotic behaviors is available. Given that the density structure fixes the sum of the squared orbitals at boundaries, if any boundary condition were imposed, it should be in total agreement with the density constraints. An alternative idea is to let the inversion method define the boundaries of the orbitals to agree with the density constraints. That is the so-called no-boundaries density-constrained strategy. This strategy is applied, *e.g.*, in the van Leeuwen and Baerends (vLB) method discussed in section 2.1.1. Although no detailed knowledge of the boundaries is needed, it is quite common to stumble upon inverse crimes. In that case, the boundary values of the potential may have to be discarded *a posteriori*, to respect of the actual piece of information carried by the input density.

In the forward, well-posed, Kohn-Sham problem, the KS equations can be solved relatively easily by, for instance, a self-consistent routine. The errors in the resulting density then mainly depend on the specific algorithm's numerical discretization, on the choice of the convergence conditions, and on the quality of the input potential. In the corresponding inverse problem, of course the discretization choice fairly impacts on the precision of the results, but the quality of the input density represents a very fundamental limit on the possibility of successfully performing the inversion. In fact, if the numerical error of a given density is not properly taken into account, the inversion can produce over-fitting issues or lead to non-physical features of the output potential. In the framework of the direct problem, the assumed potential is known everywhere at the same level of detail; in contrast, the density of many systems is known in some radial intervals and extrapolated elsewhere according to more or less sound assumptions.

In the practical applications presented in this manuscript, results are mainly positive when one tests the algorithm with analytic formulas of the target density, for which one already knows the expected potential. On the other hand, when one deals with empirical densities and treats more-than-one-dimensional systems, much higher attention must be paid.

The non-relativistic framework for the solution of the inverse Kohn-Sham problem disregards the contribution of the spin-orbit potential, a term which is normally added *ad hoc*, not being encoded into the empirical nuclear density distributions from which the Kohn-Sham potentials are derived. The relevance of the spin-orbit term for solid predictions of nuclear structure properties has already been discussed in section 1.1.3 and 1.2.3. Since the spin-orbit potential is a completely phenomenological addition to the non-relativistic KS potential, it cannot be determined from the ground-state density using the IKS method. Therefore, it is natural to extend the methods for the inverse Kohn-Sham problem to relativistic nuclear EDFs, where the spin-orbit potential, is automatically incorporated in the formalism.

In this chapter, two inversion algorithm are presented and applied to the solution of the IKS problem for doubly-magic nuclei. Afterwads, the formalism of the density-to-potential inversion is generalized to the relativistic framework. In the particular case of relativistic EDFs considered here, the functional depends also on the Lorentz scalar single-nucleon density, which is not an observable. Finally, the information on the KS potential obtained in this new and pioneering way from empirical densities is employed to improve a given functional towards the exact, unknown, EDF, starting from a relatively simple functional form, in the framework of the Density Functional Perturbation Theory [76]. The idea is to consider as a first-order perturbation the difference, supposedly small, between the known functional and the exact EDF.

2.1 Algorithms For The Solution Of The Inverse Kohn-Sham Problem

This section presents two algorithms for the density-to-potential inversion in the non-relativistic framework. Both methods are discussed in great detail in [77]. A necessary assumption is that the effective KS potential that compose the EDF is only position-dependent. That is, non-local effects and the spin-orbit potential are not taken into account. The possibility of including the latter is addressed below, section 2.3.

The first inversion method, based on the van Leeuwen and Baerends (vLB) algorithm, consists of an iterative procedure, whereas the second, the Constrained Variational (CV) method,

in a constrained minimization of the kinetic energy of the auxiliary Kohn-Sham system.

2.1.1   Van Leeuwen and Baerends method

The method consists in iteratively adjusting the calculated density of the system to mimic the input target density. To this purpose, starting from an initial guess for the effective Kohn-Sham potential $U[\varrho]$, the algorithm updates the former at each step until convergence is reached. Consider the KS equation in spherical symmetry,

$$\left(-\frac{\hbar^2}{2m}\frac{d^2}{dr^2} + \frac{\hbar^2 l(l+1)}{2mr^2} + U(r)\right)u_i(r) = \epsilon_i u_i(r) \ , \tag{2.1}$$

where $u_i(r)$ are the reduced radial wave functions and $U(r) = U[\varrho(r)]$ is the effective Kohn-Sham potential; in the case of spherical nuclei $i = \{n, l, j\}$, respectively, the principal quantum number, the orbital and the total angular momentum. The full single-nucleon wave function reads

$$\psi_i(\vec{r}) = \frac{u_{nlj}(r)}{r}[Y_l(\theta, \phi) \otimes \chi_{1/2}]_{jm} \ , \tag{2.2}$$

where m is the projection of the total angular momentum j on the z-axis. The boundary conditions associated to the Kohn-Sham Equation (2.2) are

$$\lim_{r\to 0} u(r) = r^{l+1} \tag{2.3}$$

$$\lim_{r\to 0} u'(r) = (l+1)r^l \ , \tag{2.4}$$

and they are enough to solve the equation directly, which means to calculate the density starting from a given Kohn-Sham potential, by means of, *e.g.*, a shooting algorithm. The solution of the eigenvalue problem gives access to the nuclear density, which, in spherical symmetry, reads

$$\varrho(r) = \frac{1}{4\pi r^2}\sum_{i=0}^{N_{\mathrm{orb}}}(2j+1)u_i^2(r) \ . \tag{2.5}$$

The factor $(2j+1)$ accounts for the fact that only closed-shell nuclei are here considered. In absence of a spin-orbit potential, working with the uncoupled l and s or with the coupled total angular momentum $j = l + s$ is fully equivalent.

An algebraic manipulation of Equation (2.2) is performed to isolate the KS potential,

$$U(r) = \frac{1}{4\pi r^2 \varrho(r)} \sum_{i=0}^{N_{\text{orb}}} \left[(2j+1)u_i(r) \left(\frac{\hbar^2}{2m} \frac{d^2}{dr^2} - U_l \right) u_i(r) + \epsilon_i (2j+1)u_i(r) \right], \qquad (2.6)$$

where U_l is a shorthand for the centrifugal potential. Out of Equation (2.6) an inverse routine can be devised by substituting the density in the denominator with the input target density $\tilde{\varrho}$. Comparing with Equation (2.2), and given the definition of the density (2.5), one obtains:

$$U^{(k+1)}(r) = \frac{\varrho^{(k)}(r)}{\tilde{\varrho}(r)} U^{(k)}(r) . \qquad (2.7)$$

The latter equation has an intuitive significance: if at any coordinate the iterated density becomes larger (smaller) than the target density, the absolute value of the KS potential is increased (decreased) in the successive iteration. While such behavior works fine in the case of repulsive potentials, in the case of attractive potentials the opposite should happen. Moreover, the routine does not allow the potential to change sign in the iterative process, leading to possible problems in proximity of $U(r) = 0$. Equivalently, it forces to careful choose the arbitrary energy shift of the potential. As suggested in [77], both problems can be solved at once by adopting the following reformulation of the iterative rule (2.7):

$$U^{(k+1)}(r) = U^{(k)}(r) + \gamma \frac{\varrho^{(k)}(r) - \tilde{\varrho}(r)}{\tilde{\varrho}(r)} ; \qquad (2.8)$$

in practical applications the prefactor can be safely set to $\gamma = 1$ MeV.

To sum up, the flow chart for the implementation of the vLB method reads

1. An initial guess of the average potential must be assumed. Usually, a Woods-Saxon potential[1] is appropriate;

2. Equation 2.2 must be solved in order to get the KS energy levels ϵ_i and the eigenfunctions $u_i(r)$;

3. The k-th nuclear density is calculated according to Equation 2.5;

4. The potential is adjourned by means of Equation 2.7 or Equation 2.8;

---

[1]The Woods-Saxon potential is defined $V_{WS} = V_0 \frac{[1 \pm \kappa(N-Z)/(N+Z)]}{1+\exp[(r-R_0)/a]}$; a is the diffuseness of the nuclear surface, the plus (minus) sign holds for protons (neutrons), $\kappa = 0.86$ and $V_0 = -51$ MeV

5. The procedure is repeated until the absolute variation of the potential is everywhere smaller than a user-chosen quantity α:

$$\Delta U^{(k)} = \max_r \left| U^{(k+1)}(r) - U^{(k)}(r) \right| \leq \alpha. \tag{2.9}$$

The method is remarkably robust, leading to convergence despite of the choice of the starting guess of the potential. The main drawback consists in the algorithm's inability to adjust the tail of the potential, where the nuclear densities are infinitesimally small. In any case, the empirical densities are absolutely unreliable for what regards their tails, as discussed in section 2.2.1 below.

2.1.2   Constrained Variation method

If one looks at the KS scheme as an energy optimization problem, the Constrained Variation (CV) method can be devised as a recipe for a routine able to solve the inverse Kohn-Sham problem avoiding the solution of an eigenvalue problem. Note that within many density-to-potential inversion algorithms, the diagonalization of the Hamiltonian becomes the main computational limit as soon as the size of the system increases. Through the CV method, one obtains a set of optimal wave functions that do reproduce the right target density, and yet are a unitary transformation away from the system's eigenfunctions. The method does not begin with any direct information on the potential structure, but rather with a guess on the functional structure of the Kohn-Sham orbitals. The main advantage is to deal with quantities that are formally closer to the known input, that is a nuclear density.

The method of the Lagrange multipliers is used to perform the minimization of the expectation value of the total kinetic energy of the auxiliary non-interacting system,

$$\langle \Phi \,|\, T_{KS} \,|\, \Phi \rangle = \frac{\hbar^2}{2m} \int d^3r \, \sum_{j=1}^{N} |\nabla \varphi_j(\vec{r})|^2 \,, \tag{2.10}$$

with respect to the Kohn-Sham orbitals $\varphi_j(\vec{r})$. Two types of constraints $c_i = 0$ are imposed:

$$c_0(\vec{r}) = \sum_{j=1}^{N} |\varphi_j(\vec{r})|^2 - \tilde{\varrho}(\vec{r}) = 0 \,, \tag{2.11}$$

$$c_{jk} = \langle \varphi_j \,|\, \varphi_k \rangle - \delta_{jk} = \int d^3r' \, \varphi_j^*(\vec{r}')\varphi_k(\vec{r}') - \delta_{jk} = 0 \,, \tag{2.12}$$

$j = 1, \ldots, N$ and $k = j, \ldots, N$ being a set of good quantum numbers. Specifically, the orbitals must integrate up to the correct target density, and they must obey orthonormality, in order to produce a N-representable density (section 1.3.2). The Hohenberg-Kohn theorems, section 1.3.1, ensure that the ground-state properties of the non-interacting auxiliary system, subject to the effective Kohn-Sham potential, will be the same as those of the real interacting system.

The Lagrangian of the system must be built; since time derivatives in the Schrödinger equation appear only linearly, in general one should consider complex fields or wave functions [78]. These are obtained as the superposition of two independent real fields,

$$\psi = \frac{\psi_1 + i\psi_2}{\sqrt{2}} , \tag{2.13}$$

$$\psi^\dagger = \frac{\psi_1 - i\psi_2}{\sqrt{2}} . \tag{2.14}$$

The Lagrangian density of a Schrödinger field reads

$$\mathcal{L} = i\psi^\dagger \dot{\psi} - \frac{\hbar^2}{2m} \nabla \psi^\dagger \cdot \nabla \psi - \psi^\dagger V(\vec{r}, t)\psi , \tag{2.15}$$

whence the Euler-Lagrange equations

$$\frac{\delta\mathcal{L}}{\delta\psi} - \nabla \cdot \frac{\delta\mathcal{L}}{\delta\nabla\psi} = \left(\frac{\delta\mathcal{L}}{\delta\psi} - \nabla \cdot \frac{\delta\mathcal{L}}{\delta\nabla\psi} \right)^\dagger = 0 , \tag{2.16}$$

return the Schrödinger equation and its complex conjugate

$$-\frac{\hbar^2}{2m} \nabla^2 \psi^\dagger + V\psi^\dagger = -i\dot{\psi}^\dagger , \tag{2.17}$$

$$-\frac{\hbar^2}{2m} \nabla^2 \psi + V\psi = i\dot{\psi} . \tag{2.18}$$

The conjugate variables to the fields are

$$\pi = \frac{\delta\mathcal{L}}{\delta\dot{\psi}} = i\psi^\dagger,$$

$$\pi^T = \frac{\delta\mathcal{L}}{\delta\dot{\psi}^\dagger} = 0 , \tag{2.19}$$

43

so that the Hamiltonian density reads

$$H = \pi\dot{\psi} + \pi^T\dot{\psi}^\dagger - \mathcal{L} = -i\frac{\hbar^2}{2m}\nabla\pi \cdot \nabla\psi - i\pi V\psi \ . \tag{2.20}$$

The Hamiltonian of the Schrödinger field is then just an integration away,

$$\mathcal{H} = \int_\Omega d\vec{r}\, H = \int_\Omega d\vec{r}\, \psi^\dagger\Big[-\frac{\hbar^2}{2m}\nabla^2 + V\Big]\psi \ . \tag{2.21}$$

If the fields ψ are time-independent, $\dot{\psi} = 0$, the right-hand sides of the Schrödinger equations (2.17) and (2.18) vanish, and the adjoint equation becomes trivial. Therefore, in the present case, one can consider real wave functions to define the non-interacting kinetic energy and the constraints, without any loss of generality.

The auxiliary Lagrangian,

$$\mathcal{L} = \frac{\hbar^2}{2m}\sum_{j=1}^{N}|\nabla\varphi_j(\vec{r})|^2 + U(\vec{r})\Big(\sum_{j=1}^{N}|\varphi_j(\vec{r})|^2 - \tilde{\varrho}(\vec{r})\Big) +$$
$$+ \sum_{j=1}^{N}\sum_{k=j}^{N}\epsilon_{jk}\Big(\int d^3r'\, \varphi_j(\vec{r}')\varphi_k(\vec{r}') - \delta_{jk}\Big) \ , \tag{2.22}$$

is build accordingly to the prescriptions of the method of the Lagrange multipliers: the constrained minimization is transformed into a free one with respect to the set of the orbitals and to the Lagrange multipliers. Since Lagrange multipliers in the KS auxiliary system are formally defined as

$$\lambda_i = \frac{\delta}{\delta c_i}\langle\Phi\,|\,T_{KS}\,|\,\Phi\rangle \ , \tag{2.23}$$

the zeroth multiplier, λ_0, which is associated to condition (2.11), is by definition the Kohn-Sham potential

$$U(\vec{r}) = \frac{\delta}{\delta\varrho}\langle\Phi\,|\,T_{KS}\,|\,\Phi\rangle \ , \tag{2.24}$$

that connects the auxiliary non-interacting system to the real interacting system, and enforces the density to be the same in both of them. In contrast, the multipliers of the constraints (2.12) have no plain physical meaning: they compose a symmetric matrix, whose elements are related to the opposite of those of a unitary transformation of the matrix containing the energies of the Kohn-Sham orbitals.

A this point, a cost functional $\mathcal{J}$ is defined as the space integral of the auxiliary Lagrangian (2.22),

and one may proceed to perform its minimization. This final step recalls the optimization of the action functional in mechanical system, equivalent to the solution of the Euler-Lagrange equation. The main advantage is that one can deal with the optimization of a functional rather than that of a multidimensional function. The cost functional reads

$$\mathcal{J}\left[\{\varphi_j\}_{j=1}^N, U(\vec{r}), \{\epsilon_{jk}\}\right] = \frac{\hbar^2}{2m} \int d^3r \sum_{j=1}^N |\nabla \varphi_j(\vec{r})|^2 +$$

$$+ \int d^3r\, U(\vec{r}) \Big(\sum_{j=1}^N |\varphi_j(\vec{r})|^2 - \tilde{\varrho}(\vec{r})\Big) +$$

$$+ \int d^3r \sum_{j=1}^N \sum_{k=j}^N \epsilon_{jk} \Big(\int d^3r'\, \varphi_j(\vec{r}')\varphi_k(\vec{r}') - \delta_{jk}\Big). \tag{2.25}$$

In spherical symmetry, the same has the following form:

$$\mathcal{J}_{\text{sph}}\left[\{u_j\}_{j=1}^N, v_K S(r), \{\epsilon_{ij}\}\right] = T_{\text{sph}}\left[\{u_j\}\right] + 4\pi \int_0^\infty dr\, U(r)\varrho(r)r^2$$

$$- \sum_{i=1}^N \sum_{j=1}^i \epsilon_{ij}\delta_{l_i l_j}\delta_{j_i j_j} \int_0^\infty dr\, u_i(r)u_j(r) \tag{2.26}$$

where T_{sph} is a shorthand notation for the spherical form of the kinetic energy. The derivation of Equation (2.26) from Equation (2.25) is exposed in great detail in [79]. The minimum of the kinetic energy plus the constraints coincides with the minimum of the functional, and the minimum energy principle ensures the existence of a global minimum of the functional $\mathcal{J}$. A necessary condition for the presence of an extremum of a functional is that the Lagrangian satisfies the Euler-Lagrange equations (2.16). The derivation of the kinetic term is straightforward,

$$\Big(\frac{\delta}{\delta\varphi_\alpha} - \nabla \cdot \frac{\delta}{\delta\nabla\varphi_\alpha}\Big)\frac{\hbar^2}{2m}\sum_{j=1}^N \Big[(\nabla\varphi_j(\vec{r}))^2\Big] = -\frac{\hbar^2}{m}\nabla^2\varphi_\alpha(\vec{r}), \tag{2.27}$$

while the derivation of the other two terms is slightly more cumbersome,

$$\left(\frac{\delta}{\delta\varphi_\alpha} - \nabla \cdot \frac{\delta}{\delta\nabla\varphi_\alpha}\right)\left\{U(\vec{r})\Big[\sum_{j=1}^{N}\Big(\varphi_j(\vec{r})\varphi_j(\vec{r})\Big) - \tilde{\varrho}(\vec{r})\Big]+\right.$$

$$\left. + \sum_{j=1}^{N}\sum_{k=j}^{N}\epsilon_{jk}\Big(\int d^3r'\,\varphi_j(\vec{r'})\varphi_k(\vec{r'}) - \delta_{jk}\Big)\right\}$$

$$= 2U(\vec{r})\varphi_\alpha(\vec{r}) + \Big[\sum_{j=1}^{\alpha}\varphi_j(\vec{r})\epsilon_{j\alpha} + \sum_{k=\alpha}^{N}\epsilon_{\alpha k}\varphi_k(\vec{r})\Big]. \tag{2.28}$$

In the derivation of the second term one has to deal with the fact that only the upper triangular part of the symmetric matrix ϵ_{jk} is defined. Thus, the sum in this second term proceeds in the following way,

$$\begin{bmatrix} \epsilon_{11} & & \epsilon_{1\alpha} & & \\ & \ddots & \downarrow & & \\ & & \epsilon_{\alpha\alpha}^{\text{twice}} & \rightarrow & \epsilon_{\alpha N} \\ & & & \ddots & \\ & & & & \epsilon_{NN} \end{bmatrix} \tag{2.29}$$

with a double-counting of the diagonal elements. Equations (2.27) and (2.28) sum up to zero; the minimum of the cost functional (2.25) is then identified by the following set of Euler-Lagrange equations, obtained by artificially introducing $\varphi_\beta(\vec{r})$ and integrating,

$$\frac{\hbar^2}{m}\int d^3r\,\varphi_\beta(\vec{r})\nabla^2\varphi_\alpha(\vec{r}) = 2\int d^3r\,\Big[\varphi_\beta(\vec{r})U(\vec{r})\varphi_\alpha(\vec{r})\Big]+$$

$$+ \int d^3r\,\varphi_\beta(\vec{r})\Big[\sum_{j=1}^{\alpha}\varphi_j(\vec{r})\epsilon_{j\alpha} + \sum_{k=\alpha}^{N}\epsilon_{\alpha k}\varphi_k(\vec{r})\Big], \tag{2.30}$$

where $\alpha = 1, \ldots, N$ and $,\beta \geq \alpha$. At the end of the minimization process, once the KS orbitals have been calculated, a manipulation of Equation (2.30) allows to isolate and calculate the KS potential, as well as the multipliers ϵ_{jk},.

In the practical implementation one works with a discrete mesh for the coordinate space, which is divided into n_r equally distant points. The minimization process deals with Nn_r and $\frac{N(N+1)}{2} + n_r$ unknowns for the orbitals and for the Lagrange multipliers, respectively. Together

with the $N^2 n_r$ linear equations (2.30), the n_r constraints

$$c_0(\vec{r}) = \sum_{j=1}^{N} |\varphi_j(\vec{r})|^2 - \tilde{\varrho}(\vec{r}) = 0 \; , \tag{2.31}$$

and the $\frac{N(N+1)}{2}$ equations provided by

$$\int d^3 r' \; \varphi_j(\vec{r}')\varphi_k(\vec{r}') - \delta_{jk} = 0 \; , \tag{2.32}$$

it is possible to solve the problem, at least in principle.

In order to avoid rounding errors in the regions where the kinetic energy is small due to the exponential decay of the wave functions, the latter are rescaled accordingly to

$$\varphi_j(\vec{r}) = \sqrt{\tilde{\varrho}(\vec{r})} f_j(\vec{r}) \; , \tag{2.33}$$

to make the terms in the sum of the kinetic energy (2.10) all of the same, unitary, order of magnitude.

Two conditions determine the convergence of the algorithm:

1. The relative tolerance on the violation of the constraints; at each step of the optimization, there is a test of the condition

$$\max_i |\frac{g_i - c_i}{g_i}| < \epsilon \; , \tag{2.34}$$

   where the quantities subject to the constraints are g_i, and the requested constraint is c_i.

2. The tolerance on the value of the scaled orbitals f_i defined in Equation (2.33); the algorithm stops if the change in value of the scaled orbitals between two successive iterations is smaller than a given tolerance δ, namely, if

$$\max_i |f_i^{(k)} - f_i^{(k-1)}| < \delta \; , \tag{2.35}$$

   where k is the iteration number.

In the present work, the optimization of the cost functional, Equation (2.25), as been carried out by employing the IPOPT library [80], whereas for the solution of the Euler-Lagrange equations

the EIGEN library[2] has been used.

As one can see in Figure 2.5, it is clear that the convergence criteria for the CV and vLB methods are completely different. While the orthonormal condition is exactly fulfilled by the vLB method by construction, the CV method allows for some overlap of the wave functions, controlled by the quantity ϵ in Equation (2.34). On the other side, the CV method checks for the self-consistency of the orbitals, while the convergence criteria of the vLB method, Equation (2.9), is based only on the change of the KS potential.

2.2 Tests Of The Inversion Algorithms

2.2.1 Empirical nuclear densities

The KS potential is calculated for the experimental proton densities of ^{40}Ca and ^{208}Pb, and for the neutron density of ^{208}Pb. The first two are obtained from electron scattering data [1], whereas the latter by means of proton scattering measurements [2]. Following the prescriptions given in [81], the experimental electromagnetic charge and neutron densities are parameterized with a sum of Gaussian function, Equation (2.36) below. The main purpose of this parameterization is to describe the scattering data on top of a basis of well-behaved functions, without using model distributions. On the other hand, this model leads to a non-physical functional behavior of the tail of the densities, as discussed and shown by the results obtained at the end of the present section.

The Sum of Gaussian (SoG) parameterization used for the empirical densities reads

$$\varrho_{\text{charge}}(r) \ = \ \sum_i A_i^{(\text{charge})} \left(e^{-\left(\frac{r - R_i}{\gamma}\right)^2} + e^{-\left(\frac{r + R_i}{\gamma}\right)^2} \right) , \tag{2.36}$$

and the coefficients $A_i^{(\text{charge})}$ are given by

$$A_i^{(\text{charge})} \ = \ \frac{Z e Q_i}{2\pi^{\frac{3}{2}} \gamma^3 \left(1 + \frac{2R_i^2}{\gamma^2} \right)} , \tag{2.37}$$

where Q_i is the fraction of total charge that is associated with the integral of the ith Gaussian. Accordingly, the normalization condition $\sum_i Q_i = 1$ must hold. The two Gaussians are centered at different points R_i, whereas their widths are characterized by a common value γ. The value of γ is tuned to be close to the width of the narrowest peak that one finds when inspecting

---

[2]https://eigen.tuxfamily.org/

the square of typical Hartree-Fock or Woods-Saxon wave functions for the nucleus under study. If the sum contains enough terms, the SoG parameterization, Equation (2.36), corresponds to a model-independent representation of the data points. In principle, that would require a very large number of Gaussian terms if the experimental data covers the full momentum transfer range. Experimentally this is not possible, and about ten terms proved to be robust against small changes. The representation may indeed break down whenever experimental data is too scarce or if it does not cover a wide enough range of projectile energies and scattering angles.

In order to calculate the proton densities from the charge densities, the effects of the spin-orbit and the neutron electromagnetic finite size [82] has been neglected; the proton densities are extracted according to

$$\varrho_{\text{charge}}(\vec{r}) = \int d^3r' \ f(\vec{r'}) \varrho_p(\vec{r} - \vec{r'}) \ . \tag{2.38}$$

Using the approximate electric proton form factor,

$$f(\vec{r}) = \frac{e}{\pi^{3/2}} e^{-\left(\frac{r^2}{\alpha}\right)^2} , \tag{2.39}$$

where $\alpha = \sqrt{2/3} R_p$, and the r.m.s. proton radius is $R_p = 0.87$ fm. The deconvolution that leads to the proton density is performed in the Fourier space. Due to the properties of the Gaussian functions, the result in coordinate space can be written analytically assuming spherical symmetry,

$$\varrho_p(r) = \sum_i \frac{\gamma^3 A_i}{e \beta r} \left[\left(\frac{r - R_i}{\beta^2} + \frac{R_i}{\gamma^2} \right) e^{-\left(\frac{r - R_i}{\beta}\right)^2} + \left(\frac{r + R_i}{\beta^2} - \frac{R_i}{\gamma^2} \right) e^{-\left(\frac{r + R_i}{\beta}\right)^2} \right], \tag{2.40}$$

where $\beta = \sqrt{\gamma^2 - \alpha^2}$.

In the case of neutron densities, the previous procedure is not needed. Reference [2] provides the neutron density in the form of Equation (2.36) directly. In fact, protons interact via the strong interaction with both neutrons and protons. So, if the proton density is known, one can derive a neutron density compatible with the experimental cross section. At variance with the case of the determination of the electromagnetic charge density, this procedure is not fully model-independent. In fact, even if the proton-nucleus interaction at intermediate incident energy is well-known, it still has some uncertainty.

The two algorithms have been applied to the nuclear empirical densities. Good agreement

between those and the densities calculated solving the KS equations with the obtained KS potential has been found in all cases. This is clearly visible in the left panels of Figure 2.1 for ^{40}Ca, and Figure 2.2 for ^{208}Pb. The relative differences found for the densities are of the same order of those found for theoretical densities in the following section, although in the case of the vLB procedure for ^{40}Ca the error can reach 0.025% in the outermost region of the nucleus (table 2.1). Since the differences between the vLB and CV densities and the target densities are not visible in detail from the figures, the maximum and the average of the absolute value of the differences are reported in Table 2.1. The Kohn-Sham potentials, shifted by using the experimental neutron and proton separation energies, and obtained with the vLB and CV methods, are shown in the right panel of Figure 2.1 for ^{40}Ca, and Figure 2.2 for ^{208}Pb.

The agreement between the two inversion methods is again remarkable, see the right panels of figures 2.1 and 2.2. However, while the potentials in the inner part of the nuclei look physically reasonable, they oscillate and then diverge in the asymptotic region. Of course, the asymptotic behavior of the KS potentials at large distances is not the expected Fermi-like one, namely

$$U_{\mathrm{n}}(r \to \infty) \to 0 \tag{2.41}$$

for neutrons, and

$$U_{\mathrm{p}} + U_{\mathrm{Coul.}}(r \to \infty) \to U_{\mathrm{Coul.}} = \frac{(Z-1)e^2}{r} \tag{2.42}$$

for protons. The cause of this behavior is to be found in the Gaussian tail of the parameterization of the empirical densities, which the algorithms somehow correctly turn into a quadratic, harmonic oscillator-like, potential. To support this explanation, the regions corresponding to r larger than the radius of the outermost (second outermost) Gaussian in the case of the ^{208}Pb (^{40}Ca) density are shown as shadowed areas in figures 2.1 and 2.2, respectively. The borders of these regions are evidently correlated to the change in slope of the potentials. As a consequence, the results for the KS potentials derived from experimental densities are not reliable in the tail of the potential. The employed procedures remain robust when experimental SoG densities are used, and provide reliable information about the potential up to the average position of the nuclear surface.

2.2.2 Theoretical nuclear densities

The two algorithms have been tested furthermore on the theoretical densities of the doubly-magic nuclei ^{40}Ca and ^{208}Pb, shown in Figure 2.4. This helps corroborating the explanation for
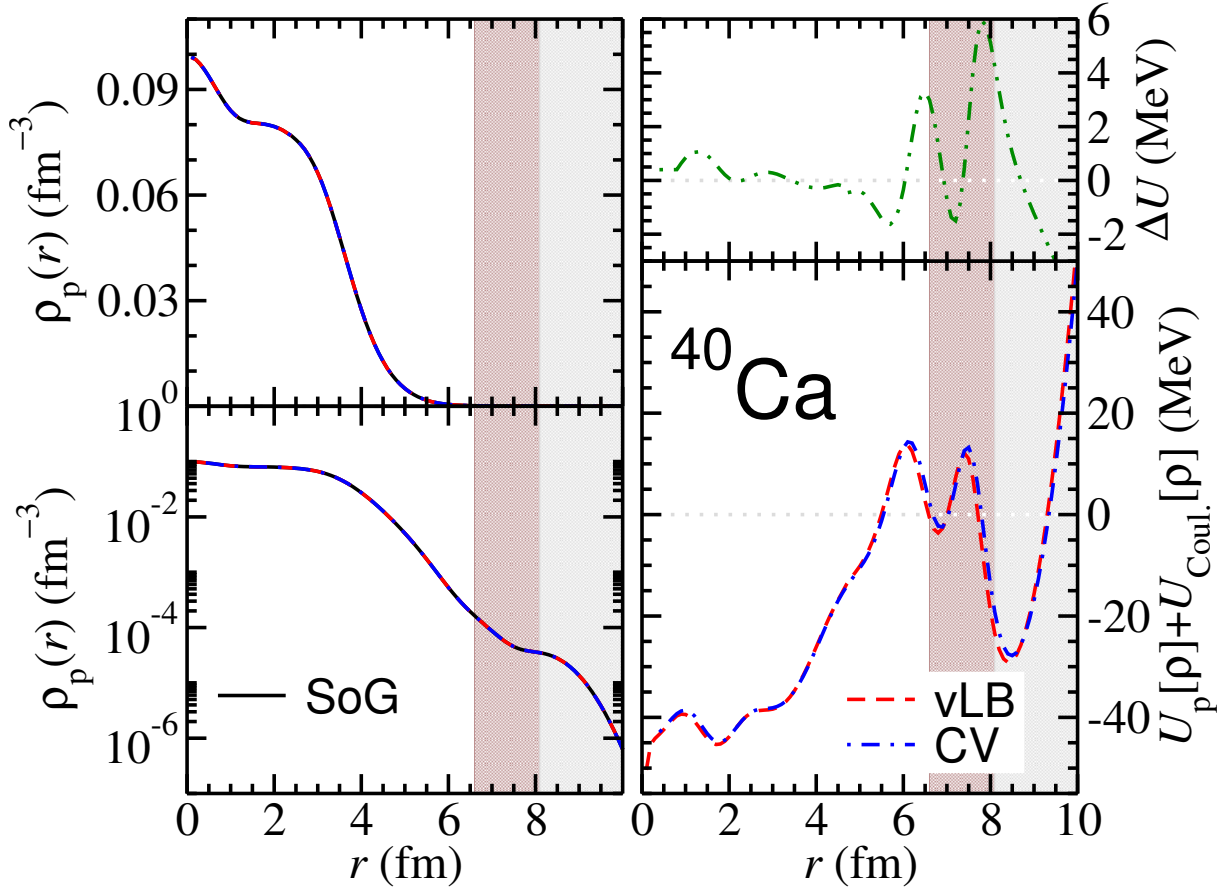
Figure 2.1: The proton density for the case of ^{40}Ca is displayed as a function of the radial coordinate, on a linear scale (top left panel) and on a logarithmic scale (bottom left panel). The target experimental density [1], labeled SoG, (black solid lines), is compared with those obtained with the inversion methods vLB (red dashed lines) and CV (blue dot-dashed lines). In the bottom right panel, the Kohn-Sham potentials obtained within the two inversion methods are compared, and in the top right panel their difference is shown.

Table 2.1: Maximum (Max.) and average (Aver.) differences between the target experimental (SoG) and KS neutron (n) and proton (p) densities from the two inversion methods for the case of ^{40}Ca and ^{208}Pb. Numerical values are all in 10^{-6} fm^{-3}.

Nucleus	vLB		CV	
	Max.	Aver.	Max.	Aver.
^{40}Ca (p)	248.	4.07	0.918	0.16
^{208}Pb (p)	8.40	0.70	0.409	0.11
^{208}Pb (n)	15.4	0.99	0.147	3.61
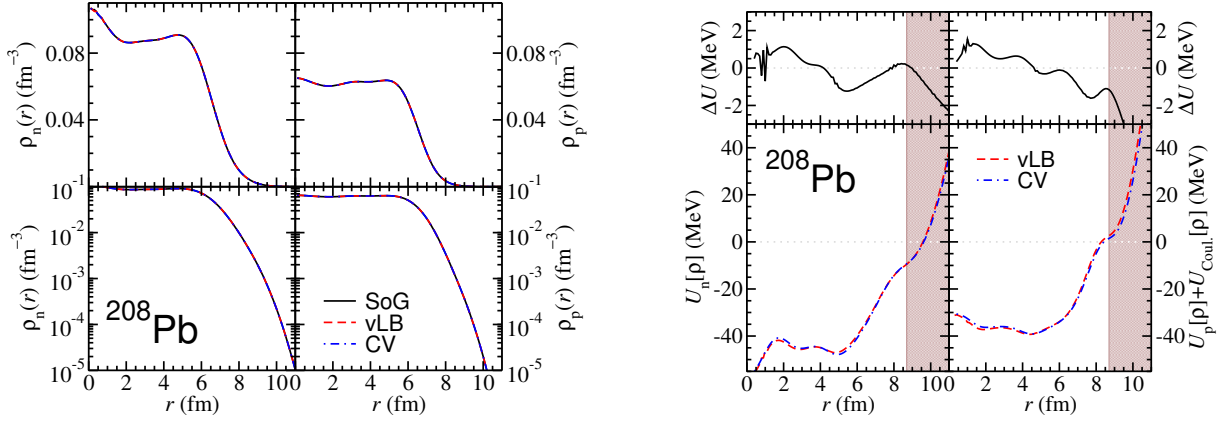
Figure 2.2: *(left figure)* The neutron and proton densities for the case of ^{208}Pb are displayed as a function of the radial coordinate, on a linear scale (top panels) and on a logarithmic scale (bottom panels). The target experimental densities [1, 2], labeled as SoG (black solid lines), are compared with those obtained with the inversion methods vLB (red dashed lines) and CV (blue dot-dashed lines). *(right figure)* The Kohn-Sham potentials calculated for neutrons and protons with the inversion methods vLB (red dashed lines) and CV (blue dot-dashed lines) are shown. In the top panels, the corresponding differences between the Kohn-Sham potentials are displayed.

the non-physical behaviors obtained in the previous section. The test shows that, when the input density are characterized by the correct asymptotic behavior, the derived Kohn-Sham potential is reliable everywhere.

The target densities are obtained by means of Hartree-Fock calculations that use the Skyrme interaction SkX [83]. The interaction contains a spin-orbit potential and an effective mass $m^*(r)$[3]. However, for the specific interaction, these non-local features are almost negligible ($< 8\%$). The logarithmic scale used in the lower panels of Figure 2.4 is crucial to expose the asymptotic behavior of the densities. The test of the inversion algorithms ensures that the obtained results are reliable: the direct KS equations (2.2) are solved, using the obtained KS potentials, to get back the input densities.

Figure 2.4 illustrates a great agreement with the target densities, also visible in table 2.2. Even if both methods satisfactorily reproduce the target densities, the CV method requires much more stringent convergence criteria. Figure 2.4 depicts the KS potentials obtained by the two algorithms. Potentials are defined up to an arbitrary constant, and they have been shifted using

---

[3]The effective mass is the mass that nucleons that move inside the mean field would have if they were freely moving particles, but with an effective mass m^*. In fact, it is calculated by computing the Fourier transformation of the Schrödinger equation of the system, and by setting it equal to the Fourier transformation of the Schrodinger equation of a freely moving, m^*-massive, particle:

$$\frac{\hbar^2 k^2}{2m} + U(k) = \frac{\hbar^2 k^2}{2m^*} \tag{2.43}$$
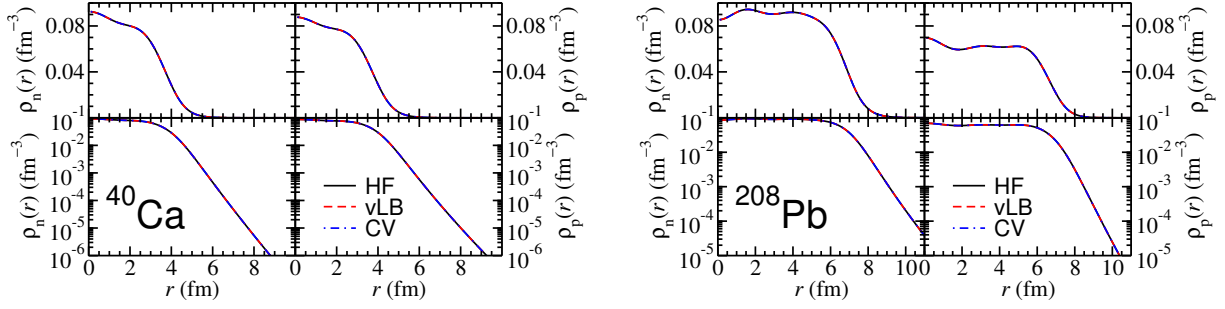
Figure 2.3: The neutron density and proton density of ^{40}Ca (left) and ^{208}Pb (right), in linear (upper panels) and logarithmic scale (lower panels). The target densities obtained from HF calculations (black solid line) are compared with the densities resulting from the two inversion method, vLB (red dashed line) and CV (blue dot-dashed line).

the last occupied eigenvalue obtained with the HF calculations. The absolute value of the difference with respect to the HF potentials is always smaller than 2.5 MeV, a quite good agreement considered the premises mentioned above.

The two algorithms, although they provide analogue results, arrive to convergence in a wildly different way. Figure 2.5 illustrates the evolution of the maximum absolute difference of the KS potential at different steps of the algorithms, in the case of ^{208}Pb, in linear and logarithmic scales. The convergence of the vLB method (red diamonds) is characterized by a brief initial oscillation, up to about five-hundred iterations, after which the difference between the potentials at two successive iterations goes to zero monotonically, at a decreasing rate. Keeping in mind that the CV method does not use the difference between potentials at successive steps as a convergence criterion, but rather attempts to minimize the value of the kinetic energy taking at same time into account the tolerance with which constraints are fulfilled, the points corresponding to different iterations do not decrease with a monotonic trend. Because of this, the convergence of the CV method (blue circles in Figure 2.5) shows an oscillatory behavior, which is particularly clear in the logarithmic scale. Nevertheless, one can see that the trend goes towards smaller values as the iteration proceeds, and eventually the values become small enough to conclude that the final result for the potential is reliable.

2.3   Relativistic Inverse Kohn-Sham Problem

The generalization of the formalism for the solution of the inverse Kohn-Sham problem to the relativistic mean-field framework is presented below. The choice for the inversion algorithm fell on the vLB method, section 2.1.1, simpler to implement and yet guaranteeing a good convergence behavior for closed-shell nuclei.
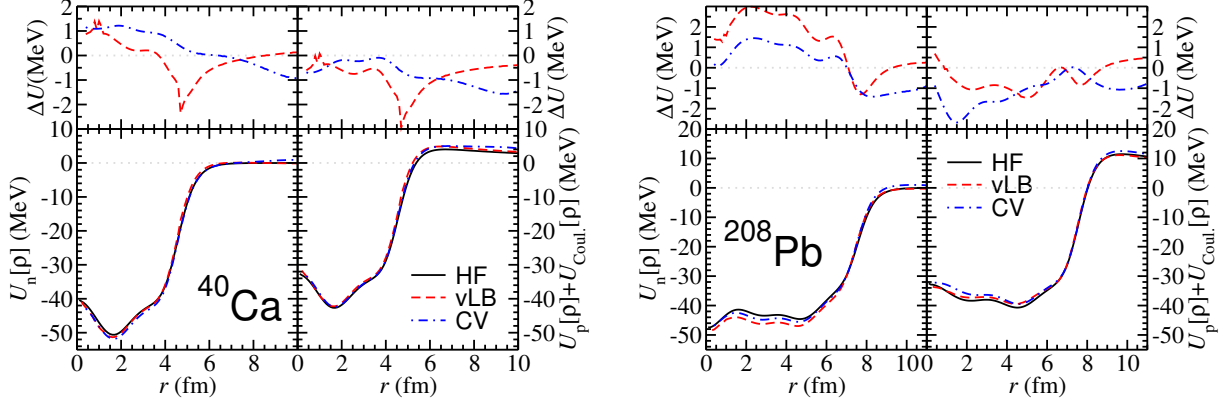
Figure 2.4: The Kohn-Sham potentials obtained with the vLB (red dashed lines) and CV (blue dot-dashed lines) inversion methods for ^{40}Ca (left figure) and ^{208}Pb (right figure). The benchmark HF calculations based on the SkX functional [83] are shown (black solid lines). In the upper panels, the differences between the vLB and CV potential, and the HF potential are shown.

Table 2.2: Maximum (Max.) and average (Aver.) differences between the target HF (SkX) and KS neutron (n) and proton (p) densities from the two inversion methods for the case of ^{40}Ca and ^{208}Pb. Numerical values are all in 10^{-6} fm^{-3}.

Nucleus	vLB		CV	
	Max.	Aver.	Max.	Aver.
^{40}Ca (p)	56.5	1.95	0.97	0.176
^{40}Ca (n)	65.7	2.17	1.03	0.186
^{208}Pb (p)	27.6	0.69	0.44	0.116
^{208}Pb (n)	55.2	4.02	7.5	2.13
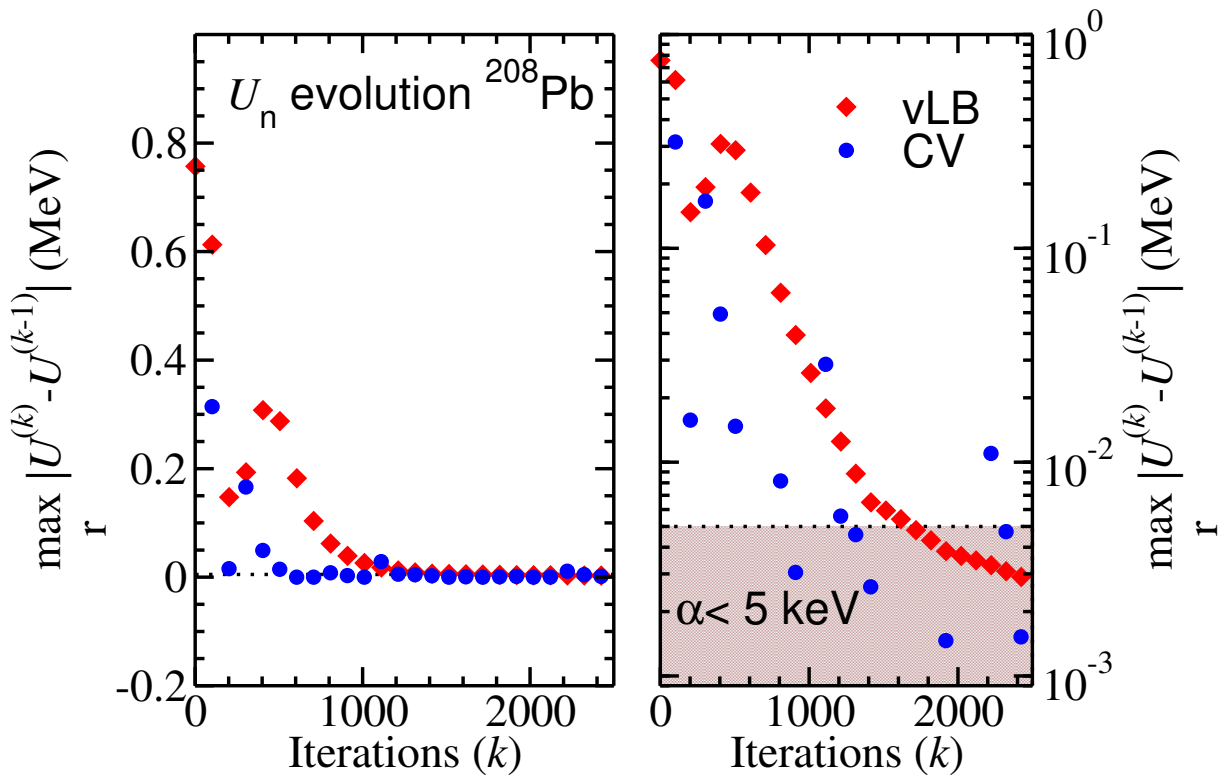
Figure 2.5: The absolute difference (2.9) between the neutron Kohn-Sham potentials for ^{208}Pb calculated at successive iterations is shown at different iteration steps on a linear (left panel) and on a logarithmic (right panel) scale. Results of the inversion method vLB and CV are shown by red diamonds and blue circles, respectively.

One starts from the single-nucleon Dirac Kohn-Sham equation,

$$[\boldsymbol{\alpha p} + \beta(m + S(\mathbf{r}) + V(\mathbf{r})] \psi_j = E_j \psi_j, \tag{2.44}$$

with the scalar and vector Kohn-Sham (KS) potentials, respectively

$$S(\mathbf{r}) = \left. \frac{\delta E[\varrho_V, \varrho_S]}{\delta \varrho_S} \right|_{\varrho_{V,gs}, \varrho_{S,gs}}, \tag{2.45}$$

$$V(\mathbf{r}) = \left. \frac{\delta E[\varrho_V, \varrho_S]}{\delta \varrho_V} \right|_{\varrho_{V,gs}, \varrho_{S,gs}}. \tag{2.46}$$

The corresponding scalar and vector ground-state densities,

$$\varrho_{S,gs} = \sum_{j \in occ} \psi_j^\dagger \beta \psi_j \,, \tag{2.47}$$

$$\varrho_{V,gs} = \sum_{j \in occ} \psi_j^\dagger \psi_j \,, \tag{2.48}$$

are obtained from the solutions of the single-nucleon Dirac KS equation in the no-sea approximation, that omits explicit contributions of negative-energy states to densities and currents [37]. Thus, the sums run only over occupied positive-energy single-nucleon orbitals.

The KS potentials are rewritten according to

$$V_+(\boldsymbol{r}) = V(\boldsymbol{r}) + S(\boldsymbol{r}) \tag{2.49}$$

$$V_-(\boldsymbol{r}) = V(\boldsymbol{r}) - S(\boldsymbol{r}) \,, \tag{2.50}$$

so that Equation (2.44) takes the form

$$\left[\boldsymbol{\alpha p} + \frac{1}{2}(\beta - \mathbb{1})(m - V_-(\boldsymbol{r})) + \frac{1}{2}(\beta + \mathbb{1})(m + V_+(\boldsymbol{r})) \right] \psi_j = E_j \psi_j \,. \tag{2.51}$$

By multiplying Equation (2.51) with $\psi_j^\dagger$ from the left, and summing over the occupied positive-energy states, one obtains:

$$\sum_{j \in occ} \psi_j^\dagger (\boldsymbol{\alpha p} - E_j)\psi_j + \frac{1}{2}(m - V_-) \sum_{j \in occ} \psi_j^\dagger(\beta - \mathbb{1})\psi_j +$$
$$+ \frac{1}{2}(m + V_+) \sum_{j \in occ} \psi_j^\dagger(\beta + \mathbb{1})\psi_j = 0 \,. \tag{2.52}$$

The vector and scalar densities that appear in this expression can be recombined according to $\varrho_+ = \varrho_V + \varrho_S$, $\varrho_- = \varrho_V - \varrho_S$, and are inserted into Equation (2.52):

$$\sum_{j \in occ} \psi_j^\dagger (\boldsymbol{\alpha p} - E_j)\psi_j - \frac{1}{2}(m - V_-)\varrho_- + \frac{1}{2}(m + V_+)\varrho_+ = 0 \,. \tag{2.53}$$

If Equation (2.51) is multiplied by $\bar{\psi}_j$, the following expression is obtained:

$$\sum_{j \in occ} \bar{\psi}_j (\boldsymbol{\alpha p} - E_j)\psi_j + \frac{1}{2}(m - V_-)\varrho_- + \frac{1}{2}(m + V_+)\varrho_+ = 0. \tag{2.54}$$

Finally, by adding and subtracting equations (2.53) and (2.54):

$$\sum_{j \in occ} (\psi_j^\dagger + \bar{\psi}_j)(\boldsymbol{\alpha p} - E_j)\psi_j + (m + V_+)\varrho_+ = 0 \,, \tag{2.55}$$

$$\sum_{j \in occ} (\psi_j^\dagger - \bar{\psi}_j)(\boldsymbol{\alpha p} - E_j)\psi_j + (V_- - m)\varrho_- = 0 \,. \tag{2.56}$$

From the previous two equations, the Kohn-Sham potentials V_+ and V_- are expressed by:

$$V_+ = -m - \frac{1}{\varrho_+} \sum_{j \in occ} (\psi_j^\dagger + \bar{\psi}_j)(\boldsymbol{\alpha p} - E_j)\psi_j \,, \tag{2.57}$$

$$V_- = m - \frac{1}{\varrho_-} \sum_{j \in occ} (\psi_j^\dagger - \bar{\psi}_j)(\boldsymbol{\alpha p} - E_j)\psi_j \,. \tag{2.58}$$

The set of IKS equations (2.57) and (2.58) can be solved iteratively. In the philosophy the vLB method, one takes the densities in the denominator as the target densities, and use equations (2.55) and (2.56) in the numerator to define the densities and the potentials at the k-th step. The resulting potentials at the $(k + 1)$-th step read

$$V_+^{(k+1)} = \frac{\varrho_+^{(k)}}{\varrho_+} V_+^{(k)} + m \frac{\varrho_+^{(k)} - \varrho_+}{\varrho_+} \,, \tag{2.59}$$

$$V_-^{(k+1)} = \frac{\varrho_-^{(k)}}{\varrho_-} V_-^{(k)} - m \frac{\varrho_-^{(k)} - \varrho_-}{\varrho_-} \,. \tag{2.60}$$

As explained in section 2.1.1, the iterative rules of equations (2.59) and (2.60) are modified in

the following way,

$$V_+^{(k)} = V_+^{(k-1)} + \gamma_+ \frac{\varrho_+^{(k)} - \varrho_+}{\varrho_+} \, , \tag{2.61}$$

$$V_-^{(k)} = V_-^{(k-1)} + \gamma_- \frac{\varrho_-^{(k)} - \varrho_-}{\varrho_-} \, , \tag{2.62}$$

where $\gamma_\pm = 1$ MeV

In actual calculations some stability issues have been encountered for large values of the radial coordinate, due to the small values of the denominators in equations (2.61) and (2.62), beyond the nuclear radius. This problem can be solved by introducing a cut-off radius r_{cut}, and setting the potentials to zero for $r > r_{cut}$. For the initial KS potential a realistic Woods-Saxon potential is used, and the Broyden mixing procedure [84] is employed to solve equations (2.61) and (2.62). The convergence criterion used to terminate the iterative IKS algorithm is the same of the vLB method, Equation (2.9), but now applied to the scalar and vector KS potentials, separately:

$$\Delta V_\pm^{(k)} \equiv \max_r [V_\pm^{(k+1)}(r) - V_\pm^{(k)}(r)] < \alpha_\pm \, . \tag{2.63}$$

2.4 DFPT+IKS Model

The method originally presented in [85] has been adopted to the nuclear relativistic mean-field framework and applied to improve a relativistic NEDF, starting from given empirical ground-state densities. From here on, the model will be denoted as DFPT+IKS model. It is assumed that the interaction, the unknown yet exact Hartree-exchange-correlation functional, can be written in the following form:

$$E_{int}[\varrho] = E_{int}^{(0)}[\varrho] + \lambda E_{int}^{(1)}[\varrho] + \mathcal{O}(\lambda^2) \, , \tag{2.64}$$

where $E_{int}^{(0)}[\varrho]$ denotes the known functional whose accuracy one wishes to improve, and λ is a small parameter. The main assumption of the method is then that the difference between the exact functional $E[\varrho]$ and the initial functional $E^{(0)}[\varrho]$ is small enough for a first-order perturbative treatment. The correction is determined by the exact ground-state density via the information extracted from the inverse Kohn-Sham (IKS) approach.

The exact Dirac spinors, that is, the solutions of Equation (2.44) for the exact energy density

functional, can also be expanded to the first order in λ,

$$\psi(\mathbf{r}) = \psi^{(0)}(\mathbf{r}) + \lambda \psi^{(1)}(\mathbf{r}) + \mathcal{O}(\lambda^2) \, , \tag{2.65}$$

and one assumes that the first-order correction is orthogonal to the zeroth-order spinor,

$$\int \psi^{(0)\dagger}(\mathbf{r})\psi^{(1)}(\mathbf{r})d\mathbf{r} = 0 \, . \tag{2.66}$$

The corresponding exact ground-state densities

$$\varrho_{V,gs}(\mathbf{r}) = \sum_{j \in occ} \psi_j^{(0)\dagger}(\mathbf{r})\psi_j^{(0)}(\mathbf{r})+$$
$$+ \lambda \left(\sum_{j \in occ} \psi_j^{(1)\dagger}(\mathbf{r})\psi_j^{(0)}(\mathbf{r}) + \sum_{j \in occ} \psi_j^{(0)\dagger}(\mathbf{r})\psi_j^{(1)}(\mathbf{r}) \right) + \mathcal{O}(\lambda^2) \, , \tag{2.67}$$

$$\varrho_{S,gs}(\mathbf{r}) = \sum_{j \in occ} \psi_j^{(0)\dagger}(\mathbf{r})\beta\psi_j^{(0)}(\mathbf{r})+$$
$$+ \lambda \left(\sum_{j \in occ} \psi_j^{(1)\dagger}(\mathbf{r})\beta\psi_j^{(0)}(\mathbf{r}) + \sum_{j \in occ} \psi_j^{(0)\dagger}(\mathbf{r})\beta\psi_j^{(1)}(\mathbf{r}) \right) + \mathcal{O}(\lambda^2) \, , \tag{2.68}$$

take the form:

$$\varrho_{V(S),gs}(\mathbf{r}) = \varrho_{V(S)}^{(0)}(\mathbf{r}) + \lambda\varrho_{V(S)}^{(1)}(\mathbf{r}) + \mathcal{O}(\lambda^2) \, , \tag{2.69}$$

where the first term on the right-hand side denotes the densities that correspond to the known functional. It is assumed that, given the exact densities $\varrho_{V(S),gs}(\mathbf{r})$, one can use the IKS method to calculate the exact Dirac spinors $\psi_j(\mathbf{r})$ and single-nucleon energies ϵ_j.

The ground-state energy can be decomposed as follows:

$$E_{gs} = E_{kin}[\varrho_{gs}] + E_{int}^{(0)}[\varrho_{gs}] + \lambda E_{int}^{(1)}[\varrho_{gs}] \, , \tag{2.70}$$

where the relativistic Kohn-Sham kinetic energy reads

$$E_{kin}[\varrho_{gs}] = \sum_{j \in occ} \int \psi_j^\dagger(\mathbf{r})\hat{t}\psi_j(\mathbf{r})d\mathbf{r} \, , \tag{2.71}$$

and $\hat{t} = \boldsymbol{\alpha}\mathbf{p} + \beta m$. By expanding the Dirac spinors as in Equation (2.65) and retaining only

those terms that are linear in λ, the following expression for the kinetic energy is obtained:

$$E_{kin}[\varrho_{gs}] = \sum_{j \in occ} \int \psi_j^{(0)\dagger}(\mathbf{r}) \hat{t} \psi_j^{(0)}(\mathbf{r}) d\mathbf{r}$$

$$+ \lambda \sum_{j \in occ} \int \psi_j^{(1)\dagger}(\mathbf{r}) \hat{t} \psi_j^{(0)}(\mathbf{r}) d\mathbf{r}$$

$$+ \lambda \sum_{j \in occ} \int \psi_j^{(0)\dagger}(\mathbf{r}) \hat{t} \psi_j^{(1)}(\mathbf{r}) d\mathbf{r} + \mathcal{O}(\lambda^2). \tag{2.72}$$

The second and third term on the right-hand side of Equation (2.70) denote the interaction (Hartree exchange-correlation) contribution to the total energy. Using the expansion of Equation (2.69) for the ground-state densities, up to terms linear in λ, one derives:

$$E_{int}^{(0)}[\varrho_{V,gs}, \varrho_{S,gs}] = E_{int}^{(0)}[\varrho_{V,gs}^{(0)}, \varrho_{S,gs}^{(0)}] + \lambda \int \left. \frac{\delta E_{int}^{(0)}}{\delta \varrho_V} \right|_{\varrho_{V,gs}^{(0)}, \varrho_{S,gs}^{(0)}} \varrho_{V,gs}^{(1)} \, d\mathbf{r}$$

$$+ \lambda \int \left. \frac{\delta E_{int}^{(0)}}{\delta \varrho_S} \right|_{\varrho_{V,gs}^{(0)}, \varrho_{S,gs}^{(0)}} \varrho_{S,gs}^{(1)} \, d\mathbf{r} + \mathcal{O}(\lambda^2), \tag{2.73}$$

$$\lambda E_{int}^{(1)}[\varrho_{V,gs}, \varrho_{S,gs}] = \lambda E_{int}^{(1)}[\varrho_{V,gs}^{(0)}, \varrho_{S,gs}^{(0)}] + \mathcal{O}(\lambda^2) . \tag{2.74}$$

Inserting expressions (2.67) and (2.68) for the first-order density corrections $\varrho_{V,gs}^{(1)}$ and $\varrho_{S,gs}^{(1)}$, respectively, into the expansion for the interaction energy, equations (2.73) and (2.74), together with the expression for the kinetic energy, Equation (2.72), the ground-state energy reads:

$$E_{gs} = E_{kin}^{(0)} + E_{int}^{(0)}[\varrho_{V,gs}^{(0)}, \varrho_{S,gs}^{(0)}]$$

$$+ \lambda \sum_{j \in occ} \int \psi_j^{(1)\dagger}(\mathbf{r}) \left[\hat{t} + \left. \frac{\delta E_{int}^{(0)}}{\delta \varrho_V} \right|_{\varrho_{V,gs}^{(0)}, \varrho_{S,gs}^{(0)}} + \beta \left. \frac{\delta E_{int}^{(0)}}{\delta \varrho_S} \right|_{\varrho_{V,gs}^{(0)}, \varrho_{S,gs}^{(0)}} \right] \psi_j^{(0)}(\mathbf{r}) d\mathbf{r}$$

$$+ \lambda \sum_{j \in occ} \int \psi_j^{(0)\dagger}(\mathbf{r}) \left[\hat{t} + \left. \frac{\delta E_{int}^{(0)}}{\delta \varrho_V} \right|_{\varrho_{V,gs}^{(0)}, \varrho_{S,gs}^{(0)}} + \beta \left. \frac{\delta E_{int}^{(0)}}{\delta \varrho_S} \right|_{\varrho_{V,gs}^{(0)}, \varrho_{S,gs}^{(0)}} \right] \psi_j^{(1)}(\mathbf{r}) d\mathbf{r}$$

$$+ \lambda E_{int}^{(1)}[\varrho_{V,gs}^{(0)}, \varrho_{S,gs}^{(0)}] + \mathcal{O}(\lambda^2) . \tag{2.75}$$

The expression in square brackets represent the zeroth-order (unperturbed) Dirac Hamiltonian, that is

$$\left[\hat{t} + \left. \frac{\delta E_{int}^{(0)}}{\delta \varrho_V} \right|_{\varrho_{V,gs}^{(0)}, \varrho_{S,gs}^{(0)}} + \beta \left. \frac{\delta E_{int}^{(0)}}{\delta \varrho_S} \right|_{\varrho_{V,gs}^{(0)}, \varrho_{S,gs}^{(0)}} \right] \psi_j^{(0)} = \epsilon_j^{(0)} \psi_j^{(0)} . \tag{2.76}$$

The orthogonality relation (2.66) ensures that the corresponding terms in Equation (2.75) vanish, and the following relation for the ground-state energy is obtained:

$$E_{gs} = E_{kin}^{(0)} + E_{int}^{(0)}[\varrho_{V,gs}^{(0)}, \varrho_{S,gs}^{(0)}] + \lambda E_{int}^{(1)}[\varrho_{V,gs}^{(0)}, \varrho_{S,gs}^{(0)}] + \mathcal{O}(\lambda^2) \, . \tag{2.77}$$

On the other hand, the ground-state energy $E_{gs} = E_{kin}[\varrho_{gs}] + E_{int}[\varrho_{gs}]$, can be also written in the following form:

$$\begin{aligned} E_{gs} = &\sum_{j \in occ} \epsilon_j + E_{int}[\varrho_{V,gs}, \varrho_{S,gs}] \\ &- \int \left.\frac{\delta E_{int}}{\delta \varrho_V}\right|_{gs} \varrho_{V,gs}(\mathbf{r}) d\mathbf{r} - \int \left.\frac{\delta E_{int}}{\delta \varrho_S}\right|_{gs} \varrho_{S,gs}(\mathbf{r}) d\mathbf{r} \, , \end{aligned} \tag{2.78}$$

where the Dirac Kohn-Sham equation has been used to eliminate the explicit contribution of the kinetic energy term, and ϵ_j are the exact single-particle energies summed over occupied states. If one separates zeroth-order terms from the first-order terms of the exact interaction functional $E_{int}[\varrho_{gs}]$, then

$$\begin{aligned} E_{gs} = &\sum_{j \in occ} \epsilon_j + E_{int}^{(0)}[\varrho_{V,gs}, \varrho_{S,gs}] \\ &- \int \left.\frac{\delta E_{int}^{(0)}}{\delta \varrho_V}\right|_{gs} \varrho_{V,gs}(\mathbf{r}) d\mathbf{r} - \int \left.\frac{\delta E_{int}^{(0)}}{\delta \varrho_S}\right|_{gs} \varrho_{S,gs}(\mathbf{r}) d\mathbf{r} \\ &+ \lambda E_{int}^{(1)}[\varrho_{V,gs}, \varrho_{S,gs}] \\ &- \lambda \int \left.\frac{\delta E_{int}^{(1)}}{\delta \varrho_V}\right|_{gs} \varrho_{V,gs}(\mathbf{r}) d\mathbf{r} - \lambda \int \left.\frac{\delta E_{int}^{(1)}}{\delta \varrho_S}\right|_{gs} \varrho_{S,gs}(\mathbf{r}) d\mathbf{r} \, . \end{aligned} \tag{2.79}$$

Using Equation (2.77), one can express the first-order correction to the interaction energy as a function of the zeroth-order ground-state densities,

$$\lambda E_{int}^{(1)}[\varrho_{V,gs}^{(0)}, \varrho_{S,gs}^{(0)}] = E_{gs} - E_{kin}^{(0)} - E_{int}^{(0)}[\varrho_{V,gs}^{(0)}, \varrho_{S,gs}^{(0)}] = E_{gs} - E_{gs}^{(0)} \, , \tag{2.80}$$

where $E_{gs}^{(0)}$ denotes the ground-state energy calculated from the known functional.

Next, Equation (2.79) is inserted into the previous expression, and the following relation is

obtained:

$$
\lambda E_{int}^{(1)}[\varrho_{V,gs}^{(0)}, \varrho_{S,gs}^{(0)}] = \sum_{j \in occ} \epsilon_j + E_{int}^{(0)}[\varrho_{V,gs}, \varrho_{S,gs}]
$$

$$
- \int \left. \frac{\delta E_{int}^{(0)}}{\delta \varrho_V} \right|_{gs} \varrho_{V,gs}(\mathbf{r}) d\mathbf{r} - \int \left. \frac{\delta E_{int}^{(0)}}{\delta \varrho_S} \right|_{gs} \varrho_{S,gs}(\mathbf{r}) d\mathbf{r}
$$

$$
- E_{gs}^{(0)} + \lambda E_{int}^{(1)}[\varrho_{V,gs}, \varrho_{S,gs}]
$$

$$
- \lambda \int \left. \frac{\delta E_{int}^{(1)}}{\delta \varrho_V} \right|_{gs} \varrho_{V,gs}(\mathbf{r}) d\mathbf{r} - \lambda \int \left. \frac{\delta E_{int}^{(1)}}{\delta \varrho_S} \right|_{gs} \varrho_{S,gs}(\mathbf{r}) d\mathbf{r} \ . \tag{2.81}
$$

Equation (2.81) gets rearranged so that all terms linear in λ (first-order corrections to the interaction functional) wind up on the left-hand side,

$$
\lambda E_{int}^{(1)}[\varrho_{V,gs}^{(0)}, \varrho_{S,gs}^{(0)}] - \lambda E_{int}^{(1)}[\varrho_{V,gs}, \varrho_{S,gs}]
$$

$$
+ \lambda \int \left. \frac{\delta E_{int}^{(1)}}{\delta \varrho_V} \right|_{gs} \varrho_{V,gs}(\mathbf{r}) d\mathbf{r} + \lambda \int \left. \frac{\delta E_{int}^{(1)}}{\delta \varrho_S} \right|_{gs} \varrho_{S,gs}(\mathbf{r}) d\mathbf{r}
$$

$$
= \sum_{j \in occ} \epsilon_j + E_{int}^{(0)}[\varrho_{V,gs}, \varrho_{S,gs}] - E_{gs}^{(0)}
$$

$$
- \int \left. \frac{\delta E_{int}^{(0)}}{\delta \varrho_V} \right|_{gs} \varrho_{V,gs}(\mathbf{r}) d\mathbf{r} - \int \left. \frac{\delta E_{int}^{(0)}}{\delta \varrho_S} \right|_{gs} \varrho_{S,gs}(\mathbf{r}) d\mathbf{r} \ . \tag{2.82}
$$

The right-hand side of the last equation depends only on the exact ground-state densities and the known functional $E_{int}^{(0)}$. Given the scalar and vector ground-state empirical densities one can calculate all terms on the right-hand side, except for the first term, sum of the exact single-particle energies. The energies are implicit functionals of the exact ground-state densities. To this end, one uses the KS energy levels obtained with the relativistic IKS method exposed in the previous section.

In practical applications, one should assume a certain *Ansatz* for the functional $E_{int}^{(1)}[\varrho]$, that will also include parameters to be determined from Equation (2.82) for a choice of empirical ground-state densities. There is no guarantee, especially in the case of several undetermined parameters for the first-order correction, that the improved functional will reproduce the exact densities to a desired level of accuracy. The solution is a self-consistent procedure in which the functional improved in one iteration is considered as the known functional for the successive

iteration step:

$$E_{int}^{(k)}[\varrho] = E_{int}^{(0)}[\varrho] + \sum_{n=1}^{k} \lambda E_{int}^{(1),(n)}[\varrho] \; ; \tag{2.83}$$

the procedure is repeated until the exact densities are reproduced by the solutions of the resulting k^{th} iteration Dirac KS equation up to a desired accuracy.

Two tests of the method, used to improve an approximate EDF towards the exact one, are presented below for $N = Z$ systems without Coulomb interaction. An existing relativistic EDF is used as the exact target functional, and the method is applied to improve different approximate functionals towards it. In real nuclei the exact functional is unknown, and ground-state data is not sufficient to determine the functional dependence on various nuclear densities.

2.4.1   First test of the model

As a target NEDF, the relativistic functional DD-PC1 [53] has been used. The single-nucleon Hamiltonian reads

$$\hat{h} = \boldsymbol{\alpha}\boldsymbol{p} + \beta[m + S(\boldsymbol{r})] + V_0(\boldsymbol{r}) + \Sigma_R(\boldsymbol{r}) \; , \tag{2.84}$$

where the scalar potential, vector potential, and rearrangement terms are respectively defined as

$$
\begin{aligned}
S &= \alpha_S(\varrho)\varrho_S + \delta_S \triangle \varrho_S \; , \\
V &= \alpha_V(\varrho)\varrho_V + \alpha_{TV}(\varrho)\vec{\varrho}_{TV} \cdot \vec{\tau} + e\frac{1-\tau_3}{2}A_0 \; , \\
\Sigma_R &= \frac{1}{2}\frac{\partial\alpha_S}{\partial\varrho}\varrho_S^2 + \frac{1}{2}\frac{\partial\alpha_V}{\partial\varrho}\varrho_V^2 + \frac{1}{2}\frac{\partial\alpha_{TV}}{\partial\varrho}\varrho_{TV}^2 \; ;
\end{aligned}
\tag{2.85}
$$

m is the nucleon mass, $\alpha_S(\varrho)$, $\alpha_V(\varrho)$, and $\alpha_{TV}(\varrho)$ are density-dependent couplings for different space-isospace channels, δ_S is the coupling constant of the derivative term, e is the electric charge, ϱ_S the single-nucleon scalar-isoscalar density, ϱ_V the time-like component of the isoscalar current, and ϱ_{TV} the time-like component of the isovector current. In addition to the contributions from the isoscalar-vector four-fermion interaction and the electromagnetic interaction, the isoscalar-vector self-energy includes the rearrangement terms in Σ_R, that arise from the variation of the vertex functionals α_S, α_V, and α_{TV} with respect to the nucleon fields in the vector density operator ϱ_V. Guided by the microscopic density-dependence of the vector and scalar self-energies, the following practical *Ansatz* for the functional form of the couplings was

adopted in [53]:

$$\alpha_S(\varrho) = a_s + (b_s + c_s x)e^{-d_s x} \,,$$

$$\alpha_V(\varrho) = a_v + b_v e^{-d_v x} \,, \tag{2.86}$$

$$\alpha_{TV}(\varrho) = b_{tv} e^{-d_{tv} x} \,,$$

with $x = \varrho/\varrho_{\mathrm{sat}}$, ϱ_{sat} denoting the nucleon density at saturation in symmetric nuclear matter.

In the simplified case of $N = Z$ doubly closed-shell nuclei without Coulomb interaction, there is no contribution of the isovector channel. Four $N = Z$ systems, ^{16}O, ^{40}Ca, ^{56}Ni and ^{100}Sn, have been used to improve, starting from the exact ground-state densities, approximate zeroth-order functionals towards DD-PC1. The accuracy of the IKS scheme in determining the Kohn-Sham potentials for given scalar and vector densities is discussed for the $N = Z = 8$ system. The densities-to-potentials inversion enables the calculation of the single-particle energies that appear on the right-hand side of Equation (2.82). Figure 2.6 compares the densities obtained in the inverse Kohn-Sham scheme to the target DD-PC1 densities. Without Coulomb interaction the proton densities are, of course, completely identical to the neutron ones. In all four panels the dash-dotted green curves denote the target densities calculated with the DD-PC1 functional, the dashed red curves are the initial densities that correspond to Woods-Saxon potentials and, finally, the solid black curves represent the final densities obtained by the inversion method. The KS potentials are shown in Figure 2.7. The result is that the target and final IKS densities and potentials are indistinguishable. The latter can, therefore, be used to calculate the single-particle energies that are needed for the application of the model based on DFPT.

In the first test of the model the initial functional $E_{int}^{(0)}[\varrho]$ is taken as a simple functional, that is actually a part of the DD-PC1 functional itself:

$$E_{int}^{(0)}[\varrho_V, \varrho_S] = \frac{1}{2}\alpha_s^{(0)}\varrho_S^2 + \frac{1}{2}\alpha_v^{(0)}\varrho_V^2 + \delta_s \varrho_s \triangle \varrho_s \,. \tag{2.87}$$

The values for the $a_s^{(0)}$ and $a_v^{(0)}$ constants are the same used in the DD-PC1 functional, namely $a_s^{(0)} = a_s = -10.4602$ fm^{-2} and $a_v^{(0)} = a_v = 5.9195$ fm^{-2}. The same choice is made for the derivative term, $\delta_s = -0.8149$. The first two terms of the functional coincide with the simple Walečka mean-field model which, by means of two parameters only, manages to produces a realistic equation of state of symmetric nuclear matter. Such a model, in fact, corresponds to a local density approximation (LDA) for the DD-PC1 energy density functional. The derivative
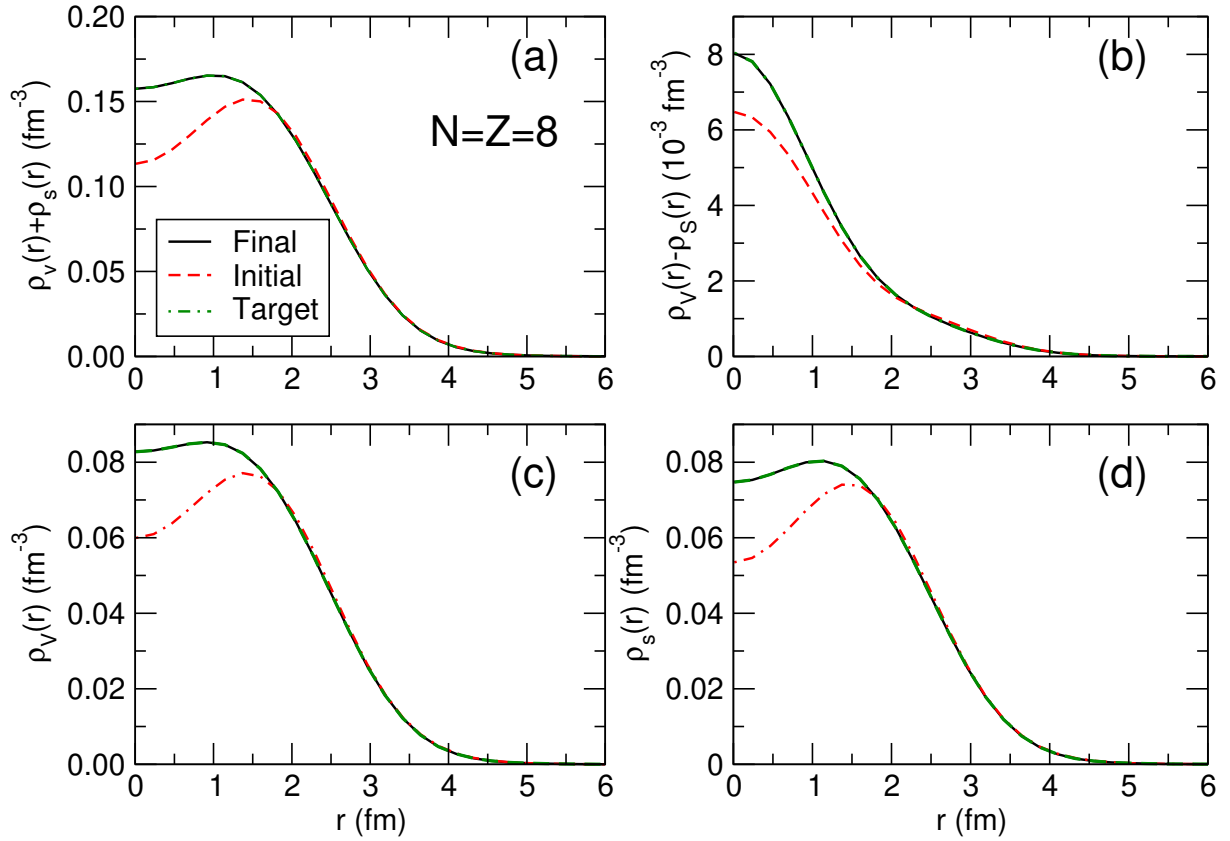
Figure 2.6: *(a)*: The sum of neutron vector and scalar densities in the $N = Z = 8$ system as a function of the radial coordinate. The target density obtained using the DD-PC1 functional (dashed green curve) is compared to the the density calculated in the initial step of the inversion method (dot-dashed red) with a Woods-Saxon potential, and to the final IKS density (solid black). *(b)*: Same as in panel *(a)* but for the difference between the neutron vector and scalar densities. *(c)*: Same as in panel *(a)* but for the neutron vector density. *(d)*: Same as panel in *(a)* but for the neutron scalar density.
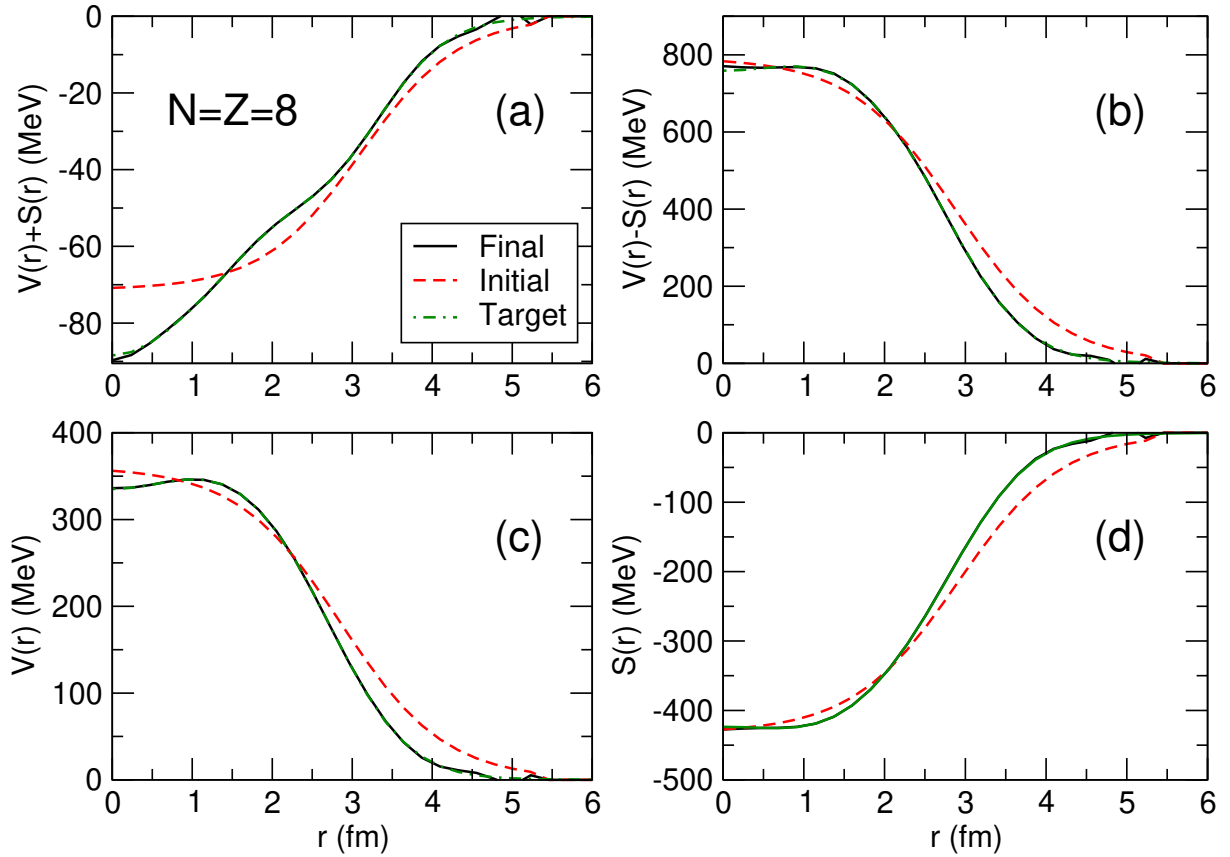
Figure 2.7: *(a)*: The sum of neutron vector and scalar potentials in the $N = Z = 8$ system as a function of the radial coordinate. The target DD-PC1 Kohn-Sham potential (dashed green curve) is compared to the initial Woods-Saxon potential (dot-dashed red), and to the final IKS potential (solid black). *(b)*: Same as in panel *(a)* but for the difference between the neutron vector and scalar potentials. *(c)*: Same as in panel *(a)* but for the neutron vector potential. *(d)*: Same as panel in *(a)* but for the neutron scalar potential.

term is used to model finite systems, and takes into account the rapid variations of the density at the surface region. The strength parameter of this term can be determined qualitatively from microscopic calculations of non-homogeneous nuclear matter.

The remaining, unknown, part of the functional, that is $E_{int}^{(1)}[\varrho]$, is chosen in the following way:

$$E_{int}^{(1)}[\varrho_V, \varrho_S] = \frac{1}{2}\alpha_s^{(1)}(\varrho_V)\varrho_S^2 + \frac{1}{2}\alpha_v^{(1)}(\varrho_V)\varrho_V^2 \ , \tag{2.88}$$

where $\alpha_s^{(1)}(\varrho_V)$ and $\alpha_v^{(1)}(\varrho_V)$ have the functional form of the density-dependent parts of the DD-PC1 couplings,

$$\alpha_s^{(1)}(\varrho_V) = \left(b_s^{(1)} + c_s^{(1)}x\right)e^{-d_s x} \tag{2.89}$$

$$\alpha_v^{(1)}(\varrho_V) = b_v^{(1)}e^{-d_v x} \ , \tag{2.90}$$

with $x = \varrho_v/\varrho_{sat}$, and $\varrho_{sat} = 0.152$ fm^{-3}. The first test of the method consists in determining the parameters of $E_{int}^{(1)}[\varrho]$ by using density functional perturbation theory in combination with the information given by the solution of the inverse Kohn-Sham scheme, using Equation (2.82). Since the right-hand side of this equation is just a number that can be evaluated once the the exact single-particle energies are provided, and the vector and scalar densities are known, a different finite system is needed to calculate each parameter of the unknown functional. Three $N = Z$ systems are employed to this end: ^{16}O, ^{56}Ni and ^{100}Sn to determine the constants $b_s^{(1)}$, $c_s^{(1)}$ and $b_v^{(1)}$, while d_s and d_v are left fixed to their DD-PC1 values. Albeit the problem has been simplified up to a certain extent, the test is far from being trivial: only three artificial systems are used to reproduce the values of parameters that were originally adjusted to the experimental masses of a large number of nuclei. Moreover, since the choice for the unperturbed functional is not close to the exact target functional, it is far from obvious that a first order perturbation method will determine the unknown parameters with sufficient accuracy. Hence, the calculation is repeated in several iterative steps, as described in the previous section, and at each step the values of $b_s^{(1)}$, $c_s^{(1)}$ and $b_v^{(1)}$ are improved. Figure 2.8 displays the values of $(b_s^{(1)})_i$, $(c_s^{(1)})_i$ and $(b_v^{(1)})_i$ at each iteration step. Assuming that nothing is known about these parameters, one starts from zero values. After some initial oscillations in the first few steps, especially between $c_s^{(1)}$ and $b_v^{(1)}$, the parameters converge to the values corresponding to the DD-PC1 target functional, denoted by the horizontal lines in Figure 2.8. The results of this first test demonstrate the feasibility of the model for nuclear densities, as well as the convergence and accuracy of the
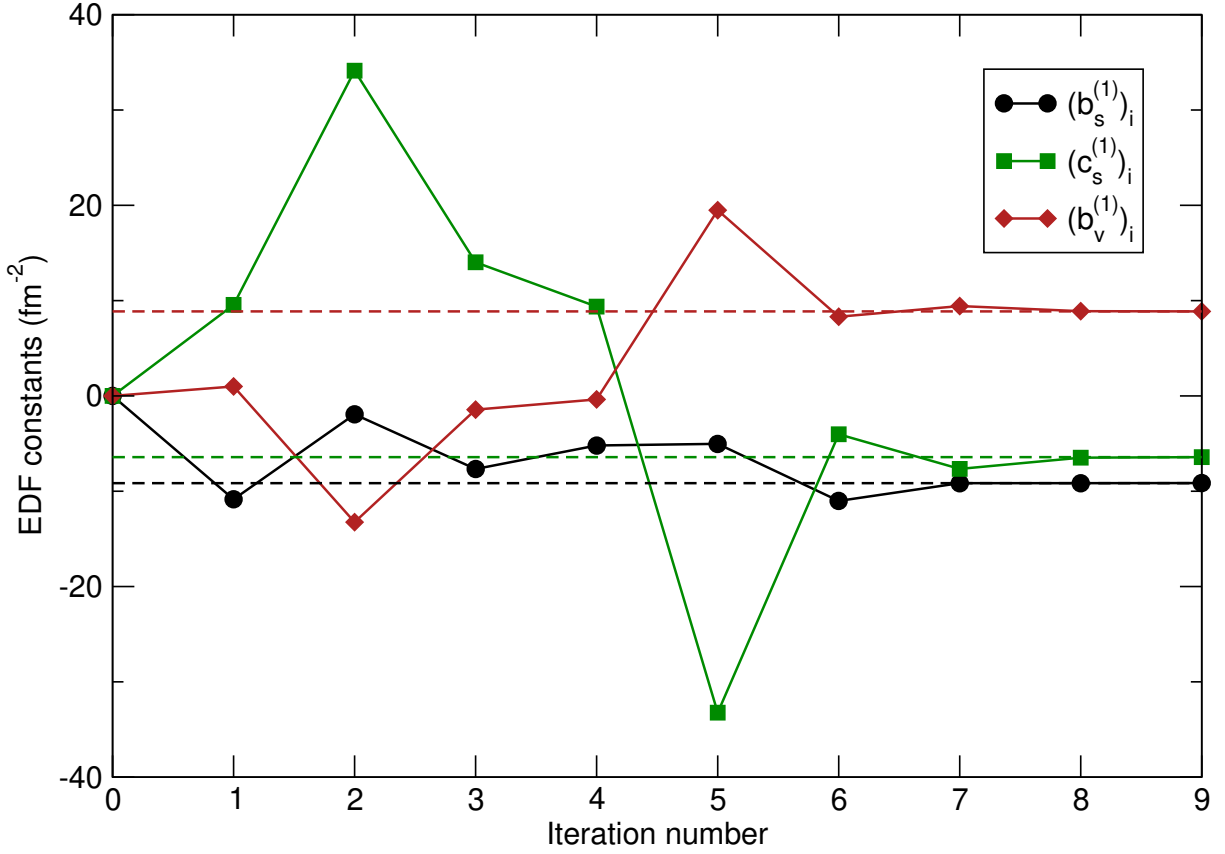
Figure 2.8: Values of the constants $(b_s^{(1)})_i$, $(c_s^{(1)})_i$ and $(b_v^{(1)})_i$ at different iteration steps. The dashed lines denote the target values that correspond to the functional DD-PC1.

iteration scheme.

2.4.2 Second test of the model

In the second test of the model the DD-PC1 EDF has been again used as the target functional, and the corresponding exact single-particle energies appearing on the right-hand side of Equation (2.82) are obtained by the inverse Kohn-Sham method as described in section 2.3. For the known functional $E_{int}^{(0)}[\varrho]$, the simple LDA form of Equation (2.87) has been adopted again with the DD-PC1 values of the three parameters. Instead, for the remaining unknown part of the functional,

$$E_{int}^{(1)}[\varrho_V, \varrho_S] = \frac{1}{2}\alpha_s^{(1)}(\varrho_V)\varrho_S^2 + \frac{1}{2}\alpha_v^{(1)}(\varrho_V)\varrho_V^2 \,,$$

a polynomial density-dependence is now chosen for the coupling parameters $\alpha_s^{(1)}(\varrho_V)$ and $\alpha_v^{(1)}(\varrho_V)$,

$$\alpha_s^{(1)}(\varrho_V) = b_s^{(1)}(x - 1) + c_s^{(1)}(x - 1)^2 \tag{2.91}$$

$$\alpha_v^{(1)}(\varrho_V) = b_v^{(1)}(x - 1) + c_v^{(1)}(x - 1)^2 , \tag{2.92}$$

with $x = \varrho_v/\varrho_{sat}$, and $\varrho_{sat} = 0.152\,\text{fm}^{-3}$.

The values of four parameters have to be determined, and Equation (2.82) requires the input from four finite systems. ^{16}O, ^{40}Ca, ^{56}Ni and ^{100}Sn are chosen. In Figure 2.9, the parameters $(b_s^{(1)})_i$, $(c_s^{(1)})_i$, $(b_v^{(1)})_i$ and $(c_v^{(1)})_i$ are shown at each iteration step of the procedure. They are compared to the parameters of the linear and quadratic term in the Taylor expansion of the DD-PC1 couplings,

$$\varrho_{sat} \left. \frac{d\alpha_{s,v}^{DD-PC1}}{d\varrho_V} \right|_{\varrho_V = \varrho_{sat}} , \tag{2.93}$$

$$\frac{1}{2}\varrho_{sat}^2 \left. \frac{d^2\alpha_{s,v}^{DD-PC1}}{d\varrho_V^2} \right|_{\varrho_V = \varrho_{sat}} . \tag{2.94}$$

Starting from vanishing values, after only a few iterations the parameters of the linear and quadratic couplings of the unknown functional reach values that are very close to the corresponding parameters of the Taylor expansion of the target DD-PC1 couplings. Using the final values of the parameters, the total scalar and vector couplings $\alpha_S(\varrho_V)$ and $\alpha_V(\varrho_V)$ are calculated as functions of the vector density, and compared with the corresponding couplings of the functional DD-PC1 (Figure 2.10). While the couplings of the unknown functional $E_{int}^{(1)}$ have been approximated by simple quadratic functions of the vector density, nevertheless the final scalar and vector couplings accurately reproduce the DD-PC1 target couplings over a broad range of densities.

Finally, in Figure 2.11 the vector densities of the four symmetric systems, $N = Z = 8$, $N = Z = 20$, $N = Z = 28$, and $N = Z = 50$, calculated with the DFPT+IKS method, are compared to the theoretical densities obtained with an RHB calculation that adopts the target functional DD-PC1. Even when the unknown part of the functional is approximated by the simple expressions of Equation (2.92), the DFPT+IKS method produces ground-state densities that are virtually identical to the target densities.
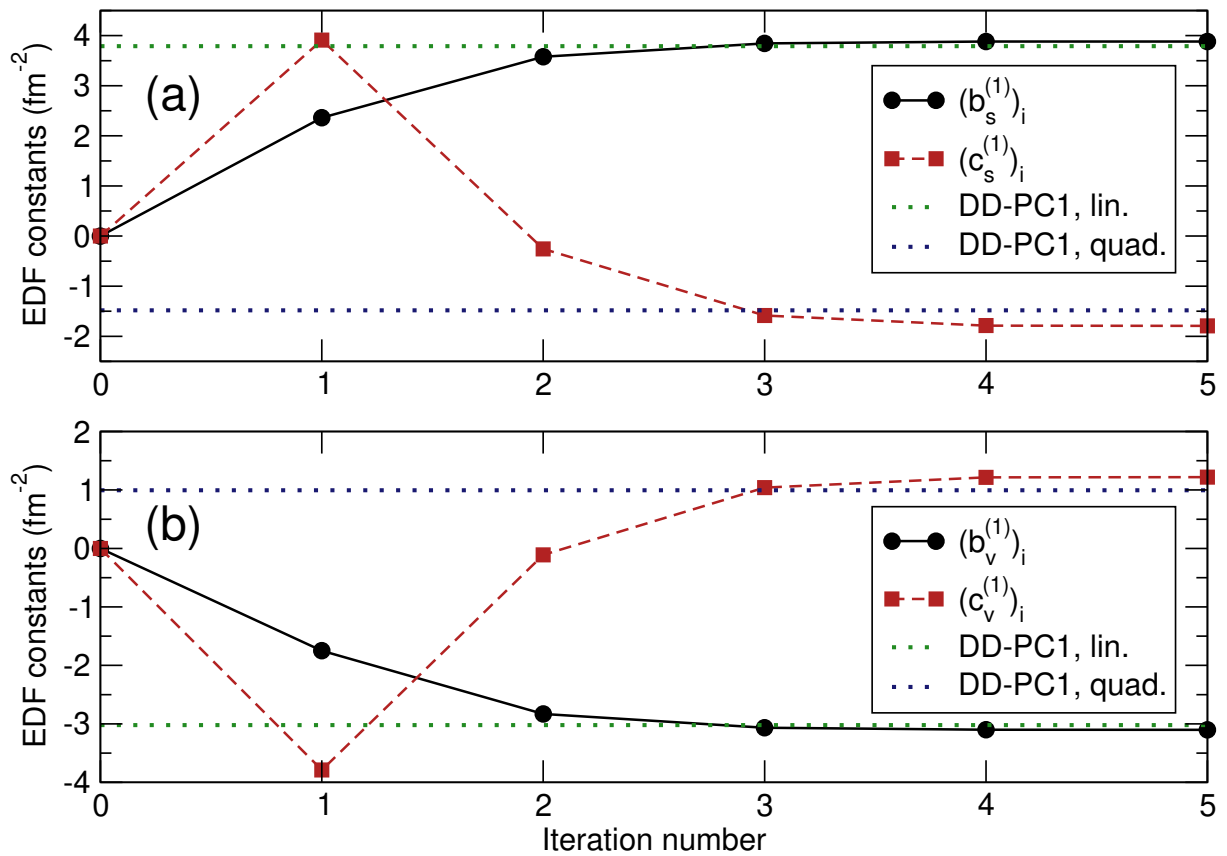
Figure 2.9: Values of the constants $(b_s^{(1)})_i$, $(c_s^{(1)})_i$ (panel (a)), $(b_v^{(1)})_i$ and $(c_v^{(1)})_i$ (panel b) at different iteration steps of the calculation. The dashed lines denote the corresponding parameters of the linear and quadratic term in the Taylor expansion of the DD-PC1 couplings.
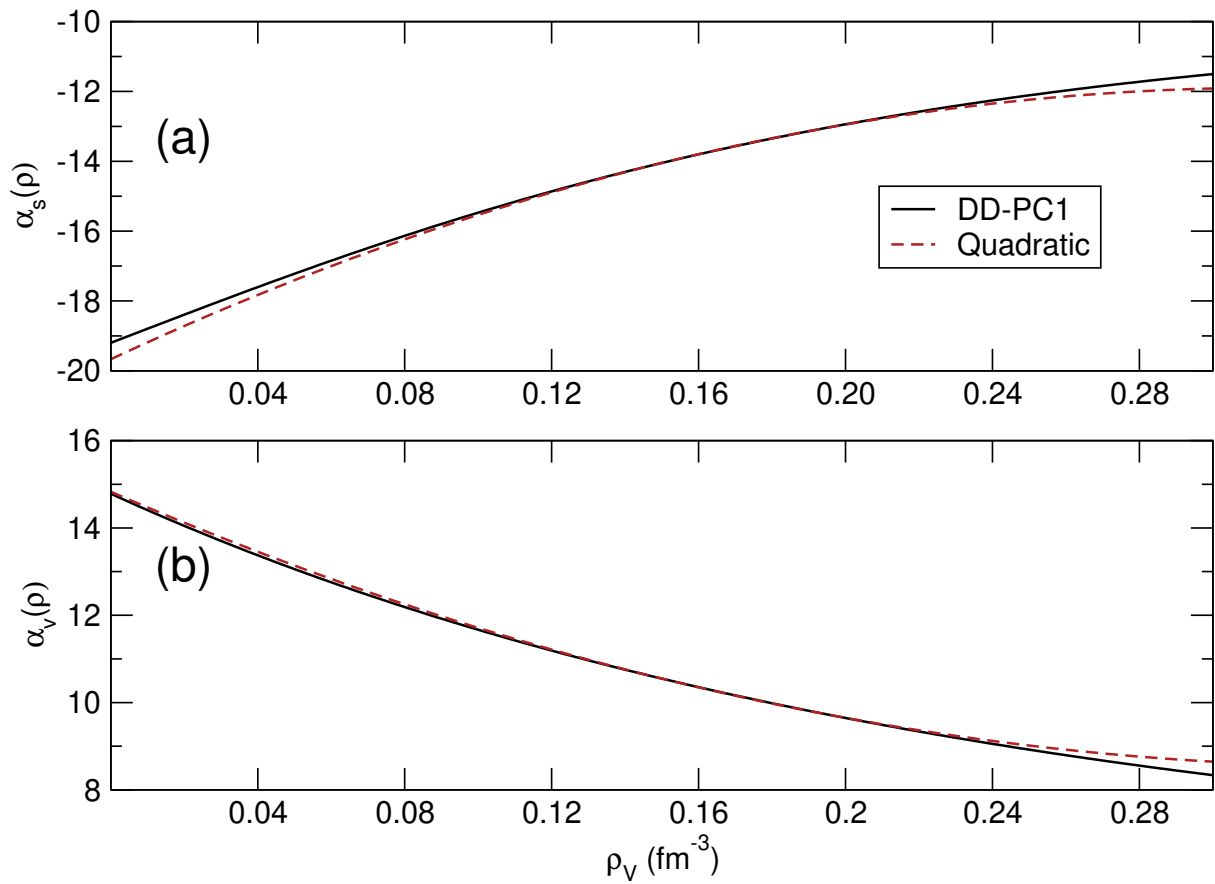
Figure 2.10: Scalar *(a)* and vector *(b)* DFPT+IKS couplings as functions of vector density, compared to the corresponding DD-PC1 target coupling functions.
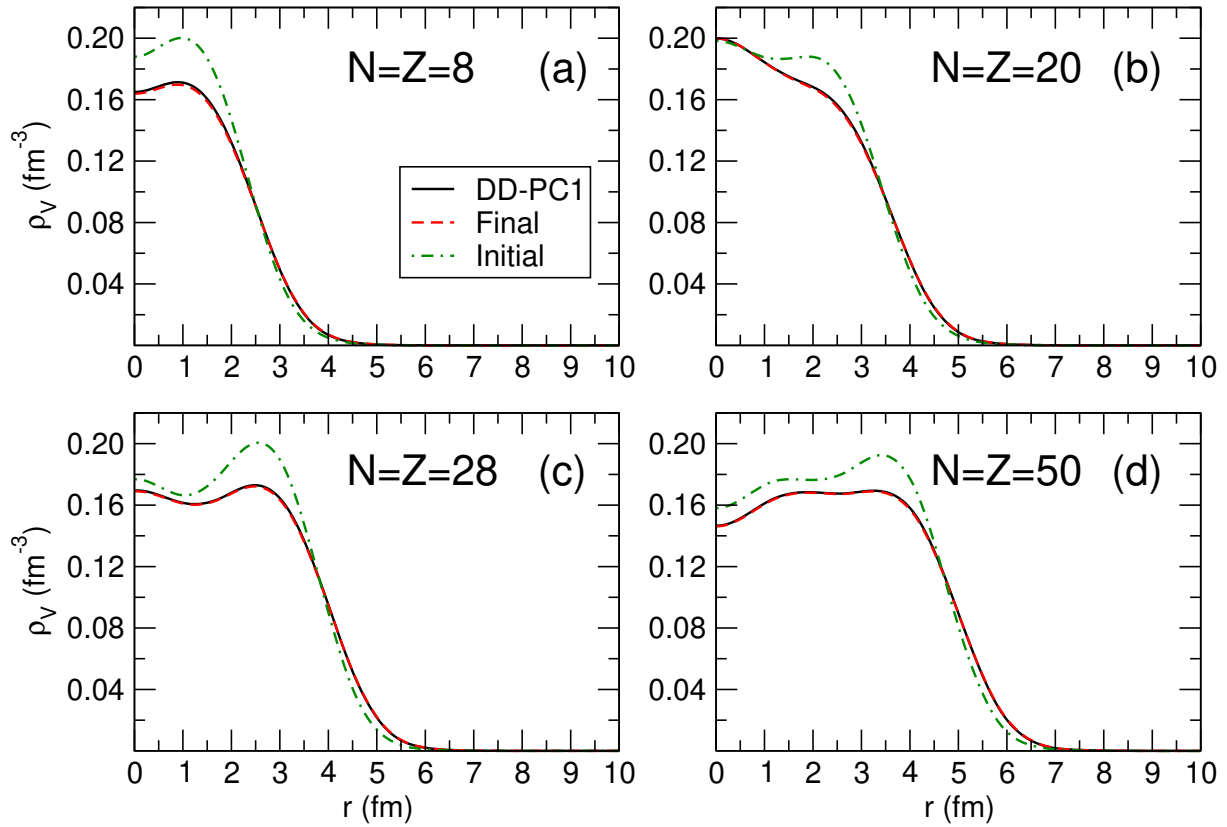
Figure 2.11: The vector densities of the four symmetric systems: $N = Z = 8$, $N = Z = 20$, $N = Z = 28$, and $N = Z = 50$. The dash-dotted green curves are the densities corresponding to the unperturbed initial functional $E_{int}^{(0)}$, Equation (2.87). The solid black and dashed red curves denote the densities obtained with the target functional DD-PC1 and the final results of the DFPT+IKS calculation, respectively.

Chapter 3

STITCHING DISCONTINUITIES ON POTENTIAL ENERGY SURFACES: EFFECT ON NUCLEAR FISSION PROPERTIES

Nuclear fission involves the spontaneous or induced splitting of a heavy atomic nucleus into two or more fragments. It is often accompanied by the prompt emission of neutrons and γ-rays.

Spontaneous fission consists of the non-induced splitting of the nucleus into fragments. It emerges from the competition of the Coulomb forces felt by protons with the nuclear surface tension caused by the attractive forces between nucleons. It occurs therefore in heavy nuclei with a large number of protons, *e.g.*, in the actinide or transactinide region. It is characterized by the fission half-life, namely the time in which half of the nuclei in a sample undergo fission. Spontaneous fission is the main process that limits the formation of super heavy proton-rich elements [86]; in fact, the empirical nuclear fissility parameter [87]

$$ x \approx \frac{Z^2}{A - 1.7826 \frac{(N-Z)^2}{A}} \, , \tag{3.1} $$

which encodes the possibility of a nucleus to undergo fission, grows as the square of the number of protons Z.

Nuclear fission can also be induced by the reaction between a target compound nucleus and incoming light projectiles, such as neutrons, protons, alpha particles, or γ-rays. Induced fission

plays a key role in nucleo-synthesis, especially within the r-process [88], where fission cycling controls the abundances of neutron-rich nuclei [89].

The energy released during one fission event, distributed between the kinetic and the excitation energy of the fragments, is remarkably high (about 200 MeV) especially if compared to other energy sources. The physics behind fission has been applied for more than seventy years to the development of technologies used for energy production. Achieving a deeper theoretical microscopic comprehension of the fission process is thereby crucial to get robust predictions, especially in those nuclear regions where experimental data are not available.

Designing a reliable microscopic framework for the description of fission represents one of the most challenging tasks of modern studies of nuclear physics. Many parameters and quantities, some of them related to nuclear collective degrees of freedom, whereas others characterizing the individual motion of nucleons, play an important role in the process. It is thus complicated to introduce systematic approximations allowing a feasible treatment of the fission process with controllable errors.

At present, most theoretical approaches rely on the adiabatic approximation [90], namely the assumption that the timescale of the collective motion driving the nucleus towards scission is several orders of magnitude larger than the one that characterizes the internal motion of the nucleons. In this case one can consider the the two types of motion as perfectly decoupled. The nuclear many-body problem is then mapped onto a collective Schrödinger-like equation (CSE), governed by only a few collective variables [91].

Albeit being adopted in most applications, some advanced microscopic simulations of the fission process do not support the assumption of adiabaticity for the large amplitude collective motion in fission, especially for trajectories from the outer saddle to the scission configuration [92]. In fact, at this stage of the nuclear deformation, quasiparticle excitations, dissipation, and memory effects [93,94] become decisive for the outcome of the process. However, whether one uses the adiabatic approximation or not, the most promising theoretical framework for a microscopic description of the fission process is based on Density Functional Theory (section 1.3) and nuclear energy density functionals.

During the last decades, several NEDF-based lines of research on the nuclear fission process have been pursued to describe both the spontaneous and the induced fission process. Some of them, often adopting the adiabatic approximation, rely on the time-dependent generator coordinate method (TDGCM) [95]. Others use time-dependent (TD) HF+BCS approaches (sec-

tion 1.2.1 and [96]) or, in a few cases, the full-fledged TDHFB approximation [97]. Each approach presents advantages and drawbacks in determining the dynamical evolution of the compound nucleus. In [98], a successful microscopic DFT-based approach to the calculation of charge and mass of the yields in spontaneous fission has been presented. In [97], a super fluid non-adiabatic extension of TDDFT has been employed to calculate the time-evolution of the nucleus from the last saddle point before scission to the point at which the fragments are well-separated. The Zagreb group, in collaboration with J. Zhao and Z. Li [99,100], used TDGCM to investigate properties of the induced fission of several nuclides at finite-temperature: low-energy bands, octupole deformations, transition rates, charge and mass distributions, and the coupling between collective and pairing degrees of freedom. Further details about the nuclear fission process and state-of-the-art works related to it can be found in the topical reviews [90–92,101,102] and in references cited therein.

3.1   Static And Dynamical Aspects Of Fission

The point at which the fragments that result from fission are physically well-separated is denoted as scission point. Such definition is currently doomed to remain very much related to the intuitive picture of the nucleus provided by the liquid drop model: a progressively deformed nuclear compound winds up in forming a neck that finally ruptures, producing fission fragments. This classical understanding of the process ignores that the wave functions, calculated by solving the SCMF equations, are apt to describe the nucleus as a whole. The single-nucleon wave functions may, and do, spread across the fragments, which in turn become inevitably highly entangled. Unfortunately, if one tries to incorporate these strictly quantum effects within the definition of scission point, several issues stem out, for instance regarding the calculation of the fragment properties [101]; there are nonetheless examples of attempts made in this line of research, *e.g.*, [103, 104]. The scission point is therefore commonly defined in a rather phenomenological way, that involves counting the number of particles in the neck region that separates the nascent fragments. In alternative, it can be defined as the nuclear configuration in which the nuclear interaction energy between the pre-fragments is surpassed by the Coulomb repulsion.

Adiabatic models often rely on pre-calculated potential energy surfaces (PESs) of the parent nucleus, that do not contain any piece of information about fission fragments. Thus, the scission point must be explicitly defined. A physical discontinuity between fission and fusion valleys usually appears to signal the transition of the nucleus to the fission region. In this frame-

work, adopted in this manuscript as well, the specific definition of the scission point is rather ambiguous, since there is no dynamical mechanism to simulate the evolution of the system; semi-empirical definitions must be employed. Thus, if the adiabatic approximation is adopted no unique definition of the scission point is available. The description of the nuclear fission process then presents some sort of dependence on the method used to define it. In contrast, non-adiabatic approaches, *e.g.*, TDHF+BCS and TDHFB, produce scission naturally and continuously, as the system is being time-evolved from a starting state after the last fission barrier.

The solution of the constrained HFB or RHB equations provides, at least in principle, the global minimum energy for a nuclear configuration subject to a number of constrained variables. This enables, given the adoption of the adiabatic approximation, the usage of a chosen set of collective degrees of freedom, commonly but not necessarily related to the geometrical shape of the nucleus, as parameters to navigate potential energy surfaces $E(q_1, \ldots, q_N)$. It is clear then that the availability of numerical routines able to incorporate a relatively large number of constraints in the simulation may play a crucial role. Constraints can be incorporated into the HFB or RHB formalism in the same fashion of the method of the Lagrange Multipliers, for instance through the implementation of the Multiple Constraint method discussed in appendix B.

In a variety of applications, nuclear multipole moments, *e.g.*, quadrupole and octupole, are routinely used as constraints in the SCMF equations. The definition of multipole moments reads:

$$\hat{Q}_{lm} = \sqrt{\frac{1}{1+\delta_{m0}}}(\hat{M}_{lm} + r_m(-1)^m \hat{M}_{l-m}), \tag{3.2}$$

with $r_m = \pm 1$ respectively valid for $m \geq 0$ and $m < 0$, and

$$\hat{M}_{lm} = \sqrt{\frac{16\pi}{2l+1}} r^l \, Y_{lm}(\theta, \phi), \tag{3.3}$$

$Y_{lm}(\theta, \varphi)$ being the spherical harmonics already defined in Equation (1.13). The choice of these collective parameters is justified by the experimental observation of low-energy vibrational modes, that usually display multipole character.

Once PESs are generated by means of a SCMF solver, one can search and find on them static minimum energy paths (MEP) or dynamic, more quantal, least action paths (LAP). These paths, constituting the static ingredients for fission studies, lead nuclei towards scission and are sufficient to calculate some of the properties that characterize the process, such as spontaneous fission half-lives.

Finally, the PES together with the densities and wave functions corresponding to each computed nuclear configuration can be plugged into a time-evolution framework, *e.g.*, TDGCM, to obtain the dynamical quantities of interest, such as mass and charge yields, or the kinetic and excitation energies of the fragments. Since the study of the dynamical aspects of fission goes beyond the scope of the present manuscript, the reader may refer, for instance, to [105], as well as to the reviews cited in the chapter's introduction.

3.1.1 Spontaneous fission lifetime

Spontaneous fission is a remarkable example of the quantum tunneling phenomenon. To undergo spontaneous fission, the parent nucleus must overcome two or three energy barriers before reaching a saddle point after which it becomes unstable against fission. Figure 3.3, depicts the typical topology of a PES associated to a nucleus that may undergo spontaneous fission. The probability that fission happens in competition with other decay modes, or equivalently a measure of the time that it takes for fission to take place, is fundamentally related to the probability of the nucleus to tunnel through the energy barriers that separate the ground-state from highly deformed configurations.

The main quantity that one aims to theoretically estimate while exploring the static aspects of spontaneous fission is the fission lifetime, denoted T_{SF} in this manuscript. Equivalently, the half-life is obtained as $\tau_{\text{SF}}^{1/2} = \ln 2 \, T_{\text{SF}}$. Given the possibility of a direct comparison of the calculated lifetimes with experimental measurements, this quantity has a particular importance in fission studies. Note that, while the implementation of the formalism for its calculation is rather straightforward, the value of the fission lifetime of nuclei ranges between about thirty orders of magnitude [23], making it a sensitive and complicated quantity both to robustly estimate and measure. The fission lifetime is calculated assuming that the nuclear ground-state is stationary, ignoring other open channels through which the nucleus might decay. This assumption is acceptable, because alternative decay modes also proceed through classically forbidden regions characterized by very small transmission coefficients.

Calculation of the action in the WKB approximation

The semi-classical WKB[1] approximation [106, 107] is employed to estimate transmission coefficients, and specifically the penetrability of a nucleus through an energy barrier. In the

---

[1]The Wentzel-Kramers-Brillouin approximation is used to solve linear differential equations by finding approximate solutions with varying coefficients. In quantum physics, the wave function usually takes the form of an exponential function, whose amplitude and phase are assumed to vary slowly.

one-dimensional fully classical case one substitutes the expression of the classical momentum $p = \sqrt{2m(E - V(x))}$ into the equation of motion of a free particle,

$$\frac{d^2\Psi(x)}{dx^2} + \frac{p^2}{\hbar^2}\Psi(x) = 0 . \tag{3.4}$$

A plane wave *Ansatz* is assumed, namely

$$\Psi(x) = A(x)e^{i\varphi(x)} ; \tag{3.5}$$

once this is plugged into Equation (3.4), it leads to the following expression for the amplitude $A(x)$ and the phase $\varphi(x)$:

$$A(x) = \frac{C}{\sqrt{p(x)}} , \tag{3.6}$$

$$\varphi(x) = \pm\frac{1}{\hbar} \int_x^\infty dy \, p(y) . \tag{3.7}$$

The expressions above are valid only in classical regions, where $V(x) \leq E$. They can be nonetheless extended to classically-forbidden regions by introducing a complex momentum $p(x)$; Equation (3.5) transforms into an exponential, and yields the following expression for the solution $\Psi(x)$ at $V(x) > E$:

$$\Psi(x) = \frac{C_\pm}{\sqrt{p(x)}}\exp\left[\pm\frac{1}{\hbar} \int_x^\infty dx \, \sqrt{2m(V(x) - E)}\right] . \tag{3.8}$$

The non-physical solution with positive sign is discarded. The resulting penetrability coefficient reads

$$P = \frac{|\Psi(b)|^2}{|\Psi(a)|^2} = \exp\left[-\frac{2}{\hbar} \int_a^b dx \, \sqrt{2m(V(x) - E)}\right] , \tag{3.9}$$

where a and b are the inner and outer turning points at the barrier, corresponding to the energies $V(a) = E$ and $V(b) = E$ that make the integrand vanish.

The extension of these concepts to the study of the nuclear fission process is justified by the assumption of adiabaticity of the collective nuclear motion, which enables using a restricted number of variables to govern the CSE. The effective collective inertia tensor $B[s]$, calculated along the fission path, and the constrained SCMF total energy replace, respectively, the mass of the particle and the potential energy in Equation (3.9). In most advanced applications, the

nuclear path along which the fission lifetime is calculated is the LAP, that minimize the action

$$S[s] = \int_a^b ds \ \sqrt{2B[s](V_{\text{eff}}(s) - E_0)} \ , \tag{3.10}$$

that appears in the exponent of (3.9). It is worth noticing, as it will be discussed in more detail in section 3.6, that it is also possible to justify a calculation of the action on static minimum energy paths. In the previous expression $V_{\text{eff}}(s)$ is the total collective energy of the nucleus with respect to the ground-state, minus the spurious zero-point energy $E_{\text{ZPE}}(Q_{20})$. E_0 is a ground-state zero-point energy correction. Some applications, such as [108, 109], take $E_0 = 1$ MeV. Others [110] fine-tune it accordingly to the quadrupole deformation of the nucleus in its ground-state, $E_0 = 0.7 \ E_{\text{ZPE}}(Q_{20}^{\text{g.s.}})$. $E_{\text{ZPE}}(Q_{20})$ is obtained using the Gaussian overlap approximation [111], as shown in [112, 113].

Finally, albeit not employed in this work, one should mention that more advanced techniques have been proposed in the literature [114] for the calculation of the transmission coefficient P across a double-hump barrier with two closely-situated classical turning points.

Calculation of the nuclear collective inertia

In adiabatic models the nuclear collective inertia can be seen as the mass of the collective wave-packet, as it incorporates the response of the nucleus to small variations of the constrained collective variables $q_i(s)$. It can be calculated along the fission path in the following way:

$$B(s) = \sum_{ij} M_{ij} \frac{dq_i}{ds} \frac{dq_j}{ds} \ , \tag{3.11}$$

where s parameterizes the path, while M_{ij} is the collective inertia tensor. The collective inertia tensor appearing in the previous equation can be calculated by means of the Generator Coordinate Method (GCM) [115] or within the adiabatic time-dependent Hartree-Fock-Bogoliubov (ATDHFB) approximation [116]. A direct comparison of the results with the two approaches can be found in [117]. The GCM approach unfortunately leads to a systematic underestimation of the collective inertia [91]. As a consequence, this work adopted the ATDHFB formalism.

The ATDHFB approximation consists of a small-momentum expansion of the full time-dependent generalized density of TDHFB equation of motion, Equation (1.33). The expansion

of the generalized density is performed through the unitary transformation

$$\mathcal{R}(t) = e^{-i\chi(t)}\mathcal{R}_0(t)e^{i\chi(t)} \ . \tag{3.12}$$

By expanding the TDHFB equation of motion up to the second order in the parameter $\chi(t)$, one obtains a collective Schrödinger equation. The time-dependence of the generalized density $\mathcal{R}_0(t)$ is mapped onto the collective space spanned by a set of variables $q_i(t)$,

$$\frac{\partial \mathcal{R}_0(t)}{\partial t} = \sum_i \frac{\partial \mathcal{R}_0}{\partial q_i}\frac{\partial q_i}{\partial t} \ . \tag{3.13}$$

The kinetic energy then becomes

$$\mathcal{K} = \frac{1}{2}\sum_{ij} M_{ij}\frac{dq_i}{dt}\frac{dq_j}{dt}, \tag{3.14}$$

and the collective inertia tensor takes the form

$$M_{ij} = \frac{\partial \mathcal{R}_0}{\partial q_i}\mathcal{M}^{-1}\frac{\partial \mathcal{R}_0}{\partial q_i}. \tag{3.15}$$

The inversion of the linear response matrix $\mathcal{M}$ relies on the assumption of the perturbative cranking approximation, in the same fashion of the derivation presented in appendix B. A diagonal approximation of the matrix is assumed, with two quasiparticle energies as diagonal elements. The partial derivatives of the generalized matrix are obtained in a similar way, by applying the cranking approximation to them as well. This results [116] in the ATDHFB approximation of the collective inertia that enters Equation (3.11):

$$M \approx M_{\text{ATDHFB}} = \hbar^2 [\mathtt{M}^{(-1)}]^{-1}\mathtt{M}^{-3}[\mathtt{M}^{(-1)}]^{-1} \ , \tag{3.16}$$

$$\mathtt{M}^{(-n)}_{ij} = \sum_{\mu<\nu}\frac{\langle\Phi|\,\hat{Q}_i^\dagger\,|\mu\nu\rangle\,\langle\mu\nu|\,\hat{Q}_j\,|\Phi\rangle}{(E_\mu + E_\nu)^n} \ . \tag{3.17}$$

The state $|\Phi\rangle$ is the quasiparticle vacuum already defined in (1.27), while $|\mu\nu\rangle = \beta_\mu^\dagger\beta_\nu^\dagger\,|\Phi\rangle$ is a two-quasiparticle excitation built on top of it. Such classical approximation neglects the presence of a zero-point energy correction to the collective potential; nonetheless, several authors suggested to use it anyway in its GCM form [110, 118, 119].

Calculation of the fission lifetime

Provided the condition $S \gg \hbar$, which in fact must hold to justify the application of the WKB approximation itself, the fission lifetime is inversely proportional to the transmission coefficient of Equation (3.9), according to the relation [120]

$$T_{\text{SF}} = 1/\nu P \; ; \tag{3.18}$$

The proportionality coefficient $\nu = 10^{20.38}$ s^{-1} is the number of assaults of the nucleus to the fission barrier per time unit, calculated for a system vibration that leads to fission equal to $\hbar \omega = 1$ MeV [121]. With these premises, the spontaneous fission lifetime reads

$$T_{\text{SF}}[s] = \frac{1}{\nu} \exp \left[\frac{2S[s]}{\hbar} \right] , \tag{3.19}$$

where the action $S[s]$ is defined by Equation (3.10).

3.2 Appearance Of Discontinuities On Self-Consistent Potential Energy Surfaces

An important drawback characterizes fission simulations that adopt the adiabatic approximation: the factual necessity to limit, due to computational resources, the number of constrained collective variables to a small, finite set. All other unconstrained variables are instead determined self-consistently, adjusted by the solver of the mean-field equations to seek the global minimum of the underlying unconstrained PES. Since it is not guaranteed for the unconstrained variables to evolve continuously, a key problem emerges in relation to saddle points, which might be missing on an equivalent trajectory restricted to a smaller dimension, or might not be real saddle points on the same PES with additional dimensions. These two types of problematic saddle points are respectively called missing and fake saddle points.

The mentioned issues with saddle points, discussed in great detail in [122], are in fact caused by the presence of an artificial discontinuity on the investigated potential energy surface. A discontinuity may appear because of two reasons:

1. In practical calculations, different starting guesses for the single-nucleon wave functions might lead the iterative process to converge to different results. Because of this, hysteresis-like fission paths might be found.

2. A sudden, discontinuous, non-physical jump of the nucleus from one configuration to another may happen. For instance, when one only constraints the mass quadrupole moment, the nucleus may jump from a symmetric configuration to one characterized by non-vanishing octupole deformation, disregarding the complex topology of the ridge that divides them.

While the first type of scenario, connected to the specific implementation of the solver's numerical routine, can be ideally avoided by carefully selecting an appropriate *Ansatz* for the single-nucleon wave functions, the second type of discontinuity is intrinsically related to the adopted theoretical framework.

Figures 3.3 and 3.6 illustrate a typical example of the latter type of discontinuity. The solver, constrained to produce a desired value of the quadrupole moment, finds successive local minima in the symmetric valley, where the nucleus is reflection-symmetric. At a certain point, during the progressive adiabatic deformation of the nucleus, the routine, which is in general allowed to break parity, winds up exploring an asymmetric valley. Within this set of pear-shaped configurations with non-vanishing octupole moment, states that are energetically more advantageous are found. In fact, the code have lingered too long in one of the valleys, finding there successive local minima but ignoring the real global minima actually present on the other side of the ridge, at the same quadrupole deformation but at different octupole deformations.

The problem is delicate, especially considering that a discontinuity might not even appear visible to the eye in the plot of the total binding energy of the deforming nucleus. This of course happens if two energy valleys are very close in energy. An example of this is shown in the first discontinuity of Figure 3.5, not clearly noticeable from the energy plot of Figure 3.3.

A discontinuity on the fission path precludes the correct calculation of physical properties of fission, for example by hiding the real height of an energy barrier. At this point, one must deal with two different but strictly connected tasks:

- A way to quantitatively assess the quality of a calculated PES must be found.

- Methods and routines to stitch discontinuities must be researched.

These are the main subjects of the second part of this doctoral work, and are discussed in the upcoming sections.

3.3 Assessment Of The Presence Of A Discontinuity On A Potential Energy Surface

The presence of a discontinuity can be quantified by computing the density distance or the norm overlap between adjacent points on the PES. In particular, consider the densities ϱ_0, ϱ_1, and the wave functions $|\varphi_0\rangle$, $|\varphi_1\rangle$, associated with the pair of points $\vec{q}_0$ and $\vec{q}_1$ on a given PES. A discontinuity is identified if the quantities

$$\mathcal{D}_{\varrho_0 \varrho_1} = \int d^3 r \, |\varrho_0(\vec{r}) - \varrho_1(\vec{r})| \,, \tag{3.20}$$

$$\mathcal{N}_{01} = \langle \varphi_0 | \varphi_1 \rangle \,, \tag{3.21}$$

are, respectively, large and far below the unit.

The calculation of the latter quantity certainly demands larger computational resources than those required by the former. In fact, the norm overlap is obtained from the HFB or RHB amplitudes U_i and V_i ($i = 0, 1$) of the two states by following the procedure described in the next subsection. The U_i and V_i matrices are calculated in terms of a chosen basis, such as the harmonic, possibly deformed, oscillator basis. In contrast, the computation of the density distance only makes use of two nuclear densities defined on top of a discretized coordinate space. The computation of Equation (3.20) thus requires the calculation of a rather simple integral in the coordinate space. On the other hand, the estimation of norm overlaps can easily become cumbersome, technically and computationally. In the case of heavy nuclei, a robust expansion of the nuclear total wave function may require the usage of harmonic oscillator bases with up about thirty major shells, corresponding to several thousands of states. Thus, it may involve the construction and multiplication of extremely large matrices, precise ordering of their states, calculation of determinants; smart implementations to keep memory usage and computational time under control become fundamental.

For these reasons, several authors, such as [122–124], decided to stick to the usage of density distances to establish the quality of potential energy surfaces. Nonetheless, the norm overlap (3.21) is a superior indicator, able to detect discontinuities stemming from a wider range of sources, such as those related to the pairing properties. In addition, one should always factor out the artificial contribution brought by the specific discretization of the PES. The norm overlap performs better also from this point of view. Accordingly to the calculations carried out

in this work, when a PES is continuous, the norm overlap takes values between 1 and about 0.5, while a discontinuity is characterized by values that are many orders of magnitude smaller, often down to 10^{-7}. Figure 3.4 confirms this. On the other hand, the density distance may take values between 0 and 10 for a continuous PES, and between 15 and 50 in presence of a discontinuity. It is then clear that choosing a critical value for $\mathcal{D}^{\mathrm{max}}$, above which the PES should be considered discontinuous, is more complicated than making a analogue choice for $\mathcal{N}^{\mathrm{min}}$. Finally, considering that the calculation of norm overlaps (3.21) is a crucial step of the model presented in section 3.4.1, in this work it was decided to implement the most robust formalism available for it on the market.

3.3.1 Calculation of norm overlaps

The calculation of the overlap of an operator O between two different many-body states $|\phi_0\rangle$ and $|\phi_1\rangle$,

$$\langle \phi_0 \,|\, O \,|\, \phi_1 \rangle, \tag{3.22}$$

is an operation that one commonly encounters, *e.g.*, in calculations based on GCM or in symmetry restoration. In the case of this manuscript, the operator is $\hat{O} = \hat{\mathbb{1}}$, since one would like to obtain the norm overlap among two adjacent states on a PES, expressed by Equation (3.21). A thorough calculation of Equation (3.22) can become a complicated task, depending on the specifics of the two states and of the bases in which they are expanded.

If the two states $|\phi_0\rangle$ and $|\phi_1\rangle$ are built via an expansion on a common spherical basis, as it may be the one formed by the eigenfunctions of a spherical harmonic oscillator potential, the well-known Onishi formula [125, 126] or the equivalent [127] Pfaffian formula [128] can be safely adopted. However, simulations of the fission process are characterized by the progressive deformation of the nucleus, which explores wildly different shapes. Thus, smart optimizations and reductions of the bases are unavoidable in order to keep numerical resources under control.

A first type of basis optimization, in which one assumes that the nucleus under investigation is axially symmetric, consists in expanding the single-nucleon wave functions in the basis of a deformed harmonic oscillator potential,

$$U(z, r_\perp) = \frac{1}{2} m (\omega_z^2 z^2 + \omega_\perp^2 r^2) \,. \tag{3.23}$$

When this expression is compared to the spherical harmonic oscillator potential (1.16), the

imposition of volume conservation entails $\omega_0^3 = \omega_z \omega_\perp^2$, and the two frequencies $\hbar\omega_z$ and $\hbar\omega_\perp$ can then be defined in terms of a deformation parameter β_0:

$$
\begin{aligned}
\hbar\omega_z &= \hbar\omega_0 e^{-\sqrt{\frac{5}{4\pi}}\beta_0} \ , \\
\hbar\omega_\perp &= \hbar\omega_0 e^{\sqrt{\frac{5}{16\pi}}\beta_0} \ .
\end{aligned}
\tag{3.24}
$$

The corresponding cylindrical oscillator lengths are defined by

$$
\begin{aligned}
b_z &= \sqrt{\frac{\hbar}{m\omega_z}} \ , \\
b_\perp &= \sqrt{\frac{\hbar}{m\omega_\perp}} \ ,
\end{aligned}
\tag{3.25}
$$

and the basis is thus uniquely determined by the two constants $\hbar\omega_0$ and β_0. The eigenfunctions of the cylindrical harmonic oscillator (3.23),

$$
\Phi_\alpha(\vec{r}, s) = \varphi_{n_z}(z, b_z)\varphi_{n_\perp, m_l}(r, b_\perp)\frac{e^{im_l\phi}}{\sqrt{2\pi}}\chi(s) \ ,
\tag{3.26}
$$

are composed of the product of a one-dimensional axial wave function and a two-dimensional radial wave function, that respectively read

$$
\varphi_{n_z}(z, b_z) = b_z^{-\frac{1}{2}}\phi_{n_z}(\xi) = b_z^{-\frac{1}{2}}N_{n_z}H_{n_z}(\xi)e^{-\frac{\xi^2}{2}} \ ,
\tag{3.27}
$$

$$
\varphi_{n_\perp, m_l}(r, b_\perp) = b_\perp^{-1}\phi_{n_\perp, m_l}(\eta) = b_\perp^{-1}N_{n_\perp, m_l}L_{n_\perp}^{|m_l|}(\eta)\sqrt{2}\eta^{|m_l|/2}e^{-\eta^2} \ ,
\tag{3.28}
$$

where $\xi = z/b_z$, $\eta = r^2/b_\perp^2$, $N_{n_z} = (\sqrt{\pi}2^{n_z}n_z!)^{-1/2}$ and $N_{n_\perp, m_l} = (n_\perp!/(n_\perp + |m_l|)!)^{1/2}$, while $H_{n_z}(\xi)$ and $L_{n_\perp}^{|m_l|}(\eta)$ are the Hermite and the associated Laguerre polynomials.

If the bases in which the states $|\phi_0\rangle$ and $|\phi_1\rangle$ are expanded are characterized by non-vanishing deformation parameters, they are not closed under rotations, and the Wick's theorem cannot be applied in its original formulation [129]; In [130], an extension of the Wick's theorem was proposed that enables the calculation of overlaps between states expanded in bases that are not closed under the canonical transformation relating them. This formalism has been implemented for the first time only recently, in the latest version of the HFB solver HFBTHO [40, 131]. Here, the formula for the calculation of the overlaps has been used to restore the angular momentum of HFB states, considering the specific case in which the state $|\phi_1\rangle$ is a rotation of the state $|\phi_0\rangle$. However, this implementation still does not represent the most general application of the

framework, since the two states are expanded in the same, albeit deformed, bases.

As already mentioned, state-of-the-art routines for fission simulations optimize the harmonic oscillator basis deformation for each configuration. In the calculation of a PES, which is the first step of many fission simulations based on the SCMF framework, the oscillator lengths b_z and $b_\perp$ are separately optimized for each HFB state, to mimic the nuclear quadrupole deformation associated to it. Figure 3.1 illustrates this: the increased deformation of the basis tightly follows the progressive deformation of the nucleus. This entails growing deformation parameters and axial oscillator lengths that increase linearly. In contrast, the radial component of the oscillator lengths remains roughly constant on the same interval.

The size of each basis is often reduced: an energy cut-off mechanism limits the number of harmonic oscillator levels that are actually considered. Thus, one would like to be able to calculate overlaps between states built on the most general bases, characterized by different number of states, oscillator lengths and deformations. Only very recently, the formalism presented in [132, 133] enabled this possibility, by far the best and most useful option in the case of the study of the nuclear fission process. Other than the tests of the formalism that accompanied its publication, no other attempt to implement it has been yet done. This formalism, whose salient features are exposed in appendix C, has been adopted, implemented and tested in this manuscript. For the first time, it was applied to calculate overlaps between states expanded in bases with different dimensions.

The basic feature of the adopted formalism for the calculation of the overlaps consists in accounting for the effect of the most generic unitary transformation that connects the two bases used for the expansion of the single-nucleon wave functions. The more distant and different are the two states, and consequently the bases optimized for their description, the more the overlap will diverge from the one calculated with the traditional formulas, possibly arriving to differ few orders of magnitudes.

In general, trying to apply traditional formulas, *e.g.*, Equation (C.10), for the calculation of overlaps between states corresponding to different configurations and built in different bases, over-estimates the correct results that are be obtained with Equation (C.18). Regarding the assessment of discontinuities, this means that the condition for a PES to be continuous becomes more stringent. This feature is visible is Figure 3.4.
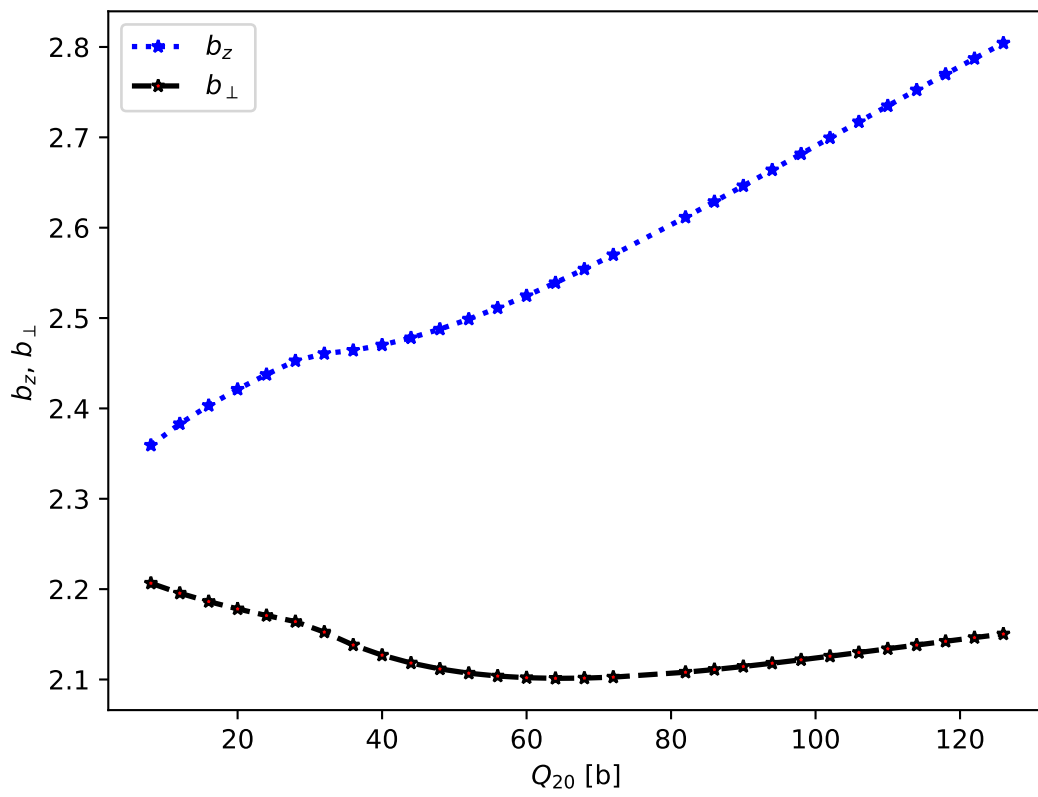
Figure 3.1: The evolution of the axial and radial oscillator lengths of the deformed harmonic oscillator basis in a typical fission simulation.

3.4 Methods For Stitching Discontinuities

A first naive solution to smooth a fission path is to brute-force recalculate the PES including the degree of freedom in which a discontinuity appeared. Unfortunately, computational resources generally hinder the further addition of collective variables.

In [134, 135], an alternative set of geometrical collective variables, not based on mass multipole moments, have been adopted. The goal here is to address the inadequacy of a few multipole moments to describe highly deformed nuclear shapes, specifically from the last saddle to the scission point. Two sides of the nucleus can be defined with respect to a plane $z = z_0$. Then, in place of the quadrupole moment, the distance between the centers of mass of the two sides of the nucleus can be used. Of course, the idea is that, at the end of the process, these will coincide with the centers of mass of the fragments. The octupole moment can be replaced by the mass difference between the sides of the nucleus. The hexadecupole moment, apt to describe deformations that lead to the formation of a neck that separates the two nascent fragments, can be substituted with a neck operator. This accounts for the density or for the number of particles inside the neck region. These operators are indeed more adequate to describe highly deformed configurations and pre-fragments. The idea of a hybrid description based on multipole moments at low-deformations and other collective variables elsewhere is intriguing. However, this approach must deal with the introduction of new parameters in the model. Moreover, the discrete substructure of nuclei makes the above definition of sides of a nucleus, or that of the neck region, rather ambiguous.

3.4.1 DPM-DK routine

The present section discusses an alternative approach to the two mentioned above to solve a discontinuity that appears on a PES. The numerical routine developed here is to be thought of as an add-on to the HFBTHO solver [40], whence it takes as inputs the nuclear PES, together with its corresponding densities and wave functions. It is nonetheless straightforward to readopt the implementation to any other HFB or RHB solver.

The routine, from here on denoted as DPM-DK, aims to quantify and efficiently stitch discontinuities that may appear on a nuclear PES. The idea is to patch the discontinuity with a relatively small higher-dimension PES, and to find a new smooth minimum energy path across it. Unlike the original work of [136], the robust calculation of the overlaps expressed by Equation (C.18) and presented in appendix C has been implemented. The ability to calculate reliable

overlaps is crucial for the stitching procedure, since these quantities are employed to quantitatively establish the smoothness of the path.

In order to quantify the actual usefulness of the software and its applicability to realistic applications, fission lifetimes have been calculated along the smoothed MEPs, and compared to reference values available in the literature. The calculation also has the goal of verifying that the procedure does not have any negative impact on nuclear fission properties. Following the presentation of the DPM-DK routine, some illustrative applications are discussed, together with the results obtained calculating the fission lifetimes along smoothed paths.

The presence of a discontinuity on an input 1D-PES is established by calculating the norm overlaps (3.21) between adjacent points. Afterwards, a 2D-PES that includes the degrees of freedom in which the discontinuity was found is generated to patch it. The HFBTHO program has been employed to this purpose. It is worth pointing out that the generated PES should be neither too large nor too small. It is evident that a big patching two-dimensional PES would go against the philosophy of the model, intended as a cheaper alternative to other options. On the other hand, a patching PES that is too small would graft a model-dependency in the search of the MEP, forcing it to pass across a narrow set of collective variables arbitrarily picked by the user.

The Dynamic Programming Method (DPM) [137, 138], inspired to a breadth-first search (BFS) algorithm [139], has been implemented on the mesh that discretizes the patching two-dimensional PES with the purpose of finding a smooth minimum energy path across it. It improves the BFS algorithm in the sense that it calculates only a limited number of paths at each step of the search, thus taming exponential memory and time requirements. In fact, the main drawback of the BFS algorithm is its memory and time cost, growing exponentially with the size of the search space. During its search, a BFS algorithm stores all the M^N paths generated between the source and the solution node. The DPM algorithm has demonstrated a great efficiency thanks to its many applications to the search of least action paths, commonly employed to calculate spontaneous fission lifetimes. For instance, in [140], a few grid-based methods used for the search of LAPs across PESs have been compared to a method based on the solution of the Euler-Lagrange equations and to a new model, called Nudged Elastic Band (NEB) method, in which the LAP is found by continuously shifting the pathway to the closest minimum action path. In this comparison, the DPM algorithm came out as a top performer; it was even used to initiate the presented NEB method, which, given its higher complexity, produces of course

slightly lower action integrals.

The minimum energy path is computed in the DPM-DK routine by thinking the patching two-dimensional PES as a tree-data structure, with an horizontal size of N points, and a vertical size of M points. The search starts from an initial source node, chosen by the user among the points of the input discontinuous PES, with coordinates (x_I, y_I). The variable x denotes the collective variable describing the input one-dimentional PES, while y is the second degree of freedom that constitutes the patching two-dimensional PES. A BFS algorithm would explore all the nodes of the MN-sized patching PES at each depth, that is at a given quadrupole deformation, before moving on to the nodes of the successive depth level. A queue would be built to keep track of the nodes that have been visited but not yet explored. The BFS algorithm is guaranteed to find the solution node, if it exists. In the present case, the solution node is another user-chosen point of the input PES, denoted by the coordinates (x_F, y_F). At the end of the search, all the paths are compared, and the one characterized by the smallest value of the path-integrated energy,

$$E[\mathcal{P}] = \sum_{i=1}^{N} E(x_i, y_i) \, , \tag{3.29}$$

is selected as the minimum energy path.

Here, an example of pseudo-code that implements the BFS algorithm is shown:

```
1        Q = [] is an empty queue
2        The source node 'source' is labeled as explored.
3        Q.append('source')
4        if Q is not empty, pop out its first element
5            v = Q.pop[0]
6            if the node v is the solution, return v
7            else
8                for all edges [v,w] starting from v
9                        if w is not labeled as explored then
10                               label w as explored
11                               Q.append(w)
```

The DPM, implemented in the DPM-DK routine, tries to deal with the exponential requirements of the BFS algorithm by limiting the amount of stored paths. Specifically, at each depth level of the search, all the paths $\mathcal{P}$ that wind up in a same successive intermediate node k are compared by calculating their path energy,

$$E_k[\mathcal{P}] = \sum_{i=1}^{N_k} E(x_i, y_i) \, , \tag{3.30}$$
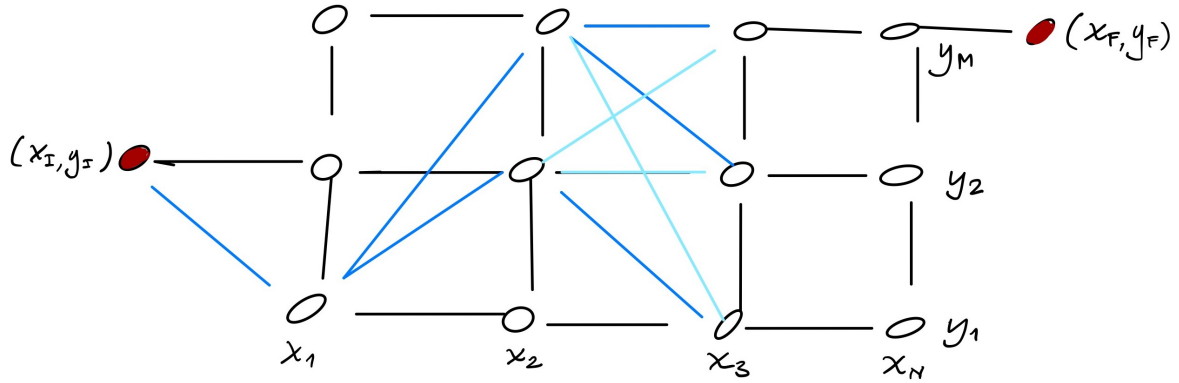
Figure 3.2: At each step of the DPM search all the successor paths are calculated (light blue segments). Among multiple paths that share the same tip, only the one with the least integrated energy, Equation (3.30), is not discarded (blue segments). At the end of the algorithm, the path with the minimum integrated energy (3.29) is selected among the stored candidates.

where $E(x_i, y_i)$ is the energy associated to the point (x_i, y_i) of the patching PES. All non-minimal paths are discarded, reducing the final number of stored paths to MN. The procedure is sketched in Figure 3.2. At the code level, this means that before proceeding to the successive depth level, that is when the queue of the pseudo-code 3.4.1 is emptied, a number of edges are removed from the structure in which they were stored. When the solution node is found, the number of paths to be compared is therefore sensitively reduced.

The additional requirement of a minimum norm overlap between neighboring connecting points, and that of a maximum acceptable gradient of the path, can be added. Of course, while these conditions favor the smoothness of the final path, they relax the adiabatic hypothesis. The path calculated by DPM-DK is not guaranteed to pass from local minima of the PES, as long as the total energy integrated on the path, Equation (3.29), is minimized. Moreover, these requirements limit the space spanned by the algorithm, disrupting the warranty of existence of a solution. In the present work, the maximum number of vertical steps between each segment of the path has been set to $\Delta_{\max} = 1$, while the minimum requested norm overlap, effectively used to establish the continuity of a PES, has been set equal to $\mathcal{N}_{\min} = 0.3$. The setting $\Delta_{\max} = 2$ was also investigated, but it was noticed that this condition would produce the same solution as $\Delta_{\max} = 1$ for equal $\mathcal{N}_{\min}$, since most of the additionally considered paths were not continuous.

3.5 Tests Of The DPM-DK Routine

^{252}**Cf**

The DPM-DK routine has been first applied to the one-dimensional PES of ^{252}Cf, constrained by the quadrupole moment. The PES[2] is shown in Figure 3.3 as a blue dotted line. The calculation of adjacent norm overlaps, Figure 3.4, reveals the presence of two discontinuities: one at $Q_{20} = 60$ b in the hexadecupole moment, Figure 3.5, and the other at $Q_{20} = 172$ b in the octupole moment, Figure 3.6. The latter discontinuity is a clear example of the above mentioned issue related to self-consistent based calculation of PES. A sharp non-physical transition from the symmetric to the asymmetric valley is present in the original path. The HFB solver ignored the presence of a set of lower-lying energy minima across the ridge that divides the two valleys. Because of this, the height of the second barrier is increased. Two patching PESs are generated, defined by $Q_{20} = (40, 72)$ b, $Q_{40} = (3.2, 10.4)$ b^2 and $Q_{20} = (128, 192)$ b, $Q_{30} = (0, 16)$ b$^{\frac{3}{2}}$. The DPM-DK routine produces new smooth MEPs, as the discontinuities get stitched one by one (Figure 3.3, dashed red and solid black lines). The evolution of the third and fourth multipole moments are as well visibly smoother at the end procedure, see Figures 3.6 and 3.5. The obtained minimum energy path reflects the complexity of the ridge that divides the symmetric and asymmetric valleys, showing the structured climb of the nucleus across it. Needless to say, due to the fact that a connecting point is added to the stitching path only if it satisfies the conditions of a minimum overlap $\mathcal{N}^{\min}$ with its neighbors, the obtained path is continuous by definition.

As mentioned above, the stitching path differs from the adiabatic path that one would obtain on a fully two-dimensional PES. This adiabatic path, locally crossing points of minimum energy, may on the other hand remain discontinuous even after increasing the dimension of the PES, due to the specific discretization of the PES. Even if, locally, each point of the DPM-DK path is not minimal as the condition of adiabaticity is relaxed, globally this is the path characterized by the smallest integrated energy, Equation (3.29).

---

[2]The PESs of ^{252}Cf have been calculated using HFBTHO. The D1S Gogny interaction has been adopted. The calculations used 30 major shells for the HO basis in which the single-nucleon states were expanded. The calculation considered a reduction of the basis corresponding to 1700 states, while the basis deformation has been optimized as a function of the nuclear deformation.
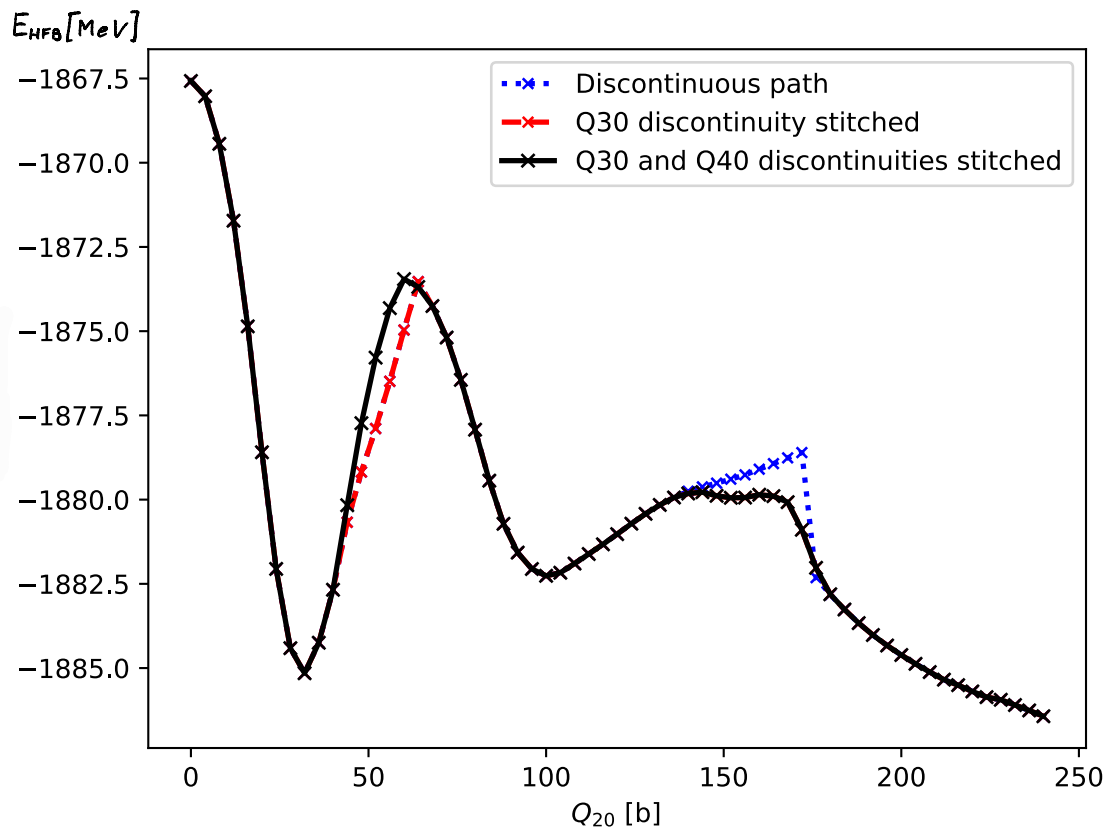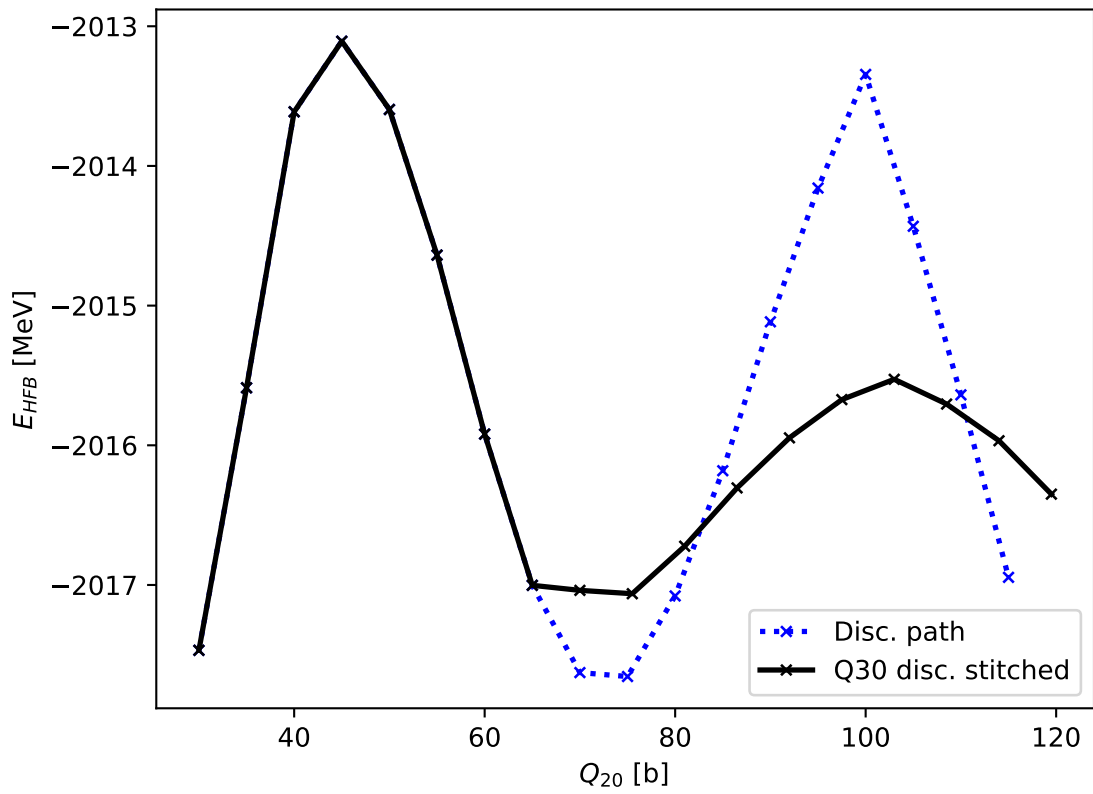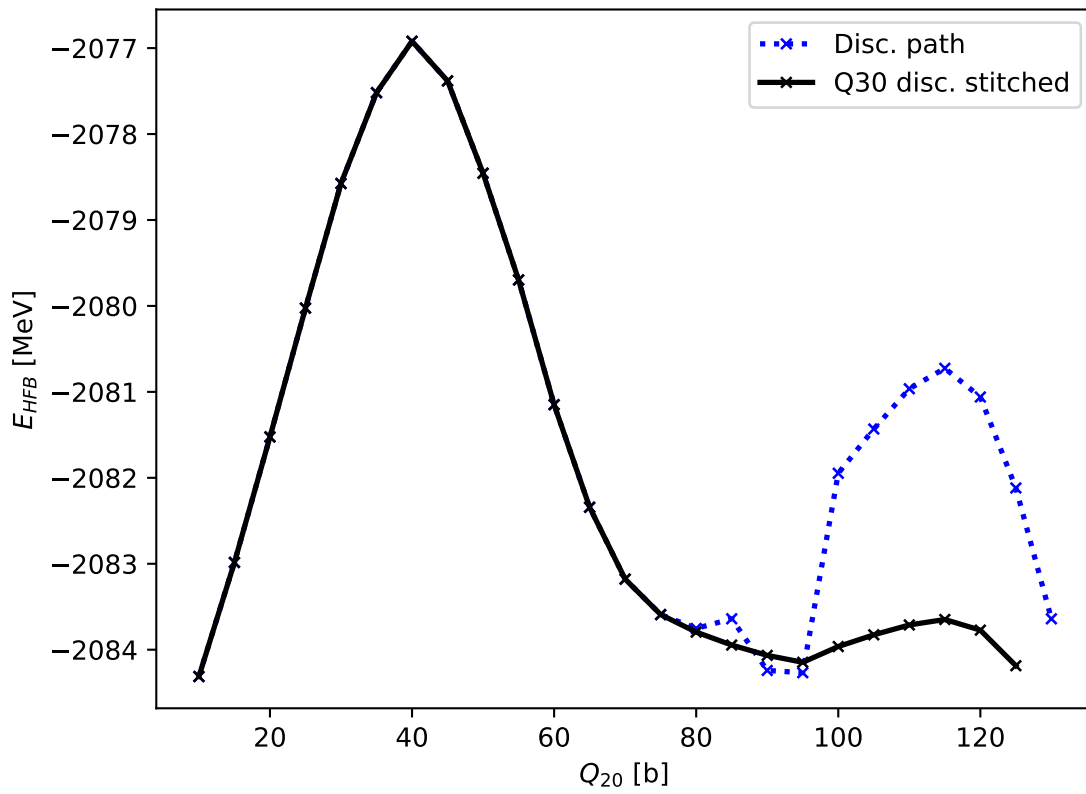
Figure 3.3: The potential energy surface of ^{252}Cf. The dotted blue line is the original, discontinuous, PES. The dashed red line is the PES obtained after stitching the octupole moment discontinuity, while the black solid line is the final DPM-DK path.
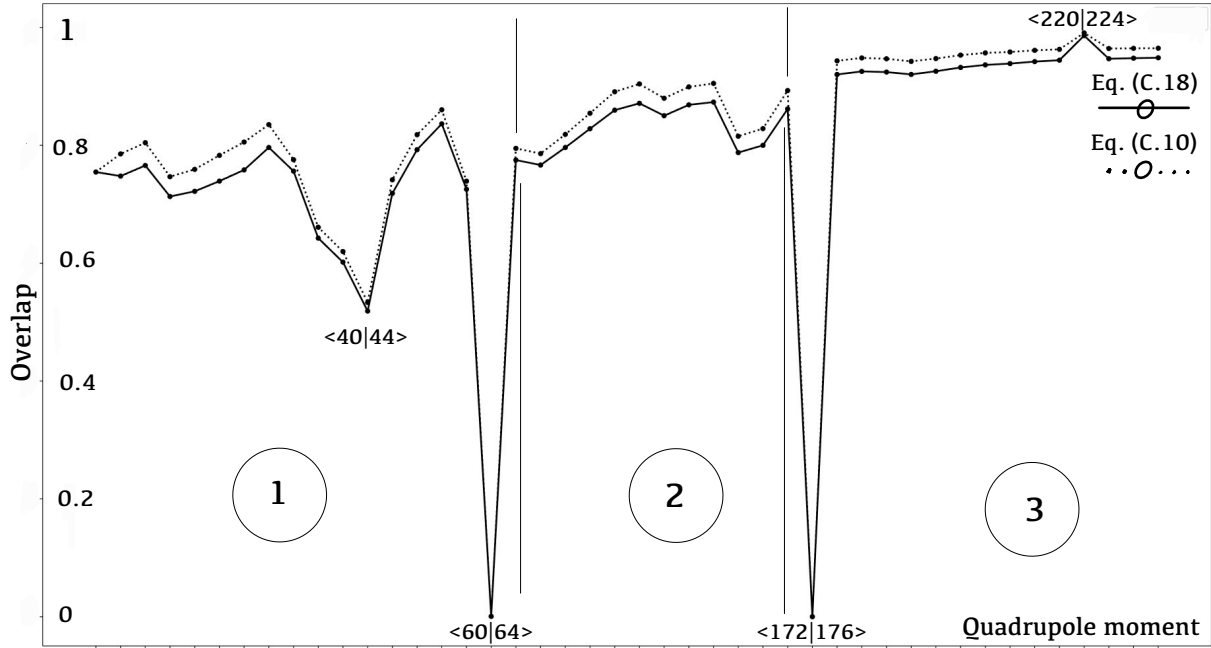
Figure 3.4: Norm overlaps, Equation (3.21), calculated between adjacent configurations of the PES of ^{252}Cf, Figure 3.3. Two discontinuities are identified within the first and third region of the figure, at $Q_{20} = 60$ b and $Q_{20} = 172$ b, respectively. In the first and third regions of the plot, $0 < Q_{20} < 64$ and $168 < Q_{20} < 232$, all adjacent overlaps are shown. The mesh step of these regions is 4 b. In the second region of the plot, where no discontinuities have been found and $\mathcal{N}_{01} > 0.7$, only a limited sample of adjacent norm overlaps is represented. All values lower than 0.01 have been set to 0.01.
(dotted line): overlaps calculated using Equation (C.10). While the traditional formulas for the calculation of norm overlaps should be inapplicable to the case in which states are expanded in arbitrary bases, this approach has been nonetheless adopted in reference [136]. *(dotted line):* overlaps calculated with the correct formalism, Equation (C.18).
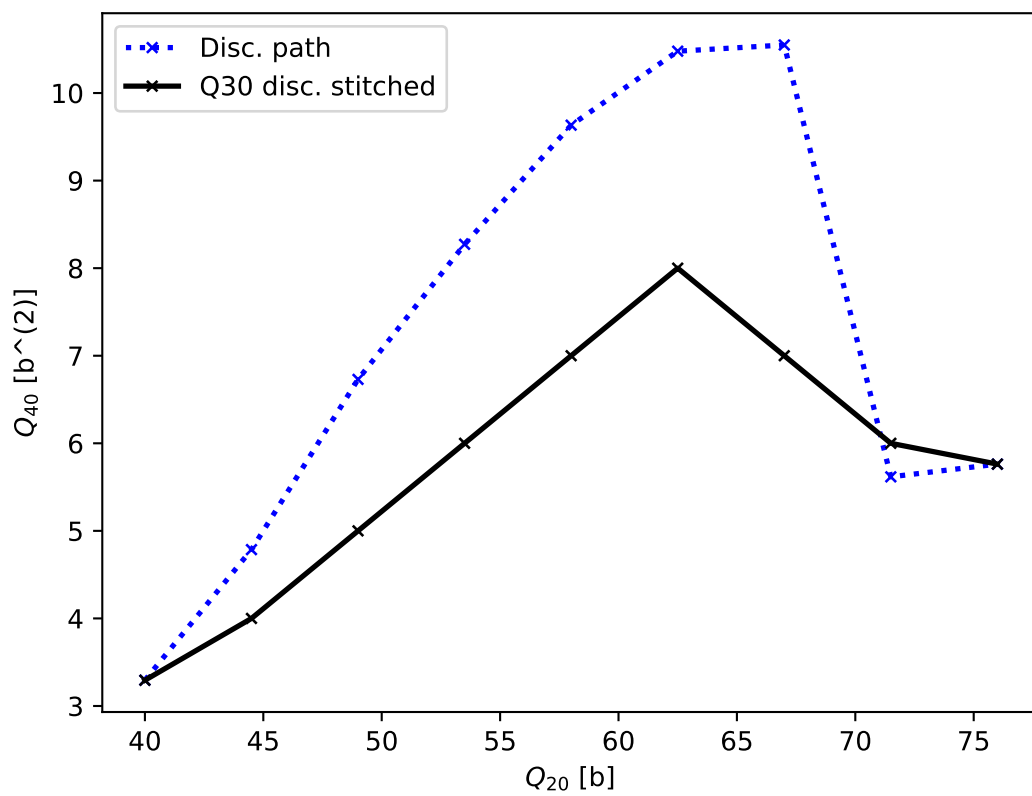
Figure 3.5: The hexadecupole moment of ^{252}Cf in proximity of the first discontinuity of Figure 3.3. In dotted blue, the original evolution of the hexadecupole moment, in solid black the hexadecupole moment on the DPM-DK path.
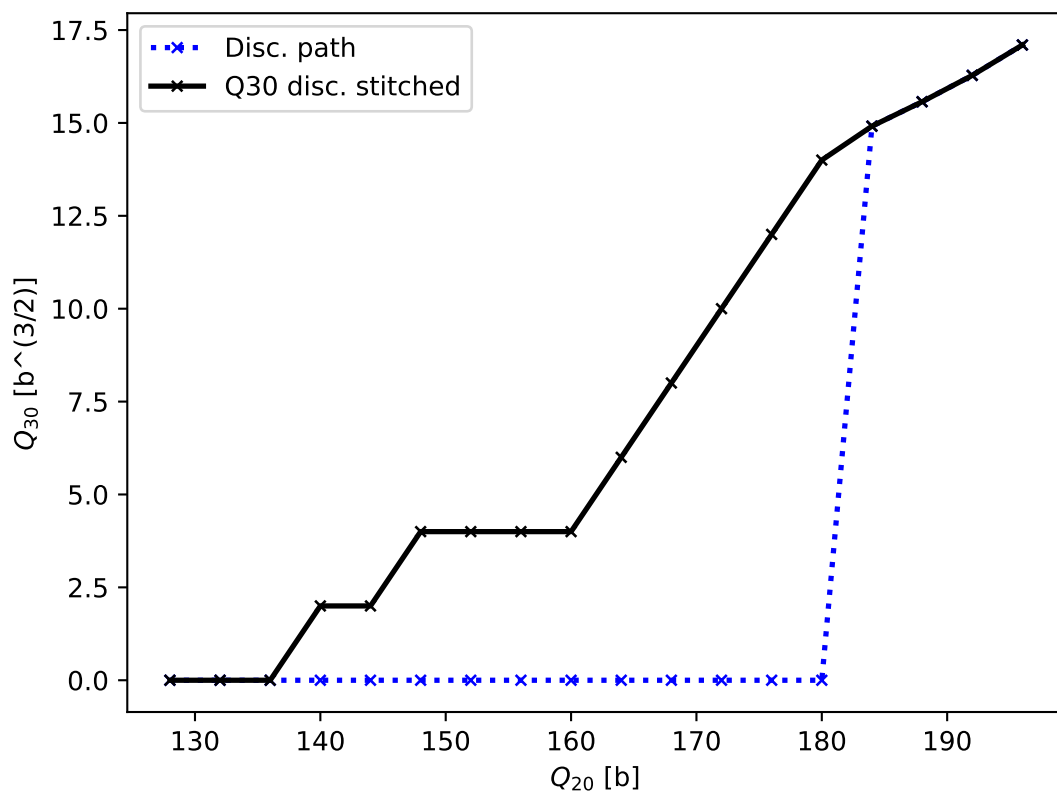
Figure 3.6: The octupole moment of ^{252}Cf in proximity of the second discontinuity of Figure 3.3. In dotted blue, the original evolution of the octupole moment, in solid black the octupole moment on the DPM-DK path.

^{284}**Fl**

A second application of the DPM-DK routine treated the case of ^{284}Fl, a super heavy element characterized by a rather low first barrier, $E_A = 5.32$ MeV, and therefore prone to undergo spontaneous fission with high probability. Again, a discontinuity was found in relation to the presence of lower-lying energy levels in the asymmetric valley. The original and the stitched PESs[3] are visible in Figure 3.7. Here, it is evident that the obtained path ignores the presence of locally favorable energy configurations with the purpose of minimizing the total energy integrated on the path. In fact, the DPM-DK path is characterized by locally higher energies in correspondence of the isomer state, at deformations within the quadrupole moment range $(65, 80)$ b. Nonetheless, the effect of crossing the ridge smoothly is that the height of the second barrier is considerably lowered.

^{294}**Fl**

A third application considered the nucleus ^{294}Fl, an isotope of the previous nucleus, characterized by a fission lifetime which is rather long for a super heavy element. The original potential energy surface is shown in Figure 3.8. Stitching of a discontinuity in the octupole moment, found in proximity of the second saddle point, has a remarkable impact on the height on the second barrier. In view of the calculation of the spontaneous fission lifetime along the path, Equation (3.19), the lowering of the second barrier caused by the smoothing procedure is compensated by increased values of the collective inertia, see Figure 3.6. The value of the fission lifetime is therefore not expected to be drastically modified.

3.6 Fission Lifetimes From Stitched Minimum Energy Paths

In order to establish quantitatively the actual usefulness of the DPM-DK routine for realistic calculations, fission lifetimes were calculated along stitched minimum energy paths, and compared to the result given by the discontinuous PESs. This is a test of the method that verifies if the new MEP is properly associated to the correct physical properties. This is an important conceptual step, as the smoothness of the path, while being a necessary condition for a path to be physically reliable, is not sufficient to guarantee it will be such. This is especially true con-

---

[3]The PESs of ^{284}Fl and ^{294}Fl have been calculated using HFBTHO. The SKM* Skyrme interaction has been adopted. The pairing strengths were adjusted: $V_{n0} = -268.9$ MeV fm^3 and $V_{p0} = -332.5$ MeV fm^3. The calculations used 26 major shells for the HO basis in which the single-nucleon states were expanded. The calculation considered a reduction of the basis corresponding to 1140 states, while the basis deformation has been optimized as a function of the nuclear deformation.

Figure 3.7: The potential energy surface of ^{284}Fl. The dotted blue line is the original, discontinuous, PES. The black solid line is the final DPM-DK path.

Figure 3.8: The potential energy surface of ^{294}Fl. The dotted blue line is the original, discontinuous, PES. The black solid line is the final DPM-DK path.

sidering the local failing of the adiabaticity condition of the stitched paths. The specific choice of the fission lifetime as quantity to calculate for this test is explained by the relatively straightforward techniques available to compute it. Moreover, no dynamical features are involved in its calculation.

In advanced applications, the fission lifetime is calculated by integrating the action on top of the least action path. Fission lifetimes calculated on MEPs are generally larger than those calculated on LAP. In our case, considering the purposes of the calculation, it has been considered a fair approximation to use static MEPs in place of LAPs. This is justified by reference [140], that provides a necessary condition for a MEP to be a LAP, and in particular shows that, when only shape-related degrees of freedom are considered, the static (minimum energy) calculation is equivalent to the dynamical and more quantal (least action) description. On the other hand, reference [141] shows that a direct comparison of the action (3.10) obtained using the two types of paths may differ up to a factor three when the particle number fluctuation degree of freedom is considered. This entails dramatic differences in the calculated lifetimes. In fact, since the collective inertia decreases as the square of the inverse pairing gap [142, 143], whereas the energy increases as the square of the pairing gap, the minimum of the action differs from the minimum of the energy. This means that pairing is indeed a fundamental ingredient for an accurate description of fission dynamics. As this goes beyond the scopes of the present manuscript, the reader is directed to [144] for further details. Finally, triaxiality features sometimes play an important role in determining the correct height of the second barrier [110, 145]. The PESs of this work are generated with HFBTHO, that allows to consider only axially symmetric deformations. With these premises in mind, it is not expected that the calculations performed on the MEP will be in full agreement with state-of-the-art results or experiments. Rather, they are expected to yield values of the more or less correct order of magnitude.

Finally, before moving on to discuss the obtained results, it is worth specifying that in all cases of study the calculated action S was found to be at least ten times larger than the squared reduced Plank constant, $\hbar^2$. As already mentioned, failing this condition would jeopardize the validity of the adoption of the semi-classical WKB approximation, and therefore the entire formalism presented in section 3.1.1 used for the calculation of fission lifetimes, Equation (3.19).

Indeed, the operation of stitching has a relevant impact on several physical properties of the nucleus. Figure 3.9 shows the evolution of the collective inertia of ^{252}Cf, calculated in accord to (3.16). The collective inertia is visibly diminished on the DPM-DK path in proximity of

Table 3.1: Spontaneous fission lifetime calculated on the discontinuous and DPM-DK smoothed path(s) for quadrupole-moment-constrained PES, compared to the state-of-the-art results.

Nucleus	Discontinuous path	DPM-DK path	Reference value
^{252}Cf	11.78 y	7.23 y, 6.43 y	2.65 y [146]
^{284}Fl	1.05 10^{-10} s	4.00 10^{-10} s	4.57 10^{-10} s [110]
^{294}Fl	1292 s	663 s	741 s [110]
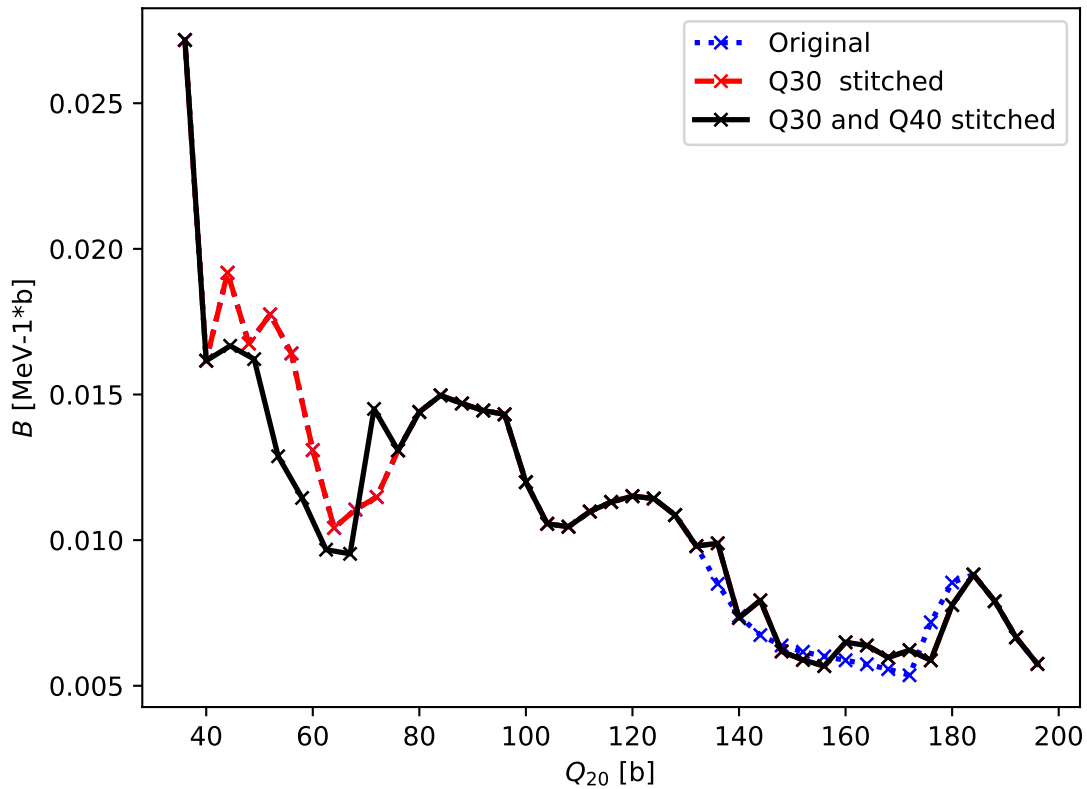
Figure 3.9: The ATDHFB collective inertia of ^{252}Cf as a function of the quadrupole deformation of the nucleus. In dotted blue, the original evolution of the collective inertia, in dashed red and solid black, the collective inertia on the DPM path.

the first barrier. Moreover, its trend is modified around the saddle point before the scission, where the stitching procedure has a large impact on the height of the second barrier. Considering the exponential dependence of Equation (3.19) on both the height of the energy barriers and the collective inertia, even small changes in these quantities may produce sensitive effects in the resulting fission lifetime. Nonetheless, a small but sensitive improvement of the lifetimes calculated along the smoothed trajectories is visible in the results illustrated in table 3.1. In the case of ^{252}Cf, where two discontinuities were found, one can see that the progressive stitching steadily improves the value of the fission lifetime towards the reference value. The same happens for the super heavy element ^{284}Fl, whose PES is characterized by a very low first energy barrier, and for which therefore a very short lifetime is obtained. In the case of ^{294}Fl, characterized by a first barrier of 7.39 MeV, the α-decay lifetime, equal to $10^{-0.08}$ s, is larger than the spontaneous fission lifetime. Since this contradicts the discussed assumptions for the adoption of the WKB approximation, the result obtained from (3.19) should not be considered physically trustworthy. Nonetheless, the fission lifetimes calculated on the discontinuous and stitched paths are in rough agreement with the reference results, as visible in table 3.1. Moreover, the energy gain for moving in a continuous way to the asymmetric valley entails a lower calculated spontaneous fission lifetime.
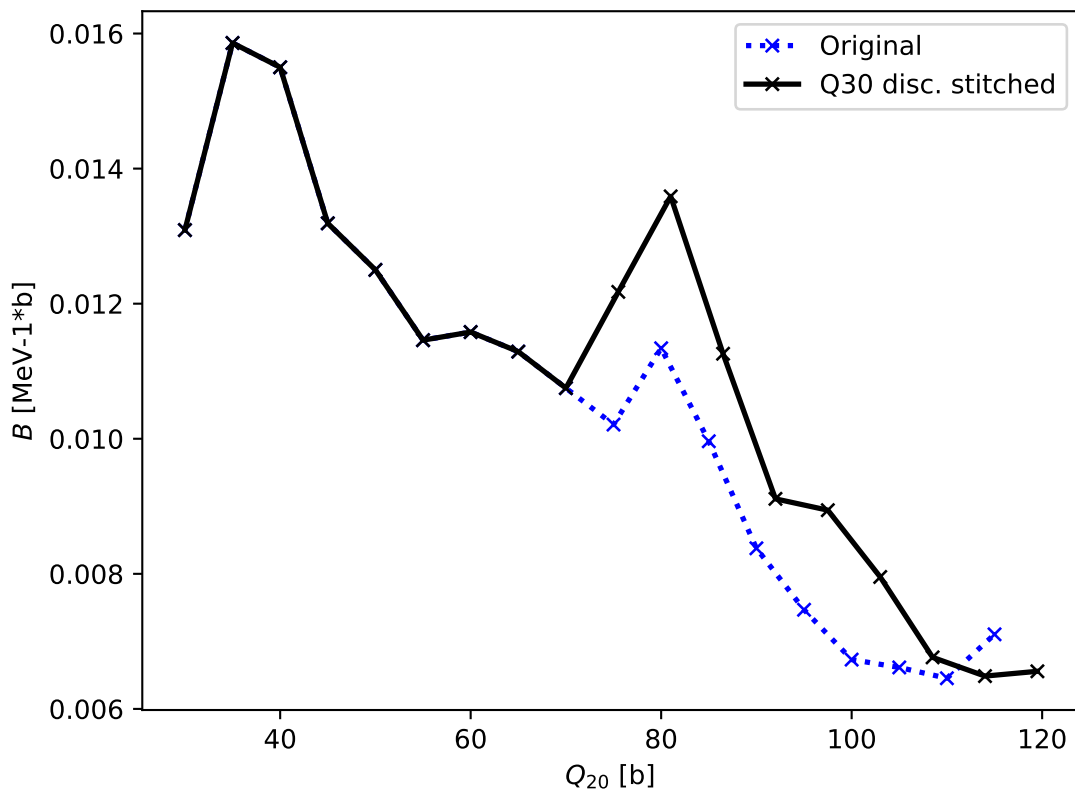
Figure 3.10: The ATDHFB collective inertia of ^{284}Fl as a function of the quadrupole deformation of the nucleus. In dotted blue, the original evolution of the collective inertia, in solid black the collective inertia on the DPM path.
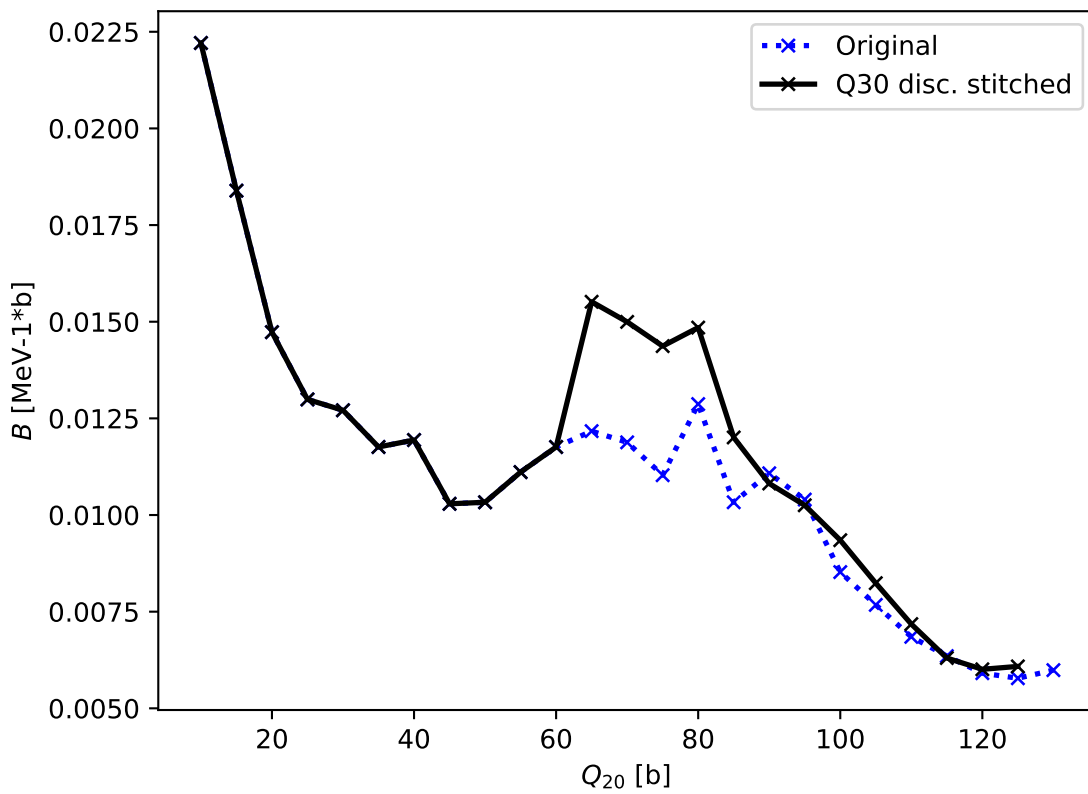
Figure 3.11: The collective inertia as a function of the quadrupole moment for ^{294}Fl. The dotted blue line is the inertia calculated on the original, discontinuous, PES. The black solid line is the calculated on the DPM path.

SUMMARY AND CONCLUSIONS

The first part of this work, reported in [147, 148], investigated for the first time in nuclear physics the inverse problem of Density Functional Theory. A formalism for its solution has been derived both in the non-relativistic and relativistic frameworks. Two inversion procedures, that already proved to be successful in other fields of physics, have been adapted to the nuclear case. They have been subsequently implemented and tested on a number of theoretical and empirical densities of closed-shell nuclei.

The inversion algorithms have been specifically chosen to be very different one from another. One of them, the Constrained Variation method, consists in the minimization of the kinetic energy of the fictitious Kohn-Sham system, whose orbitals are constrained to reproduce a given target density and to be orthonormal. The functional form of the Kohn-Sham potential is then extracted by solving a set of Euler-Lagrange equations. The formalism of this method is very general, and its eventual application to densities of deformed nuclei should be rather straightforward. On the other hand, its understanding and implementation are not particularly intuitive. Moreover, the results obtained in the case of spherical closed-shell nuclei are not exceptionally better than those of other simpler algorithms. The second method (vLB) consists in the inversion and iterative solution of the Kohn-Sham equations. At each step, the *Ansatz* for the Kohn-Sham potential is steadily adjusted in order to make the density of the Kohn-Sham system closer to the target density. While a generalization of this method for non-spherical or open-shell nuclear systems might prove to be cumbersome, the underlying idea is very intuitive and its implementation for closed-shell nuclei is not complex. Nonetheless, advanced computing techniques, such as the Broyden mixing procedure, must be employed to consistently reach convergence.

Both algorithms proved to be robust and in remarkable agreement one with the other. The Kohn-Sham potentials extracted from the empirical proton densities of ^{40}Ca and ^{208}Pb and from the neutron density of ^{208}Pb are physically reasonable in the interior and at the surface

of the nucleus. Conversely, the sum of Gaussians parameterization commonly employed for experimental densities leads to issues for the tail of the KS potentials: a divergent harmonic-oscillator-like asymptotic trend is found in all cases. In particular, it was verified that the non-physical behavior of the KS potentials begins at radii larger than the radius of the outermost or second-outermost Gaussian used in the parameterization. One can deduce that when the empirical densities are not properly backed up by data points, the derived KS potentials become unreliable. To furthermore corroborate this explanation, the inversion algorithms have been tested using as input theoretical densities calculated by means of HF calculations. In this case, where the asymptotic behavior of the densities is physically correct, the KS potential is reliable everywhere.

Realistic nuclear energy density functionals depend on spin densities and gradients of densities that cannot be measured experimentally. Despite the fact that trying to extend the implemented algorithms to tackle a larger set of nuclei, including deformed ones, might be interesting, it is evident that the sole information about empirical neutron and proton densities is insufficient to deduce an effective KS potential. Thus, the range of application of the inverse Kohn-Sham problem results limited. To partially address this issue, the iterative vLB method was extended and generalized to the relativistic framework. The most important reason to consider relativistic functionals is that within this formalism the spin-orbit potential emerges naturally, as a constructive combination of the scalar and vector nucleon potentials.

The relativistic generalization of the vLB algorithm has been tested on several theoretical scalar and vector nuclear densities. It proved to be reliable in calculating the scalar and vector potentials associated to them. Unfortunately, this generalization does not provide a direct solution to the fact that the scalar density is not an experimental observable. Accurate and well-assorted data exists only for charge proton densities, whereas the construction of the Kohn-Sham potential requires not only the isoscalar and scalar densities, but also the isovector ones. To further proceed in this line of research, one may try to exploit the equations of state of state of isospin symmetric and asymmetric nuclear matter. Data on proton vector densities could be combined with the equation of state of nuclear matter to determine the isoscalar-scalar and isovector channels of the KS potential.

A second problem associated to the application of the IKS procedure is that it is not completely clear how to employ the extracted KS potentials to build an actual NEDF. Even when a recipe for such a task had been found, the implementation of the NEDF would still depend

on the exact densities of a few specific and unrelated systems; it would not provide any direct information on the universal EDF. The idea of exploiting *ab initio* calculations for testing the IKS method on systems that are very close one to another in terms of their density would indeed be an intriguing continuation of this line of research. For instance, neutron drops would represent an ideal playground for such attempts. In that case, it could be possible to obtain a NEDF with a functional integration on a path of densities. This work proceeded instead to adapt the IKS+DFPT model to the field of nuclear physics. By using density functional perturbation theory, one can improve the form of a given NEDF towards the exact, unknown one. A model has been therefore proposed to make use of the piece of information encoded in the empirical densities and the derived Kohn-Sham potentials of a few finite systems. Specifically, the correct ground-state scalar and vector densities of a small number of finite closed-shell systems, together with the energy levels of the KS potentials derived from them, provided the ingredients necessary to estimate the first-order correction to a starting functional towards a target EDF.

The IKS+DFPT model has been tested in a few illustrative cases. The relativistic functional DD-PC1 has been taken as the exact target functional. The presented model has been employed to improve the local density approximation of the DD-PC1 functional towards the complete functional. To this purpose, the implemented routine returned the value of a number of parameters contained in the starting guess for the first-order correction of the zeroth-order EDF. A first test used as initial guess for the first-order correction the remaining part of the DD-PC1 functional. A second test started instead from an *Ansatz* given by a quadratic polynomial of the densities. In both cases the model accurately reproduced the density-dependent coupling functions.

The focus of the second part of this work has been an inherent limitation that accompanies fission simulations made within adiabatic SCMF models: the unavoidable appearance of artificial discontinuities on potential energy surfaces. The present manuscript addressed two tasks: a reliable procedure to assess the presence of a discontinuity on a PES was defined, and a routine to stitch a discontinuity by finding a smooth fission path across it was provided. The calculation of norm overlaps between states corresponding to adjacent points on a PES was identified as the quantity of interest to assess the presence of a discontinuity. The formalism presented in [132, 133] has been successfully extended and implemented. This implementation allows to overcome the limitations of traditional formulas. It provides a framework within which one can consistently consider states that are expanded in arbitrary harmonic oscillator

bases with different dimensions. Next, the DPM-DK routine, based on the Dynamic Programming Method, has been developed and tested. It can be used to find a smooth minimum energy path across a relatively small two-dimensional PES generated to patch a discontinuity found on a one-dimensional PES.

The physical reliability of the stitching paths that were obtained with the DPM-DK routine was verified. This has been done by calculating along them the most relevant quantity used to characterize spontaneous nuclear fission: the lifetime. In particular, the relaxation of the adiabaticity condition, exploited within the method in order to obtain smoother paths, has been verified not to have any negative effect on the calculated lifetimes. All the calculated lifetimes have been shown to be in agreement, up to an order of magnitude, with the corresponding reference values. A systematic improvement of the lifetimes calculated on the stitched paths was also found in comparison to the results obtained on the original, discontinuous, potential energy surfaces. The designed routine provides a valid and economic alternative to traditional approaches used to deal with the appearance of discontinuities on potential energy surfaces obtained with adiabatic self-consistent calculations.

An extension of the method to stitch discontinuities appearing on two-dimensional potential energy surfaces is under preparation. Such routine will allow to further corroborate the physical reliability of the obtained smoothed paths by investigating the response of other nuclear properties, possibly dynamical, to the stitching procedure. In this sense, the aim is to design a tool of wide usage for static and dynamic studies of the fission process.

Appendix A

THE NUCLEAR DENSITY

In this appendix a general definition of the nuclear density function is given, based on density operators. Stating from the quantity,

$$\Psi_A(\vec{x}_1,\ldots,\vec{x}_A)\Psi_A^*(\vec{x}_1,\ldots,\vec{x}_A)\,, \tag{A.1}$$

that represents the probability distribution associated with a specific solution of the Schrödinger equation, one can define the elements

$$\gamma_A = \Psi_A(\vec{x}_1',\ldots,\vec{x}_A')\Psi_A^*(\vec{x}_1,\ldots,\vec{x}_A) \tag{A.2}$$

of the density matrix. The diagonal entries of this matrix are (A.1). The elements γ_A can be thought as the representation, in the coordinates basis, of the density operator

$$\hat{\gamma}_A = |\Psi_A\rangle\langle\Psi_A|\,. \tag{A.3}$$

The operator $\hat{\gamma}_A$ is an hermitian projection, and

$$\mathrm{tr}(\hat{\gamma}_A) = \int d^A\vec{x}\int d^A\vec{x}'\,\Psi_A(\vec{x}_1',\ldots,\vec{x}_A')\Psi_A^*(\vec{x}_1,\ldots,\vec{x}_A) = 1 \tag{A.4}$$

if $|\Psi_A\rangle$ is a normalized wave function.

The expectation value of an observable $\hat{O}$ reads

$$\left\langle\hat{O}\right\rangle = \mathrm{tr}(\hat{\gamma}_A\hat{O})\,. \tag{A.5}$$

The previous equation establishes a one-to-one mapping between the density operator and each observable of the system under investigation. In fact, by comparison with

$$\left\langle \hat{O} \right\rangle = \frac{\int d\vec{x}\, \Psi^* \hat{O}\, \Psi}{\int d\vec{x}\, \Psi^* \Psi} = \frac{\langle \Psi | \hat{O} | \Psi \rangle}{\langle \Psi | \Psi \rangle} \; , \tag{A.6}$$

one notices that the density operator carries the same piece of information as any A-nucleon wave function $| \Psi_A \rangle$. Furthermore, while $| \Psi_A \rangle$ is defined up to an arbitrary phase factor, $\hat{\gamma}_A$ is unique. This operator-like description becomes essential whenever the system under investigation is part of some environment which is not isolated from it. In this case, the system does not have a complete Hamiltonian that contains all its degrees of freedom. The system is then open and any possibility of a wave function-based description is precluded [149].

Recalling the anti-symmetricity of the total wave function of a fermion system, one can simplify the density matrix and define a so-called reduced density matrix. Call γ_A, Equation (A.2), A^{th}-order density matrix. One then defines a reduced p^{th}-order density matrix

$$\gamma_p(\vec{x}_1', \ldots, \vec{x}_p'; \vec{x}_1, \ldots, \vec{x}_p) =$$
$$= \binom{A}{p} \int d\vec{x}_{p+1} \cdots \int d\vec{x}_A\, \gamma_A(\vec{x}_1', \ldots, \vec{x}_A'; \vec{x}_1, \ldots, \vec{x}_A) \; . \tag{A.7}$$

Specifically, being mainly interested in one- and two-body operators, one focuses on the 2nd-order density matrix

$$\gamma_2(\vec{x}_1', \vec{x}_2'; \vec{x}_1, \vec{x}_2) =$$
$$= \frac{A(A-1)}{2} \int d\vec{x}_3 \cdots \int d\vec{x}_A \gamma_A(\vec{x}_1', \ldots, \vec{x}_A'; \vec{x}_1, \ldots, \vec{x}_A) \; , \tag{A.8}$$

and the 1st-order density matrix

$$\gamma_1(\vec{x}_1'; \vec{x}_1) =$$
$$= A \int d\vec{x}_2 \cdots \int d\vec{x}_A \gamma_A(\vec{x}_1', \ldots, \vec{x}_A'; \vec{x}_1, \ldots, \vec{x}_A) \; , \tag{A.9}$$

All these operators are positive, semi-definite and hermitian. Also, antisimmetry requires that the interchange of two primed or two non-primed indices brings along a change of the sign of the density operators.

It is natural, whenever the quantities of interest do not involve the spin coordinate, to further

simplify the density matrices by a summation over the spin s_i. The 1st-order and the 2nd-order spinless density matrices read

$$\varrho_1(\vec{r}_1'; \vec{r}_1) = \int ds_1 \, \gamma_1(\vec{x}_1'; \vec{x}_1) \tag{A.10}$$

$$\varrho_2(\vec{r}_1', \vec{r}_2'; \vec{r}_1, \vec{r}_2) = \int ds_1 \int ds_2 \, \gamma_2(\vec{x}_1', \vec{x}_2'; \vec{x}_1, \vec{x}_2) \, , \tag{A.11}$$

and they are linked by the relation:

$$\varrho_1(\vec{r}_1'; \vec{r}_1) = \frac{2}{A-1} \int d\vec{r}_2 \, \varrho_2(\vec{r}_1', \vec{r}_2'; \vec{r}_1, \vec{r}_2) \, . \tag{A.12}$$

The diagonal entries of (A.10) provide the originally defined nuclear density, Equation (1.50).

It is also possible to write an energy formula, a generalized energy density functional

$$E[\varrho] = \int d\vec{r} \left[-\frac{\hbar^2}{2m} \nabla_{\vec{r}}^2 \, \varrho(\vec{r}'; \vec{r}) \right]_{\vec{r}'=\vec{r}} + \int d\vec{r} \, v(\vec{r}) \varrho_1(\vec{r}) + \tag{A.13}$$

$$+ \int d\vec{r}_1 \int d\vec{r}_2 w(\vec{r}_1, \vec{r}_2) \varrho_2(\vec{r}_1, \vec{r}_2) \, ; \tag{A.14}$$

the three terms represent the kinetic term, the external potential energy, and the nucleon-nucleon interaction energy, respectively. The advantage of the formula is that it involves only a function of three coordinates, $n_1(\vec{r})$, and two functions of six coordinates, $n_1(\vec{r}', \vec{r})$ and $n_2(\vec{r}_1, \vec{r}_2)$.

Appendix B

MULTIPLE CONSTRAINT METHOD

In [150], a linear-variation method to impose one or more constraints within an optimization routine was first presented. In this work, the method has been implemented within the RHB solver DIRHB [41]. With respect to other types of constraining procedures, such as the quadratic-constraint method [34, 151], this approach should be more stable. Moreover, whereas other methods allow constraining up to only two or three operators before getting overwhelmingly time consuming, in the so-called Multiple Constraints Method the computing time scales much slower with the number of constraints.

The constrained operators are embedded into the optimization process in the same fashion of the Lagrange multiplier method, that is by substituting the Hamiltonian of the system with the Routhian

$$\mathcal{H}(\mathcal{R}, \{\lambda\}_i) = \mathcal{H}(\mathcal{R}) - \sum_i \lambda_i \hat{\mathcal{F}}_i. \tag{B.1}$$

In agreement with the HFB and RHB formalism presented in section 1.2.2, each operator $\hat{\mathcal{F}}_i$ stands for

$$\hat{\mathcal{F}}_i = \begin{bmatrix} \hat{F}_i & 0 \\ 0 & -\hat{F}_i^* \end{bmatrix}^{(\text{ph})} \tag{B.2}$$

in the particle-hole canonical basis. Note that, since the generalized matrix is obtained through the diagonalization of the Routhian operator, it will also depend on the Lagrange multipliers:

$$\mathcal{R} = \mathcal{R}(\{\lambda\}_i) . \tag{B.3}$$

The main idea of the procedure is to finely adjust the Lagrange multipliers $\{\lambda\}_i$ at each iteration

of the routine, to make the expectation values of the constrained operators

$$\left\langle \hat{\mathcal{F}}_i \right\rangle = \frac{1}{2}\text{tr}\hat{F}_i + \frac{1}{2}\text{Tr}\hat{\mathcal{F}}_i\mathcal{R}$$
$$= f_i \, , \qquad\qquad\qquad (B.4)$$

equal to those desired. In the previous formula $\text{Tr}(\cdot)$ is intended as a super-trace [152], whereas $\text{tr}(\cdot)$ is the common trace operation. The following calculation of $\text{Tr}\hat{\mathcal{F}}_i\mathcal{R}$ should clarify the difference:

$$\text{Tr}\hat{\mathcal{F}}_i\mathcal{R} = \text{Tr}\begin{bmatrix} \hat{F}_i & 0 \\ 0 & -\hat{F}_i^* \end{bmatrix}\begin{bmatrix} \hat{\rho} & -\hat{\kappa} \\ \hat{\kappa}^* & 1 - \hat{\rho}^* \end{bmatrix}$$
$$= \text{Tr}\begin{bmatrix} \hat{F}_i\hat{\rho} & -\hat{F}_i\hat{\kappa} \\ -\hat{F}_i^*\hat{\kappa}^* & -\hat{F}_i^* + \hat{F}_i^*\hat{\rho}^* \end{bmatrix}$$
$$= \text{tr}\hat{F}_i\hat{\rho} - \text{tr}\hat{F}_i + \text{tr}\hat{F}_i\hat{\rho}$$
$$= 2f_i - \text{tr}(F_i) \, . \qquad\qquad (B.5)$$

Given the set $\{\lambda\}_i$ of Lagrange multipliers, the corrections $\{\delta\lambda\}_i$ necessary to yield the desired constraints $\{f\}_i$ can be obtained by imposing that the newly defined problem,

$$[\mathcal{H}(\mathcal{R}(\{\lambda + \delta\lambda\}_i), \{\lambda\}_i), \mathcal{R}(\{\lambda + \delta\lambda\}_i)] = 0 \, , \qquad (B.6)$$

is solved at the same time of the original problem,

$$[\mathcal{H}(\mathcal{R}(\{\lambda\}_i), \{\lambda\}_i), \mathcal{R}(\{\lambda\}_i)] = 0 \; ; \qquad\qquad (B.7)$$

both equations lead to solutions of the HFB/RHB problem, but only the former yields the desired expectation values f_i.

Consider the variation induced on the generalized density by the small, linear correction to the Lagrange multipliers:

$$\mathcal{R}(\{\lambda + \delta\lambda\}_i) = {}^{(0)}\mathcal{R} + {}^{(1)}\mathcal{R} \, , \qquad\qquad (B.8)$$

where

$$\mathcal{R}(\{\lambda\}_i) = {}^{(0)}\mathcal{R} \qquad\qquad\qquad (B.9)$$

is diagonal in the quasi-particle basis and it is idempotent. In fact, a necessary condition for a generalized matrix to solve the HFB/RHB problem is to be idempotent. This condition is then applied to (B.8). Up to linear terms in $\delta\lambda_i$,

$$
({}^{(0)}\mathcal{R} + {}^{(1)}\mathcal{R})^2 = {}^{(0)}\mathcal{R} + {}^{(1)}\mathcal{R}
$$

$$
\begin{bmatrix} 0 & 0 \\ 0 & 1 \end{bmatrix}
\begin{bmatrix} {}^{(1)}\mathcal{R}^{11} & {}^{(1)}\mathcal{R}^{12} \\ {}^{(1)}\mathcal{R}^{21} & {}^{(1)}\mathcal{R}^{22} \end{bmatrix}
+
\begin{bmatrix} {}^{(1)}\mathcal{R}^{11} & {}^{(1)}\mathcal{R}^{12} \\ {}^{(1)}\mathcal{R}^{21} & {}^{(1)}\mathcal{R}^{22} \end{bmatrix}
\begin{bmatrix} 0 & 0 \\ 0 & 1 \end{bmatrix}
= {}^{(1)}\mathcal{R}
$$

$$
\begin{bmatrix} 0 & {}^{(1)}\mathcal{R}^{12} \\ {}^{(1)}\mathcal{R}^{21} & 2{}^{(1)}\mathcal{R}^{22} \end{bmatrix}
=
\begin{bmatrix} {}^{(1)}\mathcal{R}^{11} & {}^{(1)}\mathcal{R}^{12} \\ {}^{(1)}\mathcal{R}^{21} & {}^{(1)}\mathcal{R}^{22} \end{bmatrix} . \tag{B.10}
$$

As a consequence, Equation (B.10) is verified only if

$$
{}^{(1)}\mathcal{R}^{ii} = 0 . \tag{B.11}
$$

Equation (B.6) is linearized exploiting Equation (B.7) and the property just derived, Equation (B.11):

$$
[\mathcal{H}(\mathcal{R}(\{\lambda + \delta\lambda\}_i), \{\lambda + \delta\lambda\}_i), \mathcal{R}(\{\lambda + \delta\lambda\}_i)] = 0
$$

$$
\left[\mathcal{H}(\mathcal{R}) + \frac{\partial\mathcal{H}}{\partial\mathcal{R}}\delta\mathcal{R} - \sum_i \hat{\mathcal{F}}_i \delta\lambda_i, {}^{(0)}\mathcal{R} + {}^{(1)}\mathcal{R}\right] = 0
$$

$$
\sum_i \delta\lambda_i \left[\mathcal{F}_i, {}^{(0)}\mathcal{R}\right] = \left[\mathcal{H}(\mathcal{R}(\{\lambda\}_i), \{\lambda\}_i), {}^{(1)}\mathcal{R}\right] + \left[\frac{\partial\mathcal{H}}{\partial\mathcal{R}}\delta\mathcal{R}, {}^{(0)}\mathcal{R}\right]
$$

$$
\sum_i \delta\lambda_i \begin{bmatrix} \mathcal{F}_i^{11} & \mathcal{F}_i^{12} \\ \mathcal{F}_i^{21} & \mathcal{F}_i^{22} \end{bmatrix} \begin{bmatrix} 0 & 0 \\ 0 & 1 \end{bmatrix} - \begin{bmatrix} 0 & 0 \\ 0 & 1 \end{bmatrix} \begin{bmatrix} \mathcal{F}_i^{11} & \mathcal{F}_i^{12} \\ \mathcal{F}_i^{21} & \mathcal{F}_i^{22} \end{bmatrix}
$$

$$
= \begin{bmatrix} \epsilon_\alpha & \mathcal{H}^{12} \\ \mathcal{H}^{21} & -\epsilon_\beta \end{bmatrix} \begin{bmatrix} 0 & {}^{(1)}\mathcal{R}^{12} \\ {}^{(1)}\mathcal{R}^{21} & 0 \end{bmatrix} - \begin{bmatrix} 0 & {}^{(1)}\mathcal{R}^{12} \\ {}^{(1)}\mathcal{R}^{21} & 0 \end{bmatrix} \begin{bmatrix} \epsilon_\alpha & \mathcal{H}^{12} \\ \mathcal{H}^{21} & -\epsilon_\beta \end{bmatrix}
$$

$$
+ \begin{bmatrix} \frac{\partial\mathcal{H}}{\partial\mathcal{R}}\delta\mathcal{R}^{11} & \frac{\partial\mathcal{H}}{\partial\mathcal{R}}\delta\mathcal{R}^{12} \\ \frac{\partial\mathcal{H}}{\partial\mathcal{R}}\delta\mathcal{R}^{21} & \frac{\partial\mathcal{H}}{\partial\mathcal{R}}\delta\mathcal{R}^{22} \end{bmatrix} \begin{bmatrix} 0 & 0 \\ 0 & 1 \end{bmatrix} - \begin{bmatrix} 0 & 0 \\ 0 & 1 \end{bmatrix} \begin{bmatrix} \frac{\partial\mathcal{H}}{\partial\mathcal{R}}\delta\mathcal{R}^{11} & \frac{\partial\mathcal{H}}{\partial\mathcal{R}}\delta\mathcal{R}^{12} \\ \frac{\partial\mathcal{H}}{\partial\mathcal{R}}\delta\mathcal{R}^{21} & \frac{\partial\mathcal{H}}{\partial\mathcal{R}}\delta\mathcal{R}^{22} \end{bmatrix}
$$

$$
\sum_i \delta\lambda_i \begin{bmatrix} 0 & \mathcal{F}_i^{12} \\ -\mathcal{F}_i^{21} & 0 \end{bmatrix} = \begin{bmatrix} 0 & (\epsilon_\alpha + \epsilon_\beta){}^{(1)}\mathcal{R}^{12} + \frac{\partial^2\mathcal{E}}{\partial\mathcal{R}_{\alpha\beta}^2}\delta\mathcal{R}_{\alpha\beta}^{12} \\ -(\epsilon_\alpha + \epsilon_\beta){}^{(1)}\mathcal{R}^{21} - \frac{\partial^2\mathcal{E}}{\partial\mathcal{R}_{\alpha\beta}^2}\delta\mathcal{R}_{\alpha\beta}^{21} & 0 \end{bmatrix}
$$

$$
\sum_i \delta\lambda_i \begin{bmatrix} 0 & \mathcal{F}_i^{12} \\ -\mathcal{F}_i^{21} & 0 \end{bmatrix} = M{}^{(1)}\mathcal{R} . \tag{B.12}
$$

In the last step, the QRPA (linear response) matrix $\mathcal{M}$ has been introduced. Equation (B.12) is manipulated to obtain the formula for the calculation of the first-order correction to the generalized density:

$$^{(1)}\mathcal{R}^{pq}_{\alpha\beta} = \sum_i \delta\lambda_i M^{-1}_{\alpha\beta} \mathcal{F}^{pq}_{\alpha\beta;i} \; . \tag{B.13}$$

with $p \neq q$.

The assumption of the cranking approximation [117] enables a great simplification of the previous expression:

$$^{(1)}\mathcal{R}^{pq}_{\alpha\beta} = \sum_i \delta\lambda_i (\epsilon_\alpha + \epsilon_\beta)^{-1} \mathcal{F}^{pq}_{\alpha\beta;i} \; . \tag{B.14}$$

The cranking approximation fundamentally consists in neglecting the residual interaction between quasi-particles. Then, the inverse of the QRPA matrix $\mathcal{M}$ becomes:

$$\mathcal{M}^{-1}_{\alpha\beta} = \begin{bmatrix} (\epsilon_\mu + \epsilon_\nu)^{-1}\delta_{\mu\alpha}\delta_{\nu\beta} & 0 \\ 0 & (\epsilon_\mu + \epsilon_\nu)^{-1}\delta_{\mu\alpha}\delta_{\nu\beta} \end{bmatrix} \; ; \tag{B.15}$$

Note that this approximation is also equivalent to fully neglect any effect of variation of the Hamiltonian with respect to the Lagrange multipliers. The resulting matrix is diagonal, with eigenvalues given by pairs of quasiparticle energies.

Denote $\vec{\mathcal{F}}_i = (\mathcal{F}^{12}_i, \mathcal{F}^{21}_i)^{\text{t}}$ and allow a similar notation for the generalized matrix. The differences δf_i between the expectation values obtained with the solutions to the two problems (B.7) and (B.6) depend on the adjustments $\delta\lambda_i$, according to:

$$\begin{aligned} \delta f_i &= f_i(\lambda_i + \delta\lambda_i) - f_i(\lambda_i) \\ &= \frac{1}{2}\text{Tr}\hat{\mathcal{F}}_i \mathcal{R}(\{\lambda_i + \delta\lambda_i\}) - \frac{1}{2}\text{Tr}\hat{\mathcal{F}}_i \mathcal{R}(\{\lambda_i\}) \\ &= \frac{1}{2}\text{Tr}\hat{\mathcal{F}}_i^{(1)}\mathcal{R} \tag{B.16} \\ &= \frac{1}{2}\vec{\mathcal{F}}_i^\dagger \cdot {}^{(1)}\vec{\mathcal{R}} \tag{B.17} \\ &= \frac{1}{2}\sum_j \vec{\mathcal{F}}_i^\dagger \cdot M^{-1}\vec{\mathcal{F}}_j \delta\lambda_j \\ &= \mathcal{T}_{ij}\delta\lambda_j \; ; \tag{B.18} \end{aligned}$$

the matrix of the correlations among the constraints, $\mathcal{T}$, has been defined. Finally, one finds the

inverse relation

$$\delta\lambda_j = \sum_i (\frac{1}{2}\vec{\mathcal{F}}_j^\dagger \cdot \mathcal{M}^{-1}\vec{\mathcal{F}}_i)^{-1}\delta f_i = \mathcal{T}_{ji}^{-1}\delta f_i. \tag{B.19}$$

The formulas that prescribe how to update the Lagrange multipliers and the generalized density matrix, Equations (B.19) and (B.14), have been derived in the quasiparticle basis. Therefore, one makes use of the following rule to move from the particle-hole to the quasi-particle basis,

$$\mathcal{F}^{(\mathrm{qp})} = \mathcal{W}^\dagger \mathcal{F}^{(\mathrm{ph})}\mathcal{W} = \begin{bmatrix} U^\dagger F U - V^\dagger F^* V & U^\dagger F V^* - V^\dagger F^* U^* \\ V^\mathrm{t} F U - U^\mathrm{t} F^* V & V^\mathrm{t} F V^* - U^\mathrm{t} F^* U^* \end{bmatrix}. \tag{B.20}$$

together with $\mathcal{F}^{12} = \mathcal{F}^{21*}$. The matrix $\mathcal{T}$ is expressed in terms of the operators in the particle-hole representation:

$$\begin{aligned} T_{ij} &= \frac{1}{2}[(V^t F^\dagger U - U^t F^t V)_{i\alpha} M_{\alpha\beta}^{-1}(U^\dagger F V^* - V^\dagger F^* U^*)_{\beta j} + \mathrm{h.c}] \\ &= \frac{1}{2}[(V^t F^\dagger U M^{-1} U^\dagger F V^* - U^t F^t V M^{-1} U^\dagger F V^* + \\ &\quad - V^t F^\dagger U M^{-1} V^\dagger F^* U^* + U^t F^t V M^{-1} V^\dagger F^* U^*) + \mathrm{h.c}] \end{aligned} \tag{B.21}$$

For instance, the particle number operator in oscillator basis is represented by the identity matrix:

$$\hat{\mathcal{N}}_q = \sum_{\nu\nu'} \delta_{\nu\nu'} a_\nu^\dagger a_{\nu'}. \tag{B.22}$$

where $|\nu\rangle = |n_z n_r \Lambda m_s\rangle$ in cylindrical coordinates.

For the quadrupole moment operator, one starts from its representation in the coordinate basis,

$$\begin{aligned} \hat{\mathcal{Q}}_{20} &= \int r\, dr dz d\phi\, \rho(r,\varphi,z)(2z^2 - r^2) \\ &= \int r\, dr dz d\phi\, (2z^2 - r^2) \\ &\quad \sum_{\nu\nu'}\sum_\sigma \int r'\, dr' dz' d\phi'\, \varphi_\nu^*(r',z',\phi',\sigma)\varphi_{\nu'}(r',z',\phi',\sigma)\delta(\vec{r} - \vec{r'})a_\nu^\dagger a_{\nu'}, \end{aligned} \tag{B.23}$$

117

and from this expression one reads out the matrix representation:

$$
\begin{aligned}
q_{\nu\nu'}^{(20)} &= \sum_\sigma \int r \, dr dz d\phi \, \varphi_\nu^*(r, z, \phi, \sigma)\varphi_{\nu'}(r', z', \phi', \sigma)(2z^2 - r^2) \\
&= \int r \, dr dz d\phi \, \varphi_{n_z}^*(z, b_z)\varphi_{n_r,\Lambda}^*(r, b_r) \\
&\quad \frac{e^{i\Lambda\phi}}{\sqrt{2\pi}}\varphi_{n_z'}^*(z, b_z)\varphi_{n_r',\Lambda'}^*(r, b_r)\frac{e^{i\Lambda'\phi}}{\sqrt{2\pi}}(2z^2 - r^2)\sum_\sigma \chi_{m_s}(\sigma)\chi_{m_s'}(\sigma) \\
&= \delta_{m_s m_s'}\delta_{\Lambda\Lambda'}\int d\xi d\eta \, N_{n_z}N_{n_z'}N_{n_r,\Lambda}N_{n_r',\Lambda'}H_{n_z}(\xi)H_{n_z'}(\xi)e^{-\xi^2} \\
&\quad L_{n_r,\Lambda}(\eta)L_{n_r',\Lambda'}(\eta)\eta^{(|\Lambda|+|\Lambda'|)/2}e^{-\eta}(2\xi^2 b_z^2 - \eta^2 b_r^2),
\end{aligned}
$$

where $\xi = z/b_z$, $\eta = r^2/b_r^2$, $L_{n_r,\Lambda}(\eta)$ are Laguerre polynomials, and $H_{n_z'}(\xi)$ are Hermite polynomials.

B.0.1   Implementation

Here, some relevant sections of the implementation of the Multiple Constraint method are discussed, in the cases of the constraints to the particle number and quadrupole moment operators. The first step consists of building the constrained operators in the harmonic oscillator (canonical) basis. In fact, the Routhian is defined in such basis. This is done within the subroutine "cstrgognyQ":

```fortran
      do nnn = 1,3        ! loop over constraint

      if (nnn.le.2) then
!  build number soperator (neutrons/protons)

      do ib = 1,nb

      nf    = id(ib,1)

      do n2 =  1,NFX      ! NFX is the maximal dimension of any K-parity block;
      do n1 =  n2,NFX     ! thus, all diagonal blocks are square matrices NFX*NFX.

      if ((n1.ne.n2).or.n1.gt.nf) then ! nf is the dimension of non-zero K-blocks.

      q0sh(n1,n2,ib,nnn) = zero
      q0sh(n2,n1,ib,nnn) = q0sh(n1,n2,ib,nnn)
      cycle

      endif

      q0sh(n1,n2,ib,nnn) = one

      enddo    ! n1
      enddo    ! n2
      enddo    ! ib

      else    ! build quadrupole moment matrix

      do ib = 1,nb

      n0f   = ia(ib,1)
      nf    = id(ib,1)
      nh    = id(ib,1) + id(ib,2)
      k1    = ka(ib,it)
      ke    = ka(ib,it) + kd(ib,it)

      do n2 =   1,NFX

      nz2 = nz(n2+n0f)
      nr2 = nr(n2+n0f)
      ml2 = ml(n2+n0f)
      ms2 = ms(n2+n0f)

      do n1 =   n2,NFX

      nz1 = nz(n1+n0f)
      nr1 = nr(n1+n0f)
      ml1 = ml(n1+n0f)
      ms1 = ms(n1+n0f)
```

```fortran
        if ((n1.gt.nf).or.(ml1.ne.ml2).or.(ms1.ne.ms2)) then
! use deltas
q0sh(n1,n2,ib,nnn) = zero
q0sh(n2,n1,ib,nnn) = q0sh(n1,n2,ib,nnn)
        cycle

        else   ! Integral over mesh points

t = zero

        do il = 0,NGL

rrp = rb(il)**2
s = zero

        do ih = 0,NGH

zz   = zb(ih)**2
s = s + (two*zz - rrp)*
qh(nz1,ih)*qh(nz2,ih)

        enddo  ! ih

t = t + s*ql(nr1,ml1,il)*ql(nr2,ml2,il)

        enddo  ! il

q0sh(n1,n2,ib,nnn) = t
q0sh(n2,n1,ib,nnn) = q0sh(n1,n2,ib,nnn)

        endif

        enddo    ! n1
        enddo    ! n2
        enddo    ! ib
        endif
        enddo    ! nnn
```

At each iteration, the code transforms these matrices into the quasiparticle representation, according to Equation (B.20). This is done within the subroutine *cstrgogny*. The matrix multiplications are performed with the aid of the LAPAK[1] method *DGEMM*. Note that, because of time-reversal symmetry, the matrices can be taken real. Also, the constrained operators are symmetric matrix.

```fortran
      do it = 1,2
      do ib = 1,nb
      nf  = id(ib,1)
      nh  = id(ib,1) + id(ib,2)
      k1  = ka(ib,it)
      ke  = ka(ib,it) + kd(ib,it)
c
      do n2 = 1,NFX
      do n1 = 1,NFX
      if ((n1.le.nf).and.(n2.le.nf)) then
      Ufg(n1,n2,ib,it) = fguv(n1   ,k1+n2,it)  ! U
      Vfg(n1,n2,ib,it) = fguv(n1+nh,k1+n2,it)  ! V
      else
      Ufg(n1,n2,ib,it) = zero
      Vfg(n1,n2,ib,it) = zero
      endif
      enddo              ! n1
      enddo                ! n2
      enddo                  ! ib
      enddo                    ! it
c

      do nn =1,no_cstr
      do it = 1,2
      do ib = 1,nb
      call DGEMM('t','n',NFX,NFX,NFX,one,Vfg(:,:,ib,it),NFX,  ! V^{t}f
     &              q0sh(:,:,ib,nn),NFX,zero,Vf(:,:,ib,it,nn),NFX)
      call DGEMM('n','n',NFX,NFX,NFX,one,Vf(:,:,ib,it,nn),NFX,  ! V^{t}fU
     &              Ufg(:,:,ib,it),NFX,zero,VfU(:,:,ib,it,nn),NFX)
      call DGEMM('t','n',NFX,NFX,NFX,one,Ufg(:,:,ib,it),NFX,  ! U^{t}f
     &              q0sh(:,:,ib,nn),NFX,zero,Uf(:,:,ib,it,nn),NFX)
      call DGEMM('n','n',NFX,NFX,NFX,one,Uf(:,:,ib,it,nn),NFX,  ! U^{t}fV
     &              Vfg(:,:,ib,it),NFX,zero,UfV(:,:,ib,it,nn),NFX)
      enddo              ! ib
      enddo                ! it
      enddo                  ! nn
c
      do nn2 = 1,no_cstr
      do nn1 = 1,no_cstr
      do it =1,2
      do it1 = 1,2
      do ib = 1,nb
      call DGEMM('n','n',NFX,NFX,NFX,one,  ! VfUUfV
     &                  VfU(:,:,ib,it1,nn1),NFX,
     &                  UfV(:,:,ib,it,nn2),NFX,zero,
     &                  VfUUfV(:,:,ib,it1,it,nn1,nn2),NFX)
      call DGEMM('n','n',NFX,NFX,NFX,one,  ! UfVVfU (it1.it2.nn1.nn2)
     &                  UfV(:,:,ib,it1,nn1),NFX,
     &                  VfU(:,:,ib,it,nn2),NFX,zero,
     &                  UfVVfU(:,:,ib,it1,it,nn1,nn2),NFX)
      call DGEMM('n','n',NFX,NFX,NFX,one,  ! VfUVfU
```

---

[1] https://netlib.org/lapack/

```
&                         VfU(:,:,ib,it1,nn1),NFX,
&                         VfU(:,:,ib,it,nn2),NFX,zero,
&                         VfUVfU(:,:,ib,it1,it,nn1,nn2),NFX)
call DGEMM('n','n',NFX,NFX,NFX,one,   ! UfVUfV
&                         UfV(:,:,ib,it1,nn1),NFX,
&                         UfV(:,:,ib,it,nn2),NFX,zero,
&                         UfVUfV(:,:,ib,it1,it,nn1,nn2),NFX)
enddo            ! ib
enddo              ! it1
enddo                ! it2
enddo                ! nn1
enddo                ! nn2
```

Within the same routine, the correlation matrix $\mathcal{T}$ and its inverse are calculated. This matrix is used for the calculation of the adjustments to the Lagrange multipliers. Because of time-reversal symmetry, one gets an extra factor two in the definition of the correlation matrix; in fact, at the code level, one does not distinguish among terms of the type $U^{\dagger}FV^{*}V^{\text{t}}F^{*}U$ and $U^{\text{t}}F^{*}VV^{\dagger}FU^{*}$. Another extra factor two in the definition of the correlation matrix is due to the fact that the code stores only one half of the matrices

$$U = \begin{bmatrix} u & 0 \\ 0 & u^* \end{bmatrix} \tag{B.24}$$

and

$$V = \begin{bmatrix} 0 & -v^* \\ v & 0 \end{bmatrix} , \tag{B.25}$$

that is, only the u and v matrices. This also implies that one needs to correct some signs with respect to the formula (B.21). In fact, only the upper part of the matrix (B.2) is stored, and the signs of those terms containing an odd number of contributions from the lower part of such matrix must be switched. In particular, these are the second and third terms in Equation (B.21).

```
do it =1,no_{cstr}
do it1 = 1,no_{cstr}
if (it1.le.2.and.it.le.2) then   ! calculates correlations
do ib = 1,nb
nf  = id(ib,1)
nh  = id(ib,1) + id(ib,2)
k1l  = ka(ib,it1)
k1r  = ka(ib,it)
do n2 = 1,NFX
do n1 = 1,NFX
if ((n1.le.nf).and.(n2.le.nf)) then
TCorr(it1,it) = TCorr(it1,it) + 8.d0
&                    *(VfUUfV(n1,n2,ib,it1,it,it1,it)
&                    + UfVVfU(n1,n2,ib,it1,it,it1,it)
&                    + UfVUfV(n1,n2,ib,it1,it,it1,it)   ! sign is switched
```

```fortran
     &                           + VfUVfU(n1,n2,ib,it1,it,it1,it)) ! sign is switched
     &                      /(equ(k1l+n1,it1)
     &                         + equ(k1r+n2,it))
          endif
          enddo          ! n1
          enddo            ! n2
c
          enddo              ! ib
          endif


          if (it1.gt.2.or.it.gt.2.and.icstr.gt.0) then ! calculates correlations
c
          do ib = 1,nb
          nf  = id(ib,1)
          nh  = id(ib,1) + id(ib,2)
          do n2 = 1,NFX
          do n1 = 1,NFX
          if ((n1.le.nf).and.(n2.le.nf)) then
          do it4 = 1,2
          if (it1.eq.it) then
          do it3 =1,2
          TCorr(it1,it) = TCorr(it1,it) + 8.d0*
     &                     (VfUUfV(n1,n2,ib,it3,it4,it1,it)
     &                      + UfVVfU(n1,n2,ib,it3,it4,it1,it)
     &                      + UfVUfV(n1,n2,ib,it3,it4,it1,it)  ! sign is switched
     &                      + VfUVfU(n1,n2,ib,it3,it4,it1,it)) ! sign is switched
     &                     /(equ(ka(ib,it3)+n1,it3)             ! QRPA matrix
     &                      + equ(ka(ib,it4)+n2,it4))
          enddo ! it3
          endif
          if (it1.gt.it) then
c
          TCorr(it1,it) = TCorr(it1,it) + 8.d0
     &                     *(VfUUfV(n1,n2,ib,it4,it,it1,it)
     &                      + UfVVfU(n1,n2,ib,it4,it,it1,it)
     &                      + UfVUfV(n1,n2,ib,it4,it,it1,it)  ! sign is switched
     &                      + VfUVfU(n1,n2,ib,it4,it,it1,it)) ! sign is switched
     &                     /(equ(ka(ib,it4)+n1,it4)
     &                      + equ(ka(ib,it)+n2,it))
c
          endif
          if (it.gt.it1) then
          TCorr(it1,it) = TCorr(it1,it) + 8.d0
     &                     *(VfUUfV(n1,n2,ib,it1,it4,it1,it)
     &                      + UfVVfU(n1,n2,ib,it1,it4,it1,it)
     &                      + UfVUfV(n1,n2,ib,it1,it4,it1,it)  ! sign is switched
     &                      + VfUVfU(n1,n2,ib,it1,it4,it1,it)) ! sign is switched
     &                     /(equ(ka(ib,1)+n1,it1)
     &                      + equ(ka(ib,it4)+n2,it4))
          endif
          enddo            ! it4
          endif
          enddo            ! n1
          enddo              ! n2
c
          enddo                ! ib
          endif
c
          enddo                  ! it1
          enddo                  ! it



c-----Invert matrix T
c------------------------------------------------------------------
          call DGETRF(no_cstr,no_cstr,TCorr,3,ipiv,ierror)
```

```
        call DGETRI(no_cstr,TCorr,3,ipiv,workk,3,ierror)

c-----Calculates corrections to the Lagrange multipliers
        call DGEMV('n',3,3,two,TCorr,3,ddf,1,zero,dal,1)
```

Finally one calculate the correction to the generalized matrix, which leads to the desired expectation values for the constraint operators. Again, some signs needs to be changed; in this case those of the second terms in the off-diagonal elements of matrix (B.20).

```
        c-----Adjust Generalized Density
        do it =1,2
        il = 0
        do ib = 1,nb           ! loop over the blocks
        k1  = ka(ib,it)
        ke  = ka(ib,it) + kd(ib,it)
        kf  = kd(ib,it)
        c
        do kl = 1,kf
        do kr = kl,kf
        il  = il + 1
        ddR(il,it)  = dal(it)*4.d0*(VfU(kl,kr,ib,it,it) ! sign is switched
     &                 + UfV(kl,kr,ib,it,it))/
     &                 (equ(k1 + kl,it)+equ(k1 + kr,it))
        if (icstr.gt.0) then
        ddR(il,it)  = ddR(il,it)
     &                   + dal(3)*4.d0*(VfU(kl,kr,ib,it,3)        ! sign is switched
     &                   + UfV(kl,kr,ib,it,3))/
     &                   (equ(k1 + kl,it)+equ(k1 + kr,it))
        endif
        aka(il,it) = aka(il,it) + xmi*ddR(il,it)
        enddo           ! kl
        enddo              ! kr
        c
        enddo                 ! ib
        enddo
```

Appendix C

NORM OVERLAPS IN ARBITRARY HARMONIC OSCILLATOR BASES

The following presentation follows the method discussed in [132, 133] and extends the formalism to consider bases with different dimensions.

Let the two states $|\phi_0\rangle$ and $|\phi_1\rangle$ be respectively expanded in the bases $\mathcal{B}_0 = \{c_{0,k}^\dagger\}_{k=0}^{N_0}$ and $\mathcal{B}_1 = \{c_{1,k}^\dagger\}_{k=0}^{N_1}$, where each set of creation operators separately satisfies the canonical anti-commutation relations. The Bogoliubov transformation introduced in Equation (1.24) defines the quasiparticle creation operators $c_{0,k}^\dagger$. In matrix representation, these are described in terms of the Bogoliubov block-structure matrices V_i and U_i:

$$
V_i = \begin{bmatrix} v_i & 0 \\ 0 & 0 \end{bmatrix} , \tag{C.1}
$$

$$
U_i = \begin{bmatrix} u_i & 0 \\ 0 & d_i \end{bmatrix} , \tag{C.2}
$$

where the index takes value $i = 0, 1$. The blocks v_i and u_i are the $N_i \times N_i$ matrices that characterize the states $|\phi_i\rangle$, whereas the d_i are arbitrary unitary matrices.

A unitary block matrix,

$$
R = \begin{bmatrix} \mathcal{R} & \mathcal{S} \\ \mathcal{T} & \mathcal{U} \end{bmatrix} , \tag{C.3}
$$

connects the complete bases $\mathcal{B}_0 \cup \bar{\mathcal{B}}_0$ and $\mathcal{B}_1 \cup \bar{\mathcal{B}}_1$. Specifically, R is the matrix representation of the operator $\hat{\mathcal{T}}_{01}$ defined by the relation $\hat{\mathcal{T}}_{01} c_{0,k}^\dagger \hat{\mathcal{T}}_{01}^\dagger = c_{1,k}^\dagger$, and the upper-left block $\mathcal{R}$ is the

restriction of such operator to the truncated bases $\mathcal{B}_0$ and $\mathcal{B}_1$. It is by incorporating the effect of the basis transformation on the overlap that this formalism go beyond the traditional formulas, which in contrast are strictly valid only when the matrix $\mathcal{R}$ is the identity.

The calculation of the overlap (3.22) starts by writing the operator $\hat{O}$ in its second quantization form,

$$O = \sum_{kl} O_{kl}^{01} c_{0,k}^\dagger c_{1,l} \,, \tag{C.4}$$

$$O_{kl}^{01} = {}_0\langle k \,|\, O \,|\, l \rangle_1 \,, \tag{C.5}$$

where the indexes k and l run over the compete Hilbert spaces. The following contraction,

$$\varrho_{lk}^{01} = \begin{cases} \dfrac{\langle \phi_0 \,|\, c_{0,k}^\dagger c_{1,l} \,|\, \phi_1 \rangle}{\langle \phi_0 \,|\, \phi_1 \rangle} = [v_1^* A^{-1} v_0^\mathsf{T}] & \text{if } k \in \mathcal{B}_0 \text{ and } l \in \mathcal{B}_1 \\ 0 & \text{otherwise} \end{cases} \,, \tag{C.6}$$

$$A = u_0^\mathsf{T} (\mathcal{R}^\mathsf{T})^{-1} u_1^* + v_0^\mathsf{T} \mathcal{R} v_1^* \,, \tag{C.7}$$

calculated with the Wick's theorem, is used for the calculations of the overlap

$$\frac{\langle \phi_0 \,|\, O \,|\, \phi_1 \rangle}{\langle \phi_0 \,|\, \phi_1 \rangle} = \mathrm{tr}\big[O^{01} \varrho^{01} \big] \,. \tag{C.8}$$

In the case of interest of this manuscript, Equation (C.8) becomes

$$\langle \phi_0 \,|\, \phi_1 \rangle = \sqrt{\det A \det \mathcal{R}} \,, \tag{C.9}$$

whereas the traditional Onishi formula would read

$$\langle \phi_0 \,|\, \phi_1 \rangle = \sqrt{\det A_{\text{trad}}} \tag{C.10}$$

$$A_{\text{trad}} = u_0^\mathsf{T} u_1^* + v_0^\mathsf{T} v_1^* \tag{C.11}$$

Furthermore, the matrix $\mathcal{R}$ can be decomposed according to

$$\mathcal{R} = L_0^* L_1^\mathsf{T} \,, \tag{C.12}$$

where the L_i matrices are lower-triangular. The decomposition (C.12) suggests the definition

of the transformations

$$\tilde{u}_0 = (L_0^*)^{-1} u_0 L_0^\dagger , \tag{C.13}$$

$$\tilde{v}_0 = L_0^\dagger v_0 L_0^\dagger , \tag{C.14}$$

$$\tilde{u}_1 = (L_1^*)^{-1} u_1 L_1^\dagger , \tag{C.15}$$

$$\tilde{v}_1 = L_1^\dagger v_1 L_1^\dagger , \tag{C.16}$$

that allows to define

$$\tilde{A} = \tilde{u}_0^\intercal (\mathcal{R}^\intercal)^{-1} \tilde{u}_1^* + \tilde{v}_0^\intercal \mathcal{R} \tilde{v}_1^* , \tag{C.17}$$

and to rewrite (C.8) in the following way:

$$\langle \phi_0 \, | \, \phi_1 \rangle = \sqrt{\det \tilde{A}} . \tag{C.18}$$

Finally, consider the application of the formalism to the case in which the bases $\mathcal{B}_i$ are two truncated deformed HO bases, composed by states of the type (3.26) connected one to the other by

$$\Phi_\alpha(\vec{r}, b_0) = \sum_{\beta=0}^{\alpha} L_{\alpha\beta}(q_{01}) \Phi_\beta(\vec{r}, b_1) , \tag{C.19}$$

$$L_{\alpha\beta} = L_{n_z m_z} L_{(n_\perp m_l),(n_\perp' m_l')}, \tag{C.20}$$

where $\alpha = (n_z, n_r, m_l, m_s)$, $\beta = (n_z', n_r', m_l', m_s')$ and $q_{01} = b_1/b_0$. Dropping some indexes, the explicit form of the one-dimensional matrices L_{nm} is given by

$$L_{nm}(q) = \Delta_{nm} \frac{\sqrt{\frac{n!}{m!}}}{2^{\frac{n-m}{2}} \left(\frac{n-m}{2}\right)!} (q^2 - 1)^{\frac{n-m}{2}} q^{m+\frac{1}{2}} \tag{C.21}$$

$$\Delta_{mn} = \frac{1}{2}[1 + (-1)^{n+m}] ; \tag{C.22}$$

The matrices are lower-triangular: $L_{nm} = 0$ if $m > n$. In fact, the matrix $L_{nm}(q)$ is triangular only if the standard ordering of the HO basis is taken. If the condition is not fulfilled, the inverse matrices $L_{nm}^{-1}(q)$ cannot be calculated analytically. In the present case $\vec{\alpha} = (n_z, n_r, m_l, m_s)$ is the set of good quantum numbers for the axially symmetric HO basis (3.27, 3.28). The standard ordering consists in $m_s = 0, 1$, $m_l = \Omega - \frac{1}{2} - m_s$, $n_z = 0, \ldots, N_z - m_l$, $n_r = 0, \ldots, \frac{N_z - n_z - m_l}{2}$,

where $\Omega = K - \frac{1}{2}$ and K is the largest possible value of the total angular momentum, equal to the number of major shells that define the truncated HO basis. With these premises, the inverse of the matrix $L_{nm}(q)$ reads

$$L_{mr}^{-1}(q) = \Delta_{mr} \frac{(-)^{\frac{m-r}{2}} \sqrt{\frac{m!}{r!}}}{2^{\frac{m-r}{2}} \left(\frac{m-r}{2}\right)!} (q^2 - 1)^{\frac{m-r}{2}} q^{-m-\frac{1}{2}} \tag{C.23}$$

The generalization of the previous formulas to the two-dimensional case reads

$$L_{(N,m),(N',m')}(q) = \delta_{mm'} \frac{1}{\left(\frac{N-N'}{2}\right)!} \left(\frac{\frac{N\pm m}{2}}{\frac{N'\pm m'}{2}}\right)^{\frac{1}{2}} (1-q^2)^{\frac{N-N'}{2}} q^{N'+1} \tag{C.24}$$

$$L_{(N,m),(N',m')}^{-1}(q) = \delta_{mm'} \frac{(-)^{\frac{N-N'}{2}}}{\left(\frac{N-N'}{2}\right)!} \left(\frac{\frac{N\pm m}{2}}{\frac{N'\pm m'}{2}}\right)^{\frac{1}{2}} (1-q^2)^{\frac{N-N'}{2}} q^{-N-1} \tag{C.25}$$

$$\left(\frac{N\pm m}{2}\right) = \left(\frac{N+m}{2}\right)\left(\frac{N-m}{2}\right) \tag{C.26}$$

where $N = 2n_\perp + |m|$.

In the implementation of this formalism of this work, the non-trivial problem of extending the formalism to include bases with different dimensionality was considered. Specifically, the DPM-DK routine, section 3.4.1, receives the wavefunctions, specifically the matrices u_i and v_i, as an output of HFBTHO, which is treated like a black box. Therefore, there is no specific information about the way in which the HO oscillator basis was built, or about the ordering of the corresponding energy levels.

If two bases have the same dimensionality and, most important, contain the same states, namely

$$\mathcal{B}_0 \cap \mathcal{B}_1 = \mathcal{B}_0 = \mathcal{B}_1, \tag{C.27}$$

then the condition of respecting the standard ordering is sufficient to properly calculate the overlaps within the discussed formalism, taking into account that the two bases may have different oscillator length b_i and deformation $\beta_{0,i}$. If this is not the case, some adjustments are required. In particular, consider an harmonic oscillator basis characterized by a total number of states $N = \frac{(n_0+1)(n_0+2)(n_0+3)}{6}$, where n_0 is the number of major shells that truncates the basis in practical applications. When a basis has a non-vanishing deformation, $b_z \neq b_\perp$ and $\beta_0 \neq 0$, it can happen that states from upper shells intrude lower shells, and vice versa. One may then consider a cut-off state with energy $E_{\text{cut-off}} < E_N$. The corresponding number of state $N_{\text{cut-off}}$ is then used

in place of N, to reduce the size of the basis without neglecting highly deformed but low-lying levels. It is easy to understand that bases with different dimensionality and/or deformation can wind up differing for a certain amount of states. In fact, the energy of a HO state is

$$E_n = \frac{\hbar^2}{2m}\left[\frac{1}{b_z^2}(2n_z + 1) + \frac{2}{b_\perp^2}(n_r + 1)\right],$$ (C.28)

where b_z, b_r are functions of b_0, β_0 according to Equations (3.24) and (3.25).

To be able to apply Equation (C.18) to this general case, a first simple idea is to extend the smaller basis, say $\mathcal{B}_0$, to have the same dimensionality of the larger one. One then marks the added states as unoccupied in the U, V matrices, namely $v_{ij} = 0$ and $u_{ij} = \delta_{ij}$. Unfortunately, this idea works fine only if

$$\mathcal{B}_0 \cup \mathcal{B}_1 = \mathcal{B}_1.$$ (C.29)

In the most general case,

$$\mathcal{B}_0 = \{c_1, \ldots, c_M, \beta_1, \ldots, \beta_X\}$$ (C.30)

$$\mathcal{B}_1 = \{c_1, \ldots, c_M, \gamma_1, \ldots, \gamma_Y\},$$ (C.31)

and one must extent both bases to

$$\mathcal{B}_0' = \mathcal{B}_0 \cup \{\gamma_i\}_{i=1}^Y$$ (C.32)

$$\mathcal{B}_1' = \mathcal{B}_1 \cup \{\beta_i\}_{i=1}^X.$$ (C.33)

To be able to use the analytic expressions of the L-matrices, both bases must be reordered according to the standard ordering. The simplest way to do so when one does not know the original level ordering of the two bases is to rebuild them from scratch, and to add, in the process, the states $\{\gamma_i\}_{i=1}^Y$ and $\{\beta_i\}_{i=1}^X$ as prescribed in the previous two equations. Those states would be otherwise discarded, since

$$E(\{\gamma_i\}_{i=1}^Y\}) > E_{\text{cut-off}}(\mathcal{B}_0)$$ (C.34)

$$E(\{\beta_i\}_{i=1}^X\}) > E_{\text{cut-off}}(\mathcal{B}_1).$$ (C.35)

In the process of building the two bases $\mathcal{B}_0'$ and $\mathcal{B}_1'$, the indexes of the added states must be also stored, that is, one needs to know at which point of the standard ordering of the set they were

created. Finally, one can modify the corresponding rows and columns of the U and V matrices coming from HFBTHO. The matrices are square, with size $M + X$ and $M + Y$ respectively. One must transform them into matrices of size $M + X + Y$ by adding a row and a column at each stored index of the added states, so that the standard ordering is respected.

Bibliography

[1] H. De Vries, C. De Jager, and C. De Vries, Atomic Data and Nuclear Data Tables **36**, 495 (1987).

[2] J. Zenihiro *et al.*, Phys. Rev. C **82**, 044611 (2010).

[3] C. Weizsäcker, Z. Physik **96**, 431458 (1935).

[4] H.-W. Hammer, A. Nogga, and A. Schwenk, Rev. Mod. Phys. **85**, 197 (2013).

[5] R. B. Wiringa, V. G. J. Stoks, and R. Schiavilla, Phys. Rev. C **51**, 38 (1995).

[6] K. Holinde, 448 (1996).

[7] S. Malbrunot-Ettenauer *et al.*, Phys. Rev. Lett. **128**, 022502 (2022).

[8] M. Kortelainen *et al.*, Phys. Rev. C **105**, L021303 (2022).

[9] S. C. Pieper and R. B. Wiringa, Annual Review of Nuclear and Particle Science **51**, 53 (2001).

[10] J. Carlson, Phys. Rev. C **36**, 2026 (1987).

[11] P. Navrátil, Ab initio no-core shell model calculations for light nuclei, 2007.

[12] P. Navrátil, S. Quaglioni, I. Stetcu, and B. R. Barrett, Journal of Physics G: Nuclear and Particle Physics **36**, 083101 (2009).

[13] E. Epelbaum, H. Krebs, and U.-G. Meißner, Phys. Rev. Lett. **115**, 122301 (2015).

[14] E. Epelbaum, H. Krebs, and U.-G. Meißner, Eur. Phys. J. A **51**, (2015).

[15] Reinert, P., Krebs, H., and Epelbaum, E., Eur. Phys. J. A **54**, 86 (2018).

[16] S. Weinberg, Physics Letters B **251**, 288 (1990).

[17] S. J. Novario, G. Hagen, G. R. Jansen, and T. Papenbrock, Phys. Rev. C **102**, 051303 (2020).

[18] G. Hagen *et al.*, Phys. Rev. C **105**, 064311 (2022).

[19] F. Marino *et al.*, Phys. Rev. C **104**, 024315 (2021).

[20] V. Strutinsky, Nuclear Physics A **122**, 1 (1968).

[21] M. Brack and P. Quentin, Physics Letters B **56**, 421 (1975).

[22] W. Koepf, M. Sharma, and P. Ring, Nuclear Physics A **533**, 95 (1991).

[23] H. Krappe and K. Pomorski, *Theory of Nuclear Fission: A Textbook* (Springer Berlin, Heidelberg, Germany, 2012).

[24] L. H. Thomas, Mathematical Proceedings of the Cambridge Philosophical Society **23**, 542 (1927).

[25] E. Fermi, Rend. Accad. Naz. Lincei. **6**, 602 (1927).

[26] O. Haxel, J. H. D. Jensen, and H. E. Suess, Phys. Rev. **75**, 1766 (1949).

[27] B. A. Brown and B. H. Wildenthal, Annual Review of Nuclear and Particle Science **38**, 29 (1988).

[28] M. Bender, P.-H. Heenen, and P.-G. Reinhard, Rev. Mod. Phys. **75**, 121 (2003).

[29] Y. F. Niu *et al.*, Phys. Rev. C **94**, 064328 (2016).

[30] C. Wa Wong, Physics Reports **15**, 283 (1975).

[31] K. Matsuyanagi *et al.*, Physica Scripta **91**, 063014 (2016).

[32] W. Satuła, J. Dobaczewski, and W. Nazarewicz, Physical Review Letters **81**, (1998).

[33] J. Y. Zeng, T. H. Jin, and Z. J. Zhao, Phys. Rev. C **50**, 1388 (1994).

[34] P. Ring and P. Schuck, *The Nuclear Many-Body Problem* (Springer Verlag, New York, NY, 1980).

[35] A. Bulgac, Hartree–Fock–Bogoliubov Approximation for Finite Systems, 1999.

[36] H. Kucharek and P. Ring, Z. Physik A - Hadrons and Nuclei **339**, 23 (1991).

[37] P. Ring, Progress in Particle and Nuclear Physics **37**, 193 (1996).

[38] R. A. Broglia, *Fifty Years of Nuclear BCS* (World Scientific, Singapore, 2013).

[39] J. Dobaczewski *et al.*, Phys. Rev. C **53**, 2809 (1996).

[40] P. Marević *et al.*, Computer Physics Communications **276**, 108367 (2022).

[41] T. Nikšić, N. Paar, D. Vretenar, and P. Ring, Computer Physics Communications **185**, 18081821 (2014).

[42] T. Skyrme, Nuclear Physics **9**, 615 (1958).

[43] M. Grasso, Progress in Particle and Nuclear Physics **106**, 256 (2019).

[44] D. Brink and E. Boeker, Nuclear Physics A **91**, 1 (1967).

[45] J. Decharand D. Gogny, Phys. Rev. C **21**, 1568 (1980).

[46] G. A. Lalazissis, T. Nikšić, D. Vretenar, and P. Ring, Phys. Rev. C **71**, 024312 (2005).

[47] T. Nikšić, D. Vretenar, G. A. Lalazissis, and P. Ring, Phys. Rev. C **77**, 034302 (2008).

[48] T. Nikšić, D. Vretenar, and P. Ring, Progress in Particle and Nuclear Physics **66**, 519 (2011).

[49] C. Horowitz and B. D. Serot, Nuclear Physics A **368**, 503 (1981).

[50] J. Boguta and A. Bodmer, Nuclear Physics A **292**, 413 (1977).

[51] B. D. Serot, Physics Letters B **107**, 263 (1981).

[52] R. Furnstahl, Physics Letters B **152**, 313 (1985).

[53] T. Nikšić, D. Vretenar, and P. Ring, Phys. Rev. C **78**, 034318 (2008).

[54] M. Serra and P. Ring, Phys. Rev. C **65**, 064324 (2002).

[55] G. Lalazissis *et al.*, Physics Letters B **671**, 36 (2009).

[56] J. Berger, M. Girod, and D. Gogny, Nuclear Physics A **428**, 23 (1984).

[57] U. Mutz and P. Ring, Journal of Physics G: Nuclear Physics **10**, L39 (1984).

[58] J. A. Sheikh *et al.*, Journal of Physics G: Nuclear and Particle Physics **48**, 123001 (2021).

[59] H. J. Lipkin, Annals of Physics **9**, 272 (1960).

[60] J. F. Goodfellow and Y. Nogami, Canadian Journal of Physics **44**, 1321 (1966).

[61] A. Kamlah, Z. Physik **216**, 52 (1968).

[62] P. Hohenberg and W. Kohn, Phys. Rev. **136**, B864 (1964).

[63] H. Englisch and R. Englisch, Physica A: Statistical Mechanics and its Applications **121**, 253 (1983).

[64] E. Lieb, International Journal of Quantum Chemistry **24**, 243 (1983).

[65] W. Kohn and L. J. Sham, Phys. Rev. **140**, A1133 (1965).

[66] K. Capelle, A bird's-eye view of density-functional theory, 2002.

[67] J. P. Kaipio and E. Somersalo, *Statistical and Computational Inverse Problems* (Springer New York, New York, NY, 2005).

[68] J. Hadamard, Princeton University Bulletin **13**, 49 (1902).

[69] J. Kaipio and E. Somersalo, Journal of Computational and Applied Mathematics **198**, 493 (2007), special Issue: Applied Computational Inverse Problems.

[70] J. T. Chayes, L. Chayes, and M. B. Ruskai, Journal of Statistical Physics **38**, 497 (1985).

[71] Y. Engel *et al.*, Nuclear Physics A **249**, 215 (1975).

[72] E. Perlińska, S. G. Rohoziński, J. Dobaczewski, and W. Nazarewicz, Phys. Rev. C **69**, 014316 (2004).

[73] F. Raimondi, B. G. Carlsson, and J. Dobaczewski, Phys. Rev. C **83**, 054311 (2011).

[74] P. Becker *et al.*, Phys. Rev. C **96**, 044330 (2017).

[75] J. Drut, R. Furnstahl, and L. Platter, Progress in Particle and Nuclear Physics **64**, 120 (2010).

[76] P. Giannozzi and S. Baroni, in *Handbook of Materials Modeling: Methods*, edited by S. Yip (Springer Netherlands, Dordrecht, 2005), pp. 195–214.

[77] D. S. Jensen and A. Wasserman, International Journal of Quantum Chemistry **118**, e25425 (2018).

[78] D. S. Koltun and J. M. Eisenberg, *Quantum mechanics of many degrees of freedom* (Wiley-VCH, New York, NY, 1988).

[79] G. Accorto, A Constrained-Minimization Method for the Solution of the Inverse Kohn-Sham Problem in Nuclei, 2018.

[80] A. Wächter and L. Biegler, Mathematical Programming **106**, 25 (2006).

[81] I. Sick, Nuclear Physics A **218**, 509 (1974).

[82] L. Ray, Phys. Rev. C **19**, 1855 (1979).

[83] B. Alex Brown, Phys. Rev. C **58**, 220 (1998).

[84] A. Baran *et al.*, Phys. Rev. C **78**, 014318 (2008).

[85] T. Naito, D. Ohashi, and H. Liang, Journal of Physics B: Atomic, Molecular and Optical Physics **52**, 245003 (2019).

[86] I. Korneev and I. Panov, Astronomy Letters **37**, (2011).

[87] J. Nix, Physics Letters B **30**, 1 (1969).

[88] E. M. Burbidge, G. R. Burbidge, W. A. Fowler, and F. Hoyle, Rev. Mod. Phys. **29**, 547 (1957).

[89] P. A. Seeger, W. A. Fowler, and D. D. Clayton, Astrophysical Journal Supplement **11**, 121 (1965).

[90] M. Bender *et al.*, Journal of Physics G: Nuclear and Particle Physics **47**, 113002 (2020).

[91] N. Schunck and L. M. Robledo, Reports on Progress in Physics **79**, 116301 (2016).

[92] A. Bulgac, S. Jin, and I. Stetcu, Frontiers in Physics **8**, (2020).

[93] K. Dietrich, J.-J. Niez, and J.-F. Berger, Nuclear Physics A **832**, 249 (2010).

[94] E. Orestes, K. Capelle, A. B. F. da Silva, and C. A. Ullrich, The Journal of Chemical Physics **127**, 124101 (2007).

[95] M. Verriere and D. Regnier, Frontiers in Physics **8**, (2020).

[96] G. Scamps and D. Lacroix, Phys. Rev. C **87**, 014605 (2013).

[97] A. Bulgac *et al.*, Phys. Rev. C **100**, 034615 (2019).

[98] J. Sadhukhan, C. Zhang, W. Nazarewicz, and N. Schunck, Phys. Rev. C **96**, 061301 (2017).

[99] J. Zhao *et al.*, Phys. Rev. C **93**, 044315 (2016).

[100] J. Zhao *et al.*, Phys. Rev. C **99**, 054613 (2019).

[101] N. Schunck and D. Regnier, Progress in Particle and Nuclear Physics **125**, 103963 (2022).

[102] K.-H. Schmidt and B. Jurado, Reports on Progress in Physics **81**, 106301 (2018).

[103] T. Papenbrock and D. J. Dean, Phys. Rev. C **67**, 051303 (2003).

[104] C. Robin, M. J. Savage, and N. Pillet, Phys. Rev. C **103**, 034325 (2021).

[105] P. Goddard, P. Stevenson, and A. Rios, Phys. Rev. C **92**, 054610 (2015).

[106] K. Hagino and N. Takigawa, Progress of Theoretical Physics **128**, 1061 (2012).

[107] J. J. Sakurai and J. Napolitano, *Modern Quantum Mechanics* (Cambridge University Press, Cambridge, UK, 2017).

[108] J. Sadhukhan *et al.*, Phys. Rev. C **90**, 061304 (2014).

[109] J. Sadhukhan *et al.*, Phys. Rev. C **88**, 064314 (2013).

[110] A. Staszczak, A. Baran, and W. Nazarewicz, Phys. Rev. C **87**, 024320 (2013).

[111] D. Brink and A. Weiguny, Nuclear Physics A **120**, 59 (1968).

[112] A. Staszczak, S. Piłat, and K. Pomorski, Nuclear Physics A **504**, 589 (1989).

[113] A. Baran, A. Staszczak, J. Dovaczewski, and W. Nazarewicz, International Journal of Modern Physics E **16**, 443 (2007).

[114] J. N. Leboeuf and R. C. Sharma, Canadian Journal of Physics **51**, 2023 (1973).

[115] S. A. Giuliani and L. M. Robledo, Physics Letters B **787**, 134 (2018).

[116] M. Baranger and M. Veneroni, Annals of Physics **114**, 123 (1978).

[117] A. Baran *et al.*, Phys. Rev. C **84**, 054321 (2011).

[118] M. Warda and J. L. Egido, Phys. Rev. C **86**, 014322 (2012).

[119] J. Randrup and P. Möller, Phys. Rev. C **88**, 064606 (2013).

[120] A. Baran, Physics Letters B **76**, 8 (1978).

[121] S. G. Nilsson *et al.*, Nuclear Physics A **131**, 1 (1969).

[122] N. Dubray and D. Regnier, Computer Physics Communications **183**, 2035 (2012).

[123] A. Zdeb, M. Warda, and L. M. Robledo, Phys. Rev. C **104**, 014610 (2021).

[124] R. Han, M. Warda, A. Zdeb, and L. M. Robledo, Phys. Rev. C **104**, 064602 (2021).

[125] N. Onishi and S. Yoshida, Nuclear Physics **80**, 367 (1966).

[126] T. Mizusaki, M. Oi, and N. Shimizu, Physics Letters B **779**, 237 (2018).

[127] A. Porro and T. Duguet, On the off-diagonal Wick's theorem and Onishi formula, 2022.

[128] G. F. Bertsch and L. M. Robledo, Phys. Rev. Lett. **108**, 042505 (2012).

[129] G. C. Wick, Phys. Rev. **80**, 268 (1950).

[130] L. M. Robledo, Phys. Rev. C **50**, 2874 (1994).

[131] P. Marević and N. Schunck, Phys. Rev. Lett. **125**, 102504 (2020).

[132] L. M. Robledo, Phys. Rev. C **105**, L021307 (2022).

[133] L. M. Robledo, Phys. Rev. C **105**, 044317 (2022).

[134] W. Younes and D. M. Gogny, *Fragment Yields Calculated in a Time-Dependent Microscopic Theory of Fission* (Springer, New York, NY, 2012).

[135] W. Younes, D. M. Gogny, and J. F. Berger, Lecture Notes in Physics (2019).

[136] N.-W. T. Lau, R. N. Bernard, and C. Simenel, Phys. Rev. C **105**, 034617 (2022).

[137] A. Baran, K. Pomorski, A. Lukasiak, and A. Sobiczewski, Nuclear Physics A **361**, 83 (1981).

[138] J. Sadhukhan *et al.*, Phys. Rev. C **88**, 064314 (2013).

[139] S. S. Skiena, in *The Algorithm Design Manual* (Springer London, London, 2008), pp. 103–144.

[140] E. Flynn *et al.*, Phys. Rev. C **105**, 054302 (2022).

[141] S. A. Giuliani, L. M. Robledo, and R. Rodríguez-Guzmán, Phys. Rev. C **90**, 054311 (2014).

[142] E. Yuldashbaeva, J. Libert, P. Quentin, and M. Girod, Physics Letters B **461**, 1 (1999).

[143] A. Staszczak, A. Baran, K. Pomorski, and K. Böning, Physics Letters B **161**, 227 (1985).

[144] L. Moretto and R. Babinet, Physics Letters B **49**, 147 (1974).

[145] H. Abusara, A. V. Afanasjev, and P. Ring, Phys. Rev. C **85**, 024314 (2012).

[146] A. Zdeb, A. Dobrowolski, and M. Warda, Phys. Rev. C **95**, 054608 (2017).

[147] G. Accorto *et al.*, Phys. Rev. C **101**, 024315 (2020).

[148] G. Accorto *et al.*, Phys. Rev. C **103**, 044304 (2021).

[149] H.-P. Breuer and F. Petruccione, *The Theory of Open Quantum Systems* (Oxford University Press, Oxford, UK, 2007).

[150] W. Younes and D. Gogny, Phys. Rev. C **80**, 054313 (2009).

[151] B. Giraud, J. Le Tourneux, and S. Wong, Physics Letters B **32**, 23 (1970).

[152] N. Berline and M. V. Ezra Getzler, *Heat Kernels and Dirac Operators* (Springer Berlin, Heidelberg, DE, 1992).

Curiculum Vitae

Address:

- Institute: Physics Department, Faculty of Mathematics and Natural Sciences, University of Zagreb, Bijenička 32, 10 000 Zagreb, Croatia

- e-mail: gaccorto@phy.hr

- Private 1: Stjepana Ladiša 1, 10000, Zagreb, Croatia

- Private 2: Via Gaggio 34A, Malgrate, 23864, Italy

- Phone: +39 348 1769251

Personal:

- Date and Place of Birth: 24 January 1993, Lecco, 23900, Italy

- Nationality: Italian;

Education:

- **1999 - 2012**: Elementary and High Schools in Malgrate and Lecco, Italy;

- **2012 - 2018** : Physics Department, University of Milan - Statale, Italy;

- **February 2015** : B.Sc. in Physics, University of Milan - Statale, Thesis: *Sensitivity of nuclear matter on the range of the effective interaction*, Thesis supervisors: Prof. Xavier Roca-Maza, Prof. Gianluca Colò;

- **July 2018** : M.Sc. in Nuclear Physics, University of Milan - Statale, Thesis: *A constrained-minimization method for the solution of the Inverse Kohn-Sham problem in nuclei*, Thesis supervisors: Prof. Gianluca Colò, Prof. Xavier Roca-Maza.

List of publications

PUBLICATIONS IN SCIENTIFIC JOURNALS:

1. **G. Accorto**, P. Brandolini, F. Marino, A. Porro, A. Scalesi, G. Colĭ, X. Roca-Maza, E. Vigezzi: First step in the nuclear inverse Kohn-Sham problem: From densities to potentials, **Phys. Rev. C 101** 024315 (2020).

2. **G. Accorto**, T. Naito, H. Liang, T. Nikšić, D. Vretenar: Nuclear energy density functionals from empirical ground-state densities, **Phys. Rev. C 103**, 044304 (2021).

List of Figures

144

List of Tables